Magnetically-Forced Axisymmetric Zonal Accelerations in Earth's Outer Core

by

Colin More

A thesis submitted in partial fulfillment of the requirements
for the degree of

Doctor of Philosophy
in
GEOPHYSICS

Department of Physics
University of Alberta

Abstract

Azimuthal accelerations of cylindrical surfaces co-axial with the rotation axis have been inferred to exist in Earth's fluid core on the basis of magnetic field observations and changes in the length-of-day. These accelerations have a typical timescale of decades. However, the physical mechanism causing the accelerations is not well understood. Scaling arguments suggest that the leading order torque averaged over cylindrical surfaces should arise from the Lorentz force. Decadal fluctuations in the magnetic field inside the core, driven by convective flows, could then force decadal changes in the Lorentz torque and generate zonal accelerations. This hypothesis is tested by constructing a quasi-geostrophic model of magnetoconvection, with thermally-driven flows perturbing a steady, imposed background magnetic field. It is found that when the Alfvén number is similar to that estimated for Earth's fluid core, temporal fluctuations in the torque balance are dominated by the Lorentz torque, with the latter generating mean zonal accelerations. The model reproduces both fast, free Alfvén waves and slow, forced accelerations, with ratios of relative strength and relative timescale similar to those inferred for the Earth's core. The temporal changes in the magnetic field which drive the time-varying Lorentz torque are produced by the underlying convective flows, which shear and advect the magnetic field on timescales associated with convective eddies. These results support the hypothesis that temporal changes in the magnetic field deep inside Earth's fluid core drive the observed decadal zonal accelerations of cylindrical surfaces through the Lorentz torque.

Physics is the science of what you can throw away.

- Keith Cuff

Acknowledgements

The successful completion of a PhD project is not due to the brilliance of a single person, but to that of the medium-sized army of friends, colleagues, acquaintances, teachers, professors, mentors, and family members which helped along the way. I have been extraordinarily lucky to have been surrounded by one of the finest such armies throughout my academic career. The successes of the project rightly belong to all of them, while its weaknesses lie wholely with myself.

I would particularly like to thank my PhD supervisor, Mathieu Dumberry, for the remarkable amount of patience, support, and intelligence he has displayed over the course of the six and a half years it took to produce this thesis. I am sure better supervisors exist, but I have trouble imagining how. I would also like to thank my committee members, Moritz Heimpel and Bruce Sutherland, for their own commitment to the project. Bruce in particular displayed a remarkable capacity for punishment by signing up for a second tour, having also supervised my master's thesis!

This being a terminal degree, now seems to be an ideal time to look back on all the teachers who have contributed to getting me here. A good teacher is, in the truest sense of the word, priceless, and I have had many. A non-exhaustive list would include Mrs. Bullock and Ms. Smith, Mr. Fowler and Mr. Dencer, Tim Cooper, George McGuire, Derek Harnett, Rob Woodside, and Jeff Chizma. An exhaustive list would be *significantly* longer (compared to

what, you ask, Tim? Why, the non-exhaustive list, of course!). Thank you all.

I have been very fortunate to have had the support of NSERC post-graduate scholarships at several points in my graduate school career. I certainly appreciated them when I won them, and I appreciated them even more after they ran out!

I have been even more fortunate with the officemates I've had over the course of this degree, and with the friends I've made. Life really is largely about the people you're surrounded with on a daily basis, and my surroundings have been wonderful. Thanks in particular to Ben, Dan, Daniel, Drew, Kathrin, Keith, Olivia, and the Sarahs. That was a good time!

The trials of the past several years were eased tremendously by my girlfriend, Julie. While many people truly cared for me and offered their support, she did so while having to actually live with me! It certainly wasn't great fun for her much of the time, but she never complained, and whenever I thought her patience was at an end she instead managed to give me even more. It was also pretty great having food appear while I was in the depths of writing. I love you.

Like the Matrix, nobody can be told what it's like to be in graduate school. Happily, my dearest sister, Heather, has always been a year or three ahead of me. It's meant so much to have someone who knows exactly what is going on, while also knowing exactly what I need. Such as musical suggestions at strange hours of the night, or encouragement to outside for a change. Thanks, from your favourite brother who is really really happy to be done!

Finally, my parents. You have been constant sources of encouragement, support, and love throughout this journey and throughout my life. None of this could have happened without you. Thank you.

Contents

List of Tables

List of Figures

Chapter 1

Introduction

The remote setting and extreme environment of Earth's core make it a very difficult structure to study. Only in the past century has such basic information as its size, composition, and phase been rigorously established. Analysis of Earth's orientation in space, its elasticity, and its seismological properties show its deep interior to be composed of two distinct regions. The innermost region is a solid, metallic core extending to a radius of 1220 km. The outer region is a spherical shell surrounding the inner core, extending from the surface of the latter (the inner core boundary, or ICB) to the core-mantle boundary (CMB) at a radius of 3480 km (Jeffreys, 1926; Brush, 1980; Souriau and Calvet, 2015; Stixrude and Jeanloz, 2015).

The outer core is known to be a self-sustaining dynamo which generates the dominant part of Earth's magnetic field (Jones, 2015). However, the mechanism driving the dynamo is largely unknown. Tidal forcing (e.g. Kerswell and Malkus, 1998; Le Bars et al., 2015) and convection due to radiogenic heating of core fluid (e.g. Kutzner and Christensen, 2000) have been shown to be capable of forcing other planetary dynamos. However, in Earth's core, the most likely candidate is turbulent convection driven by a combination of chemical buoyancy and secular cooling (Nataf and Schaeffer, 2015). Chemical buoyancy results from light elements, such as carbon and sulphur, being rejected as material freezes onto the inner core.

Since this lowers the density of the fluid in the neighbourhood where freezing is occurring, the fluid experiences a buoyant force. Secular cooling, on the other hand, relies on a superadiabatic temperature gradient between the ICB and the CMB. Conduction and convection then work together to transport the excess heat out of the core, with convection dominating if the temperature gradient is large enough.

Both chemical buoyancy and secular cooling are strongly affected by the thermal and mechanical properties of the outer core material. The material's melting point is of particular interest since the temperature at the ICB plays a key role in estimating the core's mean temperature and density profiles (Nimmo, 2015). However, before the melting point can be found, the chemical composition of the outer core material must be determined. Doing so is a rather interdisciplinary science (Ringwood, 1984; McDonough, 2014). It generally involves using the chemical composition of meteorites and theories of planetary formation to estimate the relative abundance of elements in Earth as a whole (e.g. Wänke and Dreibus, 1988; Wasson and Kallemeyn, 1988; Palme et al., 2014), then applying geochemistry to determine how each chemical component would separate as Earth evolved (Allègre et al., 1995; Li and Agee, 1996; Li and Fei, 2014, e.g.). While this is still a very active field of research, and while there remains considerable debate about the precise recipe, it has been established with some certainty that an iron/nickel alloy is the dominant ingredient, with trace amounts of oxygen, silicon, and sulphur[1]. However, the trace elements likely contribute roughly 10% of the outer core's total mass (Allègre et al., 1995; Hirose et al., 2013; McDonough, 2014).

Assuming the composition of the outer core was known precisely, measuring the melting point of that material (along with other key parameters, like the the viscosity, thermal and

[1]Because of different freezing points for different elements, the different ways elements can or cannot form solid crystal structures, and other geochemical considerations, the proportion of trace elements probably differs between the outer and inner cores. If the density jump between the two bodies were accurately known, geochemists could use these differences to constrain the recipes somewhat. Unfortunately, the density jump is *not* well known.

chemical expansivities, and electrical conductivity) at the temperatures and pressures found in the core would remain challenging. Only recently have laser-heated diamond anvil cell and shock experiments enabled the most modest of the expected conditions to be reached experimentally (e.g. Alfè, 2015; Souriau and Calvet, 2015). Instead, most estimates rely on quantum mechanical calculations based on first principles. These *ab initio* calculations suggest a temperature at the ICB of about 5650 ± 600 K (e.g. Nimmo, 2015). If the outer core is assumed to be undergoing vigorous convection, its mean radial temperature profile should be close to adiabatic. This means the temperature at the CMB can be calculated from that at the ICB, assuming one uses the correct adiabat. This, like the composition of the outer core, is the subject of vigorous debate (see e.g. Alfè, 2015; Souriau and Calvet, 2015). However, Nimmo (2015) estimates the CMB temperature to be in the range of 4180 ± 400 K.

It is likely that compositional buoyancy is the dominant driver of convection in the outer core (Lister and Buffett, 1995), with secular cooling and other mechanisms playing secondary roles (e.g. Jones, 2015). Despite this, many successful self-sustaining dynamo models have been constructed using only thermal forcing, and it remains one of the simplest ways to drive a realistic numerical dynamo (Glatzmaier and Roberts, 1995; Olson, 2015). The credibility of such models, however, relies on the degree to which they can be verified with observations from nature. While it remains impossible to directly observe core flows, we *are* able to directly observe the geomagnetic field at Earth's surface. Because changes in the field's spatial and temporal structures are strongly associated with patterns of flow near the CMB, the magnetic field can provide valuable insight into the dynamics of the core, and provide constraints on any model of core dynamics we may care to construct.

1.1 Geomagnetic Inversions

The notion that changes in the magnetic field at Earth's surface were caused by motions within the planet itself was first proposed by Halley (1692). At the time, electromagnetic induction was unknown; as Halley himself put it, "we know [of no fluids] that are any ways Magnetical". Instead, Halley hypothesized that Earth's interior could be a series of solid, concentric, spherical shells, separated from one another by a "fluid medium between". If each shell were magnetized with a dipole field of independent strength and orientation[2], and the shells were allowed to rotate independently of one another, very complex changes in the observed magnetic field could be explained[3].

Developments in the understanding of electrodynamics soon demonstrated that flows of liquid metals were capable of amplifying and maintaining magnetic fields, thus in effect providing Halley's missing magnetical fluid. Work by Henry Cavendish, Emil Wiechert, Richard Oldham, Beno Gutenberg, Harold Jeffreys, and others (Brush, 1980) had by the 1920's revealed Earth's basic structure, and shown in particular an outer core composed of just such a liquid metal. Larmor (1919) proposed that Earth's main magnetic field (the part not associated with magnetization of the crust, or induced by the magnetosphere's interactions with the solar wind) could be generated by convection occurring within this liquid metal, while Elsasser formalized this idea in a series of three papers in the late 1940's (Elsasser, 1946a,b, 1947). Since then, the idea that the main field is generated by a convectively-driven dynamo in the outer core has been broadly accepted (e.g. Olson, 2015).

Figure 1.1 shows three snapshots corresponding to the estimated configuration of the spherically radial magnetic field at the CMB in 1905, 1950, and 2000. Magnetic field lines pointing

[2]Strictly speaking, Halley did not propose a true dipole, but merely that each shell has two magnetic poles.

[3]It is largely thanks to Halley that the world was given Newton's *Principia Mathematica*. After the Royal Society of London nearly went bankrupt publishing Francis Willughby's *De Historia Piscium*, Halley himself stepped in to bankroll the *Principia*'s publication.

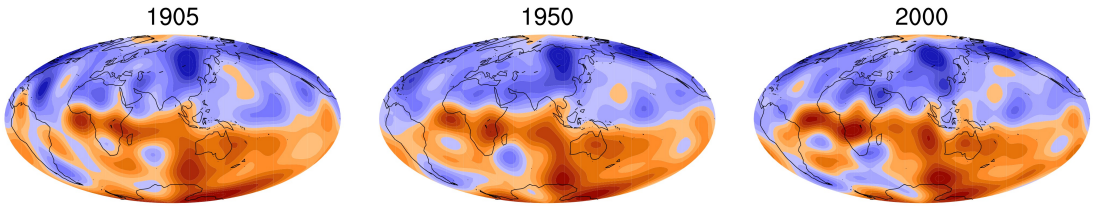

Figure 1.1: Snapshots of the spherically radial (B_r) component of the magnetic field at the core-mantle boundary. Blue and red regions indicate magnetic field lines pointing into and out of the core, respectively. From an extended version of the gufm1 geomagnetic model (Jackson et al., 2000).

out of the core are marked in red, while those pointing into the core are marked in blue. The configuration clearly evolves between snapshots. This time-variability of the main field is termed the "secular variation".

One particularly consistent feature of the global secular variation has been a westward drift of flux patches along the equator (Dumberry and Finlay, 2007). Vestine (1953) assumed the flux patches were being advected by flows at the CMB, enabling him to calculate the azimuthal velocity structure there. He then used that structure to estimate the outer core's total angular momentum. As will be discussed in section 1.3, Earth as a whole must conserve angular momentum. Thus, changes in the outer core's angular momentum must correspond to an equal and opposite change in the angular momentum of the crust and mantle, measurable as a change in the length-of-day (LOD). Vestine's predictions turned out to "correspond reasonably well" with the unexplained changes in LOD observed by Brouwer (1952), linking flow velocities at the CMB to the core's angular momentum for the first time[4].

Vestine's work was the beginning of modern geomagnetic core flow inversion. Such inversions rely on the induction equation. For flow velocity $\mathbf{u}$, magnetic field $\mathbf{B}$, magnetic diffusivity

[4]Munk and Revelle (1952) presented theoretical arguments for this at the same May 1952 meeting of the AGU as Vestine presented his work. Munk and Revelle cite the idea as originally coming from Louis Slichter, the director of the Institute of Geophysics at UCLA at the time.

η, time t, and gradient operator $\boldsymbol{\nabla}$,

$$\frac{\partial \mathbf{B}}{\partial t} = \boldsymbol{\nabla} \times (\mathbf{u} \times \mathbf{B}) + \eta \nabla^2 \mathbf{B} \,. \tag{1.1}$$

While at first glance Eq.(1.1) appears to allow the recovery of all three velocity field components, several considerations limit the amount of velocity information which can be practically extracted from the observed magnetic field.

First, because $\mathbf{B}$'s radial derivatives are not known at the CMB, not enough information exists to calculate the diffusion term of Eq.(1.1). This difficulty is generally overcome, however, by invoking the "frozen flux" approximation (Alfvén, 1943)[5]. It assumes that conductivity is very high, causing the magnitude of the diffusion term to be dominated by the other terms in Eq.(1.1). With $\mathcal{L}$ as the length scale, $\mathcal{T}$ as the magnetic variation's timescale, and $\mathcal{U}$ as the typical flow velocity, the ratio between the diffusion and time variation terms is $\eta \mathcal{T} \mathcal{L}^{-2}$, and the ratio between the diffusion and production terms is $\eta \left(\mathcal{U}\mathcal{L}\right)^{-1}$. Thus, the frozen flux approximation holds if

$$\frac{\eta \mathcal{T}}{\mathcal{L}^2} \ll 1 \quad \text{and} \quad \frac{\eta}{\mathcal{U}\mathcal{L}} \ll 1 \,. \tag{1.2}$$

The magnetic diffusivity of the outer core is thought to be around 0.5 $\mathrm{m^2 s^{-1}}$ (Pozzo et al., 2012). Typical core flow velocities are about 10 km $\mathrm{yr^{-1}}$, or 3×10^{-4} m $\mathrm{s^{-1}}$ (e.g. Holme, 2015). Generally, core flow inversions are done for periods spanning years to decades. A reasonable upper bound for the timescale of changes in the magnetic field used by them could be a century, or about 3×10^9 s. This leaves only the minimum length scale of the inversions to be determined.

The geomagnetic field is often expanded in spherical harmonics. If such an expansion is

[5]At the end of the same six-page paper, Alfvén invented the term "magnetohydrodynamic wave". He also considered "hydromagnetic wave", but dismissed it as "shorter but not quite adequate".

performed on the radial part of the total main field outside the CMB (at radial distance $r = r_2$ from Earth's centre), the magnitude of each degree ℓ depends on a factor $\left(\frac{r_2}{r}\right)^{\ell+2}$. For example, that the dipole part of the main field drops off as $\frac{1}{r^3}$, and the quadrupole by $\frac{1}{r^4}$. Thus, the higher the spherical harmonic degree, the more strongly it is attenuated with distance.

At Earth's surface, where the observations used to construct models of the geomagnetic field are taken, the full field is a composition of the main field, a contribution from magnetic bodies embedded in the crust, and sources from the upper atmosphere and space. While the magnitude of the main field is much greater than that of other sources at low degrees, its contribution to higher degrees is masked by non-core sources. This is illustrated by Figure 1.2. The curved, increasing red line shows the theoretical contribution of the crustal magnetic field, while the straight, decreasing red line shows the theoretical contribution of the core. Red circles show measurements. At about degree 13, the power of the field from the core drops below that from crustal sources (e.g. Maus, 2008; Holme, 2015) Thus, the magnetic structure at the CMB can only be resolved up to degree 13, corresponding to a length scale of about $\mathcal{L} \approx 840$ km.

With these values of η, $\mathcal{U}$, $\mathcal{T}$, and $\mathcal{L}$,

$$\frac{\eta\mathcal{T}}{\mathcal{L}^2} \approx \frac{\eta}{\mathcal{U}\mathcal{L}} \approx 2 \times 10^{-3}\,. \tag{1.3}$$

Thus, the frozen flux approximation is valid for the outer core on timescales of centuries or less.

The second consideration limiting the usefulness of Eq.(1.1) is that, as pointed out by Roberts and Scott (1965) and Backus (1968), the flow field is non-unique. Most core flow inversions use only the radial component of the magnetic field, since this is the component most well-

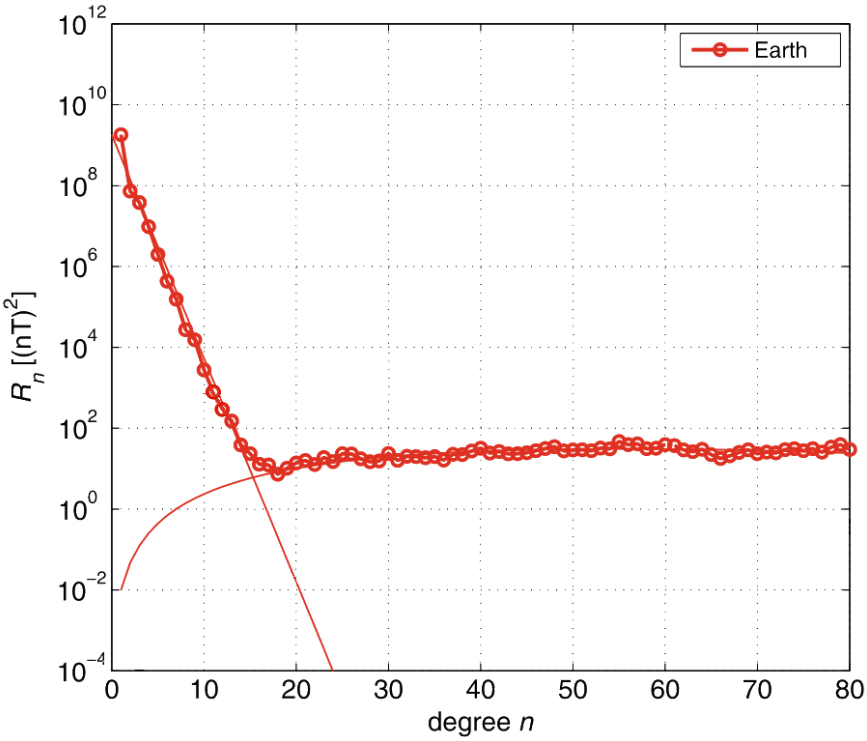

Figure 1.2: Spherical harmonic power spectrum, often called a Mauersberger-Lowes spectrum, for the internally-generated geomagnetic field at Earth's surface. Red dots show measurements. The straight, decreasing red line shows the theoretical power of spectrum from the core, while the curved, increasing red line shows the theoretical spectrum from sources in the crust. Modified from Figure 14 of Hulot et al. (2010).

determined at the CMB. In the usual (r, θ, ϕ) spherical coordinates, the radial component of the induction equation is

$$\frac{\partial B_r}{\partial t} = -\boldsymbol{\nabla}_H \cdot (\mathbf{u} B_r) \,, \tag{1.4}$$

where $\boldsymbol{\nabla}_H$ means only the (θ, ϕ) components of the gradient operator. Backus (1968) shows how $\mathbf{u}B_r$ may be written in terms of two scalar potential functions Φ and Ψ as

$$\mathbf{u} B_r = \boldsymbol{\nabla}_H \Phi - \hat{\mathbf{r}} \times \boldsymbol{\nabla}_H \Psi \,, \tag{1.5}$$

where $\hat{\mathbf{r}}$ is the spherically radial unit vector. Since $\boldsymbol{\nabla}_H \cdot (\hat{\mathbf{r}} \times \boldsymbol{\nabla}_H \Psi) = 0$, substituting Eq.(1.5) into Eq.(1.4) results in

$$\frac{\partial B_r}{\partial t} = -\nabla_H^2 \Phi \,. \tag{1.6}$$

Thus, the flow information carried by Ψ plays no role in the radial magnetic field's time variability, and therefore cannot be calculated using magnetic field observations. This limitation is generally overcome by placing some physical constraint on the flow at the CMB, such as assuming a purely toroidal ($\boldsymbol{\nabla}_H \cdot \mathbf{u}_H = 0$, where $\mathbf{u}_H = u_\theta \hat{\theta} + u_\phi \hat{\phi}$) or tangentially geostrophic ($\boldsymbol{\nabla}_H \cdot (\mathbf{u} \cos\theta) = 0$) flow (Holme, 2015). However, neither of these assumptions fully eliminates the non-uniqueness.

Solutions to Eq.(1.4) are often expanded in spherical harmonics (Whaler, 1986). Such an approach allows the construction of models which match data to arbitrary accuracy, provided the expansion extends to a high enough degree. However, such solutions are unattractive: small-scale flows are not required to explain large-scale magnetic features, and are therefore not uniquely recoverable from those magnetic features. Instead, techniques have been adopted to bias solutions towards large-scale, smooth flows (Holme, 2015). Differences in the choice and implementation of such constraints, along with differences in how the original

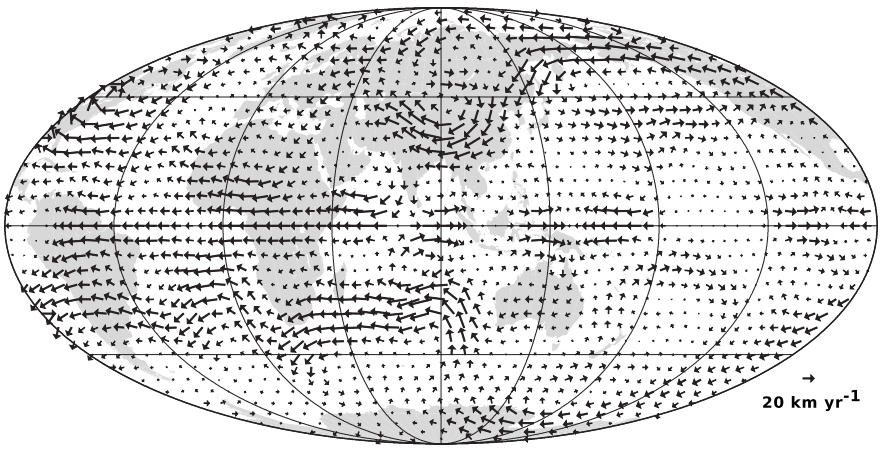

Figure 1.3: Snapshot of flow velocities at the core-mantle boundary, as inverted from the secular variation of the geomagnetic field. The root-mean-square velocity is 15.2 km yr^{-1}. Modified from Figure 3 of Holme (2015), originally in Holme and Olsen (2006).

magnetic field model was constructed and projected onto the CMB, leads to the considerable differences found between various core flow models (e.g. Bloxham and Jackson, 1991).

A final consideration when building a core flow model is the conductivity of the mantle. If it is not a perfect insulator, projecting the magnetic field observed at the surface through it to the CMB will induce very large uncertainties. Therefore it *is* generally assumed to be a perfect insulator when building such models (Holme, 2015).

A wide variety of core flow models have been inverted from geomagnetic data over the years. A snapshot of the velocity field from a typical one is shown in Figure 1.3. However, such snapshots show only the velocity field in a very thin layer near the CMB – electromagnetic screening prevents a view of any flow information beneath this layer. Fortunately for studies of core dynamics, scaling arguments and model results (e.g. Gillet et al., 2012) show that the dominant force balance on decadal timescales for relatively large length scales is geostrophic: a balance between pressure gradients and the Coriolis force.

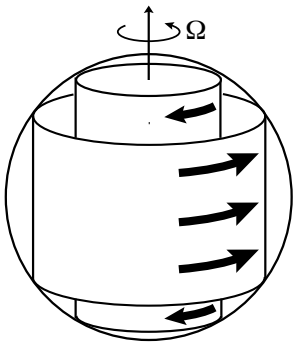

Figure 1.4: The geometry of the mean zonal flows, or geostrophic cylinders, which carry angular momentum in Earth's outer core.

1.2 Geostrophy and Angular Momentum

As discussed mathematically in Section 2.2, a geostrophic balance in the outer core has two key consequences. First, the flow field tends to be invariant, or rigid, in the direction parallel with the axis of rotation (in cylindrical (s, ϕ, z) coordinates, $\frac{\partial}{\partial z}\mathbf{u} = 0$). Second, because of this axial rigidity, the core's total axial angular momentum is contained within the azimuthal velocities of rigid cylindrical surfaces aligned with the rotation axis. The latter surfaces are termed "geostrophic cylinders", and are illustrated by Figure 1.4.

Because geostrophic cylinders are rigid and intersect the CMB, their notion can be used to calculate the outer core's total angular momentum using the core flow maps built from geomagnetic inversions. In one end of a geostrophic cylinder intersects the CMB at a latitude θ, its other end intersects the CMB at the equatorially opposite latitude $\pi - \theta$. The azimuthal velocity of the geostrophic cylinder, or its "zonal velocity", can then be calculated by averaging the azimuthal velocities on the CMB at θ and $\pi - \theta$. This is the procedure followed to generate Figure 1.5.

Figure 1.5 clearly shows exchanges of angular momentum between adjacent cylinders over the one-century period it spans. These exchanges manifest themselves in wave-like structures with periods of perhaps sixty years. This raises a new question: are these truly large-scale

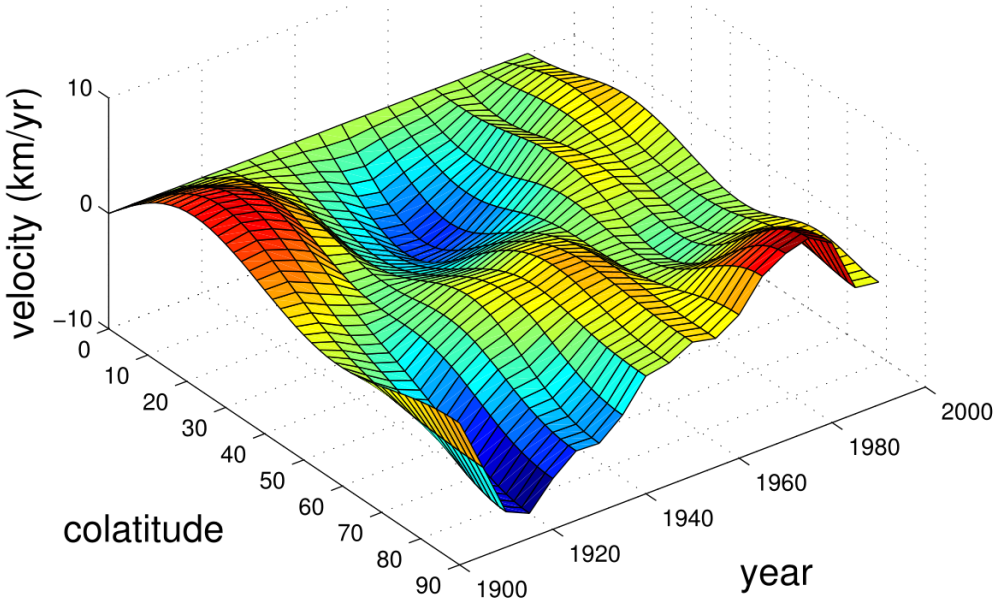

Figure 1.5: Time-varying component of the axisymmetric, equatorially symmetric, azimuthal velocity ($\overline{u_\phi}$) extracted from a core flow model. Adapted from Figure 1(a) of Zatman and Bloxham (1997).

fluctuations in the zonal velocity structure, or are they merely artifacts of the assumptions made in generating the figure? One approach to answering this question is to use information from models like that shown in Figure 1.5 to build a prediction of the core's total axial angular momentum through time, and compare the resulting timeseries to observed LOD variations. This is similar to the procedure followed by Vestine in 1953. First, however, it is instructive to discuss the mechanisms behind LOD variations in general.

1.3 Length-of-Day Variability

The LOD variation is a measure of the difference between the length of one mean solar day, defined as 86,400 seconds, and how long it takes a fixed point on Earth's surface to actually complete one revolution (e.g. Dehant and Mathews, 2015). Because relative motions in and between the individual bodies occur on geological timescales, for the purposes of this discussion Earth's surface, the remainder of the crust, and the mantle can be viewed as

forming a single solid body. "Mantle" will refer to this unified body for the remainder of this thesis. The mantle is subject to a variety of external torques Γ_i^M, including those from astronomical bodies like the moon, the sun, and Jupiter, but also including those from the atmosphere, ocean, and core-mantle interactions. The mantle is also subject to changes in its moment of inertia C_M. The relationship between Γ_i^M, C_M, time t, and the mantle's angular velocity Ω_M is

$$\frac{\partial}{\partial t}\left(C_M \Omega_M\right) = \sum_i \Gamma_i^M \,. \tag{1.7}$$

Both external torques and changes in C_M occur at a variety of amplitudes, over a variety of timescales. The most consistent influence over the longest timescales, from tens of thousands to billions of years, is the moon's gravitational field. The latter induces a tidal bulge in the Earth which, in the absence of any viscous forces in the planet, would be aligned with the sublunar point. Since viscous forces *are* present inside Earth, the tidal bulge is swept slightly ahead of the sublunar point by Earth's rotation. The resulting misalignment of mass exerts a retrograde torque on Earth, and a prograde torque on the moon. The rotation of the former is slowed, while orbit of the latter is enlarged. Optical retroflectors, left on the moon along with the Apollo Lunar Module descent stages, enabled Dickey et al. (1994) to estimate the moon's drift rate to be 3.8 cm yr^{-1}. Based on this drift rate, the corresponding lengthening in Earth's LOD should be 2.3 ms per century (Morrison and Ward, 1975; Christodoulidis et al., 1988; Stephenson and Morrison, 1995).

On medium timescales of thousands to tens of thousands of years, the most notable influence on LOD variability has been the result of glaciation. Kilometre-thick ice sheets extending from the polar regions during the latest glacial period deformed the crust and mantle beneath them. Since the glaciers began to recede some 11,700 years ago (Walker et al., 2009), both crust and mantle in the polar regions have been allowed to viscously relax back toward isostatic equilibrium. This process makes Earth less oblate, decreasing its moment of

inertia and increasing its rate of rotation (Dickey et al., 2002). The relaxation continues into the present day; Mitrovica et al. (2015) estimates its effect is a decrease in the LOD of about 1.1 ms per century. However, coupling between the core and mantle modulates this speedup, decreasing it by 0.6 ms per century (Mitrovica et al., 2015). Thus, allowing for feedback from core-mantle coupling, long-term lunar tides and medium-term glacial isostatic adjustment have combined to effect a relatively steady slowing of 1.8 ms per century for the past several thousand years (Morrison and Stephenson, 2001). Other effects, such as long-term climatological shifts, plate tectonics, and mantle convection likely influence the LOD on medium and long timescales as well, though to a much smaller degree (Gross, 2015).

The moon's influence also plays a leading role on the shortest timescales. The misalignment between its orbital axis and Earth's rotation axis causes a strong monthly signal, and the differing viscous properties of water and rock change Earth's moment of inertia throughout a single day as regions dominated by one or the other rotate through the moon's tidal influence. In addition, the moon's orbit precesses about the ecliptic every 18.6 years, contributing a decadal signal as well (Dehant and Mathews, 2015). Meanwhile, seasonal LOD variability is dominated by changes in atmospheric angular momentum (Rosen and Salstein, 1991) and ocean currents (Marcus et al., 1998).

Clearly, there are many ways in which the LOD can be influenced; only a few of them have been discussed here. The unexplained signal described by Brouwer (1952) was the result of removing the known effects – at that time, mainly the effect of the moon and atmosphere – from the raw LOD signal. What was left over must be the signature of changes in the core's axial angular momentum. A more sophisticated version of this procedure was used to generate the solid black line of Figure 1.6, showing the remnant of the LOD signal left over once all other effects are removed.

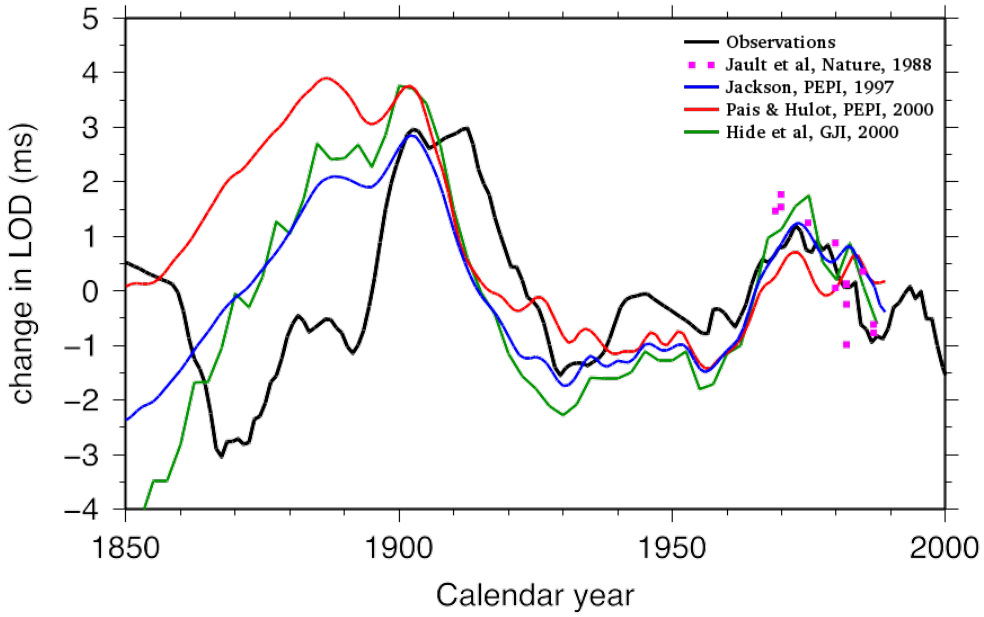

Figure 1.6: Predicted change in the length of day based on geostrophic core flows. Coloured lines: predictions from models. Black line: observation of actual LOD change. Data from Jault et al. (1988) (pink dots), Jackson (1997) (blue line), Pais and Hulot (2000) (red line), and Hide et al. (2000) (green line). Modified from Figure 9 in Finlay et al. (2010).

1.4 Agreement of Observation and Prediction

The core's total axial angular momentum may be calculated from geomagnetic core flow inversions simply by integrating the zonal velocities of geostrophic cylinders (see section 2.2.2). The resulting timeseries can then be transformed into a prediction of the variation in LOD using the relative moments of inertia of the core and mantle[6]. This produces the LOD predictions shown by the coloured dots and lines of Figure 1.6.

LOD predictions and the observations of LOD are remarkably well-correlated in Figure 1.6, especially over the past several decades when both the quality and quantity of geomagnetic data has increased. This correlation strongly indicates that the assumptions upon which LOD predictions are based are valid. In particular, it demonstrates that, to leading order,

[6]This ignores the slight modification the higher density of the solid inner core provides to the moment of inertia. However, while the entire core's axial moment of inertia is about 9×10^{36} km m^2, that of the inner core is only about 6×10^{34} kg m^2, or 0.7% that of the outer core (e.g. Mathews et al., 1991). Therefore, the denser inner core is insignificant in the angular momentum budget of the core as a whole.

core flows are indeed geostrophic on timescales of decades to centuries.

1.5 Unexplained Variability

While many of the features in the LOD observations are well-characterized, some features lack a clear mechanisms by which they are generated by the outer core. In particular, there are variations with characteristic timescales of 6 years (Holme and de Viron, 2013; Chao et al., 2014) and 60 years (e.g. Vestine and Kahle, 1968) in both $\overline{u_\phi}$ (Figure 1.5) and in the length-of-day signal (Figure 1.6).

Scale analysis shows that zonal accelerations of geostrophic cylinders (called simply "zonal accelerations" for the remainder of this thesis) must be driven by magnetic, rather than inertial or viscous, forces. However, integration of the momentum equation (see Eq.(B.12)) over the surface of a geostrophic cylinder causes the pressure, buoyancy, and Coriolis terms to vanish. If to first order inertia and viscosity are neglected, it is implied that a steady-state solution is possible only if the averaged Lorentz force also vanishes. In other words, the mean Lorentz torque on any given geostrophic cylinder must be zero. This is known as Taylor's condition (Taylor, 1963), with systems obeying it said to be in a Taylor state. Reinstating inertia, perturbations in the magnetic field – and, therefore, in the Lorentz torque – can be accommodated by zonal accelerations of the geostrophic cylinder.

Taylor's condition enables the generation of waves by differential rotation of geostrophic cylinders. Such rotation shears radial magnetic field lines, as shown in Figure 1.7. By Lenz's law, Lorentz forces are induced to oppose this shear and brake the differential rotation. However, because geostrophic cylinders have mass, inertial accelerations cause them to overshoot their equilibrium point. The wave motion resulting from this balance between inertial and

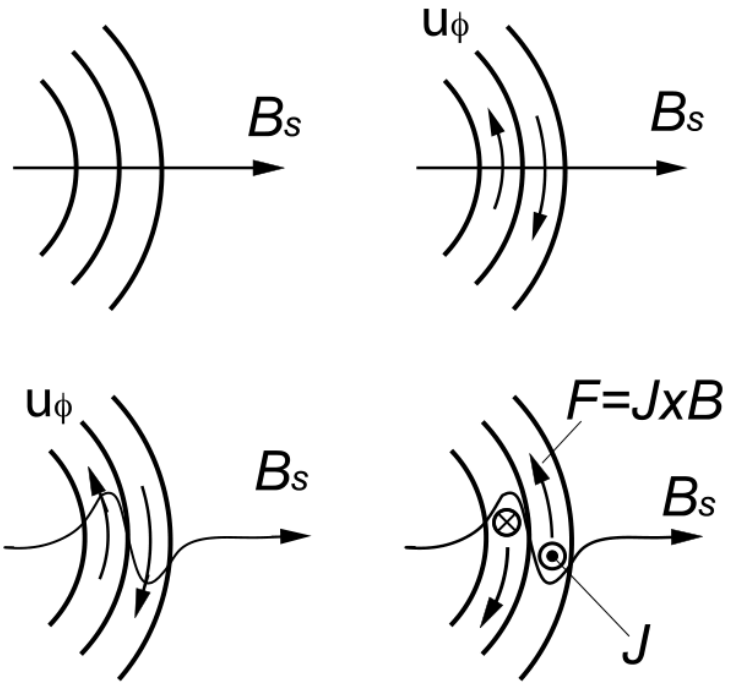

Figure 1.7: Concentric geostrophic cylinders threaded with a radial magnetic field B_s, viewed from above in the $\mathbf{e}_z$-direction. Top left: unperturbed system. Top right: differential rotation u_ϕ between cylinders. Bottom left: differential rotation shears the original B_s field, creating a perturbation b_ϕ field in the $\mathbf{e}_\phi$-direction. Bottom right: Curvature in the magnetic field induces $\mathbf{e}_z$-currents, causing a Lorentz force to oppose the original differential rotation of the cylinders. Modified from Figure 3 of Dumberry (2008).

Lorentz forces is called an Alfvén wave. Free Alfvén waves propagate radially across the set of geostrophic cylinders at the Alfvén velocity

$$u_A = \frac{|\mathbf{B}|}{\sqrt{\rho_0 \mu_0}}\,, \tag{1.8}$$

where $|\mathbf{B}|$ is the average of the cylindrically radial magnetic field over the surface of a geostrophic cylinder, ρ_0 is the fluid density, and μ_0 is the permeability of free space. In Earth's core, this type of free Alfvén wave is termed a *torsional oscillation*.

Torsional oscillations were proposed by Braginsky (1970) as the mechanism responsible for the 60-year LOD variations. In order to have the correct characteristic timescale, he found that the radial magnetic field within the outer core would have to be about equal to the

0.3 mT observed at the CMB. However, more recent work has suggested that the internal magnetic field strength is closer to ten times that observed at the CMB (e.g. Christensen, 2006; Gillet et al., 2010). Since this corresponds to free Alfvén waves with a six-year period, it is now thought that torsional oscillations are responsible for the 6-yr LOD variability. This leaves the mechanism responsible for the 60-year variability in $\overline{u_\phi}$ shown by Figure 1.5, and the 60-year variability in LOD shown by Figure 1.6, unexplained.

One possibility is that the decadal zonal accelerations may not reflect deep seated rigid flows at all, but are instead free Magnetic-Archemedian-Coriolis (MAC) waves in a stratified layer at the top of the core (Buffett, 2014; Buffett et al., 2016). The zonal flows of such MAC waves are characterized by a shear in the axial direction: flow at the CMB does not reflect flow deeper in the core. Despite it being more difficult to build a prediction of LOD changes based only on the flows at the CMB, it is nevertheless possible that, when properly taking into account the coupling of flows in the bulk of the core with these MAC waves, a prediction of core angular momentum change may be constructed so as to match the observed LOD variations (Buffett et al., 2016). However, the very fact that a very good match between the observed changes in the LOD and those predicted on the basis of purely rigid zonal flows suggests that deviations from rigidity are limited.

A alternative explanation is that the zonal accelerations are not free oscillations at all, but are forced by an underlying, dynamical mechanism. If convection were to continually induce perturbations of the internal magnetic field, the magnetic perturbations would be balanced by continually excited zonal accelerations. Assuming this is the case, the forcing must occur on timescales longer than the propagation time of free Alfvén waves. In other words, the typical convective velocity u_C must be smaller than u_A, such that the Alfvén number

$$\mathcal{A} = \frac{u_C}{u_A} \tag{1.9}$$

is $\ll 1$. Typical flow velocities in Earth's core are of the order of $u_C = 10$ km yr^{-1} (e.g. Holme and Olsen, 2006), while a typical radial magnetic field of about 3 mT (e.g. Gillet et al., 2010; Buffett, 2010), an outer core density of 10^4 kg m^{-3} (e.g. Dziewonski and Anderson, 1981), and $\mu_0 = 4\pi \times 10^{-7}$ N A^{-2} produces an Alfvén velocity (using Eq.(1.8)) of about 840 km yr^{-1}. Thus, the Alfvén number of the outer core is about $\mathcal{A} \approx 0.01$.

While such a low Alfvén number implies a significant separation between the eddy and Alfvén timescales, it does not say anything about the relative strength of magnetic and inertial forces. However, inspection of the relevant terms in the Navier-Stokes equation shows that the magnetic force strength is proportional to the square of the magnetic field, and that the inertial force strength is proportional to the square of velocity (see Section 2.3). The ratio of their strengths is therefore the square of the ratio between magnetic and velocity field strengths. As will be shown in Section 3.4.4, this ratio turns out to be equivalent to the Lundquist number, Lu. Formally, Lu is the ratio of how quickly magnetic information can be transmitted compared to how quickly it is dissipated. With τ_{d_b} as the timescale of magnetic diffusion and τ_a as the timescale needed for a free Alfvén wave to cross a distance ℓ, the Lundquist number is defined as

$$\mathrm{Lu} = \frac{\tau_{d_b}}{\tau_a} \approx \frac{\ell u_A}{\eta}\,. \tag{1.10}$$

Using $\ell \approx 10^6$ m, corresponding to the typical eddy size in the outer core, and a magnetic diffusivity of 0.5 m^{2}s^{-1} implies an Lu in excess of 5×10^4. Clearly, magnetic forces play a dominant role in large-scale dynamics.

Given the low $\mathcal{A}$ and high Lu of the outer core, it is likely that the decadal-timescale zonal accelerations observed in it are driven by time-dependent Lorentz torques, with the time dependency stemming from the continual evolution of the underlying convective flow structure. Exploring the viability of this mechanism using a numerical model is the overarching

goal of this thesis.

1.6 Strategy

One approach to numerically demonstrate this mechanism would be to tune an existing three-dimensional, self-sustaining dynamo model to produce the expected eddy-induced, magnetically-forced waves. However, existing models are capable of achieving only relatively high Alfvén numbers of approximately 1, meaning the dynamics of free and forced magnetically-driven zonal accelerations are not well separated. Some recent 3D models have been able to achieve lower values of $\mathcal{A} \approx 0.1$ (e.g. Aubert et al., 2017; Schaeffer et al., 2017), though at the disadvantage of being very numerically demanding.

An alternative approach is to build a highly idealized model of geostrophically-dominated magnetoconvection within the existing framework of quasi-geostrophic (QG) convection models (e.g. Busse and Or, 1986; Cardin and Olson, 1994; Aubert et al., 2003). The QG approximation assumes the flow is to first order in a geostrophic balance, allowing the full three-dimensional magnetohydrodynamic equations to be collapsed onto a two-dimensional domain. We modify a QG model of thermally-driven convection by adding an induction equation to track the evolution of the magnetic field as it is sheared and advected by the flow. Because a self-sustaining dynamo cannot be sustained in only two dimensions (e.g. Cowling, 1957; Roberts, 2015), a steady background magnetic field is imposed on the model. The induction equation serves to track perturbations to this background field. The magnetic field is then allowed to feed back on the flow field via the Lorentz force, although in practice we limit its effect to only the zonal velocity field (see Section 4.1).

We are thus able to conduct a magnetoconvection experiment at comparatively modest nu-

merical cost. Previous studies have shown that Boussinesq QG models with thermal forcing are capable of reproducing flow patterns similar in scale and behaviour to the ones we expect in planetary cores (e.g. Aubert et al., 2003; Gillet and Jones, 2006). However, these models have not been used to investigate the generation of magnetically-forced zonal flows.

Our strategy to do so is to tune the model to produce an Earth-like $\mathcal{A} \approx 0.01$. Convective velocities are then smaller than Alfvén velocities by a factor of about 100, implying a large temporal separation between free and forced magnetically-induced zonal accelerations. We track the zonal accelerations along with the azimuthally averaged viscous, Reynolds, and magnetic torques, finding particularly strong correlations between magnetic torques and zonal accelerations. Furthermore, the timescales associated with convective eddies are found to be similar to the timescales of longer-period zonal accelerations. We therefore demonstrate that convective eddies are capable of perturbing a magnetic field such that magnetically-forced zonal accelerations are produced on timescales much longer than those of free Alfvén waves.

1.7 Scientific Advancements Contained in this Thesis

There were several key scientific advancements involved in the production of this work. First, a QG version of the induction equation was derived and used to augment the governing equations of an existing thermally-driven QG model (see Appendix D.4 and Eq.(2.41) for the non-axisymmetric version, and Appendix D.5 and Eq.(2.42) for the axisymmetric version). Second, QG versions of the magnetic torques feeding back on the flow field were derived (see Term ⑤ in Appendix D.1 for the non-axisymmetric expression, and Term ③ in Appendix D.2 for the axisymmetric expression), and incorporated into the non-axisymmetric vorticity equation (first term on the right-hand side of Eq.(2.35)) and the zonal flow equation

(Eqs.(2.39) and (2.40)).

In order to derive and implement the equations above, it was found that the form of how the magnetic perturbation field $\mathbf{b}$ was written in terms of the magnetic potential a (Eq.(2.18), or the second equation of Eq.(2.16)) had to be the same as the form of how the velocity field $\mathbf{u}$ was written in terms of the streamfunction ψ (Eq.(2.17), or the first equation of Eq.(2.16)). If it did *not* take the same form, the total axial angular momentum of the model would not be conserved. In fact, where the form of the velocity definition is dictated by the no-penetration boundary condition, writing the magnetic perturbation field in the same form implies a magnetic equivalent of the no-penetration boundary condition. Allowing for magnetic coupling at the boundaries would necessitate a change in the form of Eq.(2.18).

Once the model was implemented, it was found that in order to produce magnetically-forced, slow-timescale zonal accelerations, model parameters which produced Alfvén numbers much less than 1 and Lundquist numbers much greater than 1 had to be used. In addition, we found that the non-axisymmetric Lorentz torque had to be neglected from the non-axisymmetric vorticity equation in order to produce realistic, large-scale convective eddies (see Section 4.1). The latter was the final ingredient needed to demonstrate that convective eddies can perturb the magnetic field in such a way as to force slow zonal accelerations.

The substantial scientific contributions and interpretations of this work are presented in Chapters 4 and 5. These chapters are based directly on content submitted for publication in More and Dumberry (2017).

Chapter 2

Theory

2.1 Geometry

The three-dimensional volume of the outer core lends itself naturally to the use of the spherical coordinates (r, θ, ϕ). Figure 2.1 illustrates how two concentric spheres can be used to approximate the outer core's geometry: the inner sphere of radius r_1 represents the inner core boundary, while the outer sphere of radius r_2 represents the core-mantle boundary (CMB).

A quasi-geostrophic (QG) model takes advantage of a rapidly rotating fluid's axial rigidity (see Section 2.2) to collapse the fully three-dimensional problem onto a two-dimensional plane. This plane, equivalent to a slice through the core's equator, is represented by the grey annulus of Figure 2.1. Position on such an annular surface is easily described with the cylindrical coordinates (s, ϕ, z), where the $\mathbf{e}_z$-axis is aligned with the axis of rotation and the $z = 0$ plane is the equatorial plane. The model domain then extends from the "tangent cylinder", or the cylinder tangent to the $r = r_1$ surface, at $s = s_1$ to the "equator" at $s = s_2$. Despite the final QG model being two-dimensional, the z-coordinate is needed for axial averaging when deriving the QG equations. The region inside the tangent cylinder is not modelled[1].

[1]Unlike the 2D geometry proposed by Pratchett (1986), ours does not require four giant elephants and

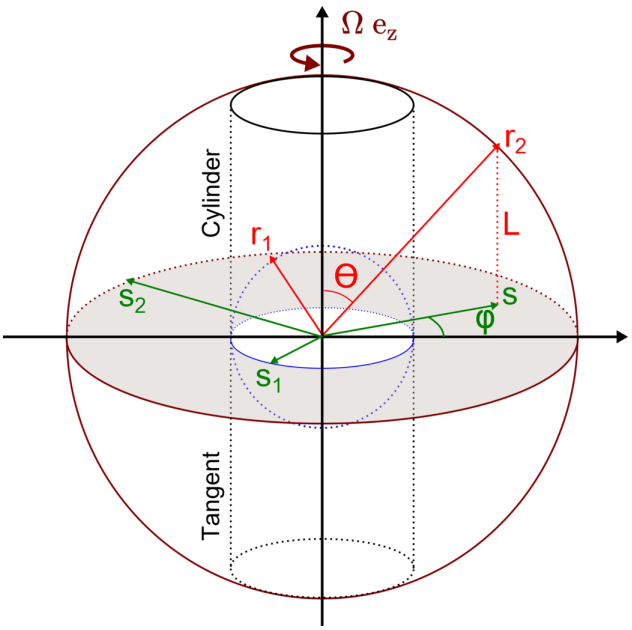

Figure 2.1: Geometry of our QG model. The domain of integration is the shaded 2D annulus between s_1 and s_2.

The half-column height L between the equatorial plane and the upper $(+)$ and lower $(-)$ boundaries is a function of s:

$$L = \sqrt{1 - s^2}\,. \tag{2.1}$$

The slope of the upper and lower boundaries plays a key role in the model's behaviour. The β parameter, equivalent to the same parameter used in the β-plane approximation common in meteorology and oceanography, describes this slope as a function of s:

$$\beta = \frac{1}{L}\frac{\partial L}{\partial s} = -\frac{s}{L^2}\,. \tag{2.2}$$

a space turtle to support itself. It does, however, have a hole in the middle, which could be thought of as either a feature or a glitch, depending on one's point of view.

2.2 Axial Rigidity

2.2.1 Axial Invariance

The dynamics of a system in geostrophic balance are dominated by pressure gradients and the Coriolis force. For rotation rate $\boldsymbol{\Omega} = \Omega \mathbf{e}_z$ relative to an inertial frame, velocity $\mathbf{u}$ relative to the rotating frame, constant density ρ_0, reduced pressure P, and gradient operator $\boldsymbol{\nabla}$, the geostrophic balance under the Boussinesq approximation (Rayleigh, 1916) is written

$$2\boldsymbol{\Omega} \times \mathbf{u} = -\frac{1}{\rho_0} \boldsymbol{\nabla} P \,. \tag{2.3}$$

Taking the curl of Eq.(2.3) causes the pressure term to vanish. Since the axis of rotation is aligned with the $\mathbf{e}_z$-axis, the left-hand side can be expanded to show that velocities do not vary in the axial direction:

$$(\mathbf{e}_z \cdot \boldsymbol{\nabla})\, \mathbf{u} = \frac{\partial}{\partial z} \mathbf{u} = \mathbf{0} \,. \tag{2.4}$$

This is the Taylor-Proudman theorem, named for its independent discovery by Taylor (1917) and Proudman (1916)[2]. It is absolute only in systems which are perfectly geostrophic. When geostrophy is violated, Eq.(2.4) is also violated as fast inertial waves transmit information axially (Jault and Finlay, 2015). However, if only small perturbations are allowed about a first-order geostrophic balance, axial variations remain small. This is the core assumption of the QG framework.

[2]It was first published twenty years earlier by Hough (1897).

2.2.2 Geostrophic Cylinders

Because of axial rigidity, the total axial angular momentum of a geostrophically-dominated system is organized in a very simple way. The total axial angular momentum $\mathcal{L}_z$ of a fluid under the Boussinesq approximation (Rayleigh, 1916) is

$$\mathcal{L}_z = \mathbf{e}_z \cdot \iiint_V \rho \mathbf{r} \times \mathbf{u} \, \mathrm{d}V \approx \rho_0 \int_s \oint_0^{2\pi} \int_{-L}^{L} (s u_\phi) \; s \, \mathrm{d}s \, \mathrm{d}\phi \, \mathrm{d}z \, . \tag{2.5}$$

Because u_ϕ is axially rigid (that is, $\frac{\partial}{\partial z} u_\phi = 0$), its axial average $\langle u_\phi \rangle$ (see Appendix A.4) is equal to its free-stream value u_ϕ. Using the definition of the azimuthal average given by Eq.(A.17), Eq.(2.5) reduces to

$$\mathcal{L}_z = 4\pi \rho_0 L \int_s s^2 \overline{u_\phi} \, \mathrm{d}s \, , \tag{2.6}$$

where $\overline{u_\phi}$ is the azimuthally averaged azimuthal velocity, or the zonal velocity. Thus, angular momentum is stored by the zonal velocities of cylindrical surfaces at each radial position s.

2.3 The Quasi-Geostrophic Model

2.3.1 Basic Equations

The governing equations for thermal convection of a conducting fluid under the Boussinesq approximation are derived in Appendix B. With primes ($'$) denoting dimensional variables which will later be nondimensionalized,

$$\frac{\partial \mathbf{u}'}{\partial t'} + (\mathbf{u}' \cdot \boldsymbol{\nabla}') \, \mathbf{u}' + 2\boldsymbol{\Omega}' \times \mathbf{u}' = -\frac{1}{\rho_0} \boldsymbol{\nabla}' P' + \nu \nabla'^2 \mathbf{u}' + \alpha g_0 \Theta' \frac{\mathbf{r}'}{r_2'} + \frac{1}{\rho_0 \mu_0} (\boldsymbol{\nabla}' \times \mathbf{B}') \times \mathbf{B}' \, , \tag{2.7}$$

Parameter	Description	Outer Core Value
r_1	radius of inner core	1220 km
r_2	radius of outer core	3480 km
μ_0	permeability of free space	$4\pi \times 10^{-7}$ H m^{-1}
Ω	rotation rate	7.3×10^{-5} s^{-1}
g_0	gravitational acceleration at CMB	10 m s^{-2}
ρ_0	reference density	10^4 kg m^3
α	thermal expansivity	1.5×10^{-5} K^{-1}
θ	local temperature perturbation	10^{-4} K
B	magnetic field strength	3 mT
ν	kinematic viscosity	1.5×10^{-6} m^2 s^{-1}
κ	thermal diffusivity	2×10^{-5} m^2 s^{-1}
η	magnetic diffusivity	0.5 m^2 s^{-1}

Table 2.1: Typical values of some key core parameters. Sources: Radius of inner and outer cores, gravity, and density from Dziewonski and Anderson (1981). Thermal expansion coefficient from Jones (2015), itself derived from Anufriev et al. (2005), which comes from Braginsky and Roberts (1995). Local temperature perturbation from Anufriev et al. (2005). Magnetic field strength from Gillet et al. (2010) and Buffett (2010). Kinematic viscosity from de Wijs et al. (1998). Thermal diffusivity calculated from the thermal conductivity of (Pozzo et al., 2012), the density of Dziewonski and Anderson (1981), and the heat capacity of Anufriev et al. (2005). Magnetic diffusivity calculated from the electrical conductivity of Pozzo et al. (2012).

$$\frac{\partial T'}{\partial t'} = -\left(\mathbf{u}' \cdot \boldsymbol{\nabla}'\right) T' + \kappa \nabla'^2 T' \,, \tag{2.8}$$

$$\frac{\partial \mathbf{B}'}{\partial t'} = \boldsymbol{\nabla}' \times \left(\mathbf{u}' \times \mathbf{B}'\right) + \eta \nabla'^2 \mathbf{B}' \,, \tag{2.9}$$

$$\boldsymbol{\nabla}' \cdot \mathbf{u}' = 0, \quad \boldsymbol{\nabla}' \cdot \mathbf{B}' = 0 \,. \tag{2.10}$$

Here, the thermal expansivity α, gravitational acceleration at the CMB g_0, kinematic viscosity ν, thermal diffusivity κ, permeability of free space μ_0, magnetic diffusivity η, magnetic field $\mathbf{B}$, and time t join the already-defined quantities $\mathbf{u}$, Ω, P, $\mathbf{r}$, r_2, and ρ_0. Representative values in the outer core for the physical parameters are given in Table 2.1.

Eqs.(2.7) - (2.10) are nondimensionalized using the scalings shown in Table 2.2: length by

Dimension	Scale Choice	Approximate Value
$\mathcal{L}$ (length)	r_2	3×10^6 m
$\mathcal{T}$ (time)	Ω^{-1}	7×10^{-5} s^{-1}
$\mathcal{U}$ (velocity)	$\mathcal{L}\mathcal{T}^{-1} = r_2\Omega$	250 m s^{-1}
ΔT (temperature)	$T_1 - T_2$	10^{-4} K
$\mathcal{B}$ (magnetic field)	$r_2\Omega\sqrt{\rho_0\mu_0}$	30 T
$\mathcal{P}$ (pressure)	$\rho_0\mathcal{U}^2 = \rho_0 r_2^2\Omega^2$	0.6 GPa

Table 2.2: Definition of the scalings used in nondimensionalizing the basic equations. Typical values are calculated using the the data in Table 2.1. As per Jones (2015), ΔT is assumed to be of the same order as local temperature perturbations.

the radius of the outer sphere r_2, time by the reciprocal rotation rate Ω^{-1}, velocity by $r_2\Omega$, temperature by the superadiabatic temperature difference between outer and inner spheres ΔT, the magnetic field by $r_2\Omega\sqrt{\rho_0\mu_0}$, and pressure by $\rho_0 r_2^2\Omega^2$. As shown in Appendix C, Eqs.(2.7) - (2.10) then become

$$\frac{\partial \mathbf{u}}{\partial t} + (\mathbf{u}\cdot\boldsymbol{\nabla})\,\mathbf{u} + 2\mathbf{e}_z \times \mathbf{u} = -\boldsymbol{\nabla} P + E\nabla^2\mathbf{u} + Ra^*\Theta\mathbf{r} + (\boldsymbol{\nabla}\times\mathbf{B})\times\mathbf{B}\,, \tag{2.11}$$

$$\frac{\partial T}{\partial t} = -\,(\mathbf{u}\cdot\boldsymbol{\nabla})\,T + \frac{E}{P_r}\nabla^2 T\,, \tag{2.12}$$

$$\frac{\partial \mathbf{B}}{\partial t} = \boldsymbol{\nabla}\times(\mathbf{u}\times\mathbf{B}) + \frac{E}{P_m}\nabla^2\mathbf{B}\,, \tag{2.13}$$

$$\boldsymbol{\nabla}\cdot\mathbf{u} = 0, \quad \boldsymbol{\nabla}\cdot\mathbf{B} = 0\,. \tag{2.14}$$

Notice that the primes have now been dropped – all variables are now nondimensional. The information previously contained by the physical parameters (e.g. ρ_0, g_0, etc.) is now contained in the nondimensional parameters E (Ekman number), Ra^* (modified Rayleigh number), P_r (Prandtl number), and P_m (magnetic Prandtl number). Typical values in the outer core for each nondimensional parameter are given in Table 2.3.

Constant	Name	Outer Core Value
$E = \frac{\nu}{\Omega r_2^2}$	Ekman number	10^{-15}
$P_r = \frac{\nu}{\kappa}$	Prandtl number	0.1
$Ra = \frac{\alpha g_0 \Delta T r_2^3}{\nu\kappa}$	Rayleigh number	10^{22}
$Ra^* = E^2 Ra P_r^{-1}$	Modified Rayleigh number	10^{-6}
$P_m = \frac{\nu}{\eta}$	Magnetic Prandtl number	10^{-6}

Table 2.3: Nondimensional parameter definitions. Values for the outer core calculated from data in Table 2.1.

2.3.2 Representation of Fields

The magnetic and temperature fields are each decomposed into background $(T_0, \mathbf{B}_0)$ and perturbation $(\Theta, \mathbf{b})$ components. The background fields are fixed in time, while the perturbation fields vary in time. Thus, for an arbitrary position $\mathbf{x}$,

$$T(t,\mathbf{x}) = T_0(\mathbf{x}) + \Theta(t,\mathbf{x})\,, \quad \mathbf{B}(t,\mathbf{x}) = \mathbf{B}_0(\mathbf{x}) + \mathbf{b}(t,\mathbf{x})\,. \tag{2.15}$$

The horizontal components of a vector field or operator are specified by an H subscript. For example, the horizontal components of the gradient operator in cylindrical coordinates are $\nabla_H = \mathbf{e}_s \frac{\partial}{\partial s} + \mathbf{e}_\phi \frac{1}{s}\frac{\partial}{\partial \phi}$. In their final QG form, the horizontal, nonaxisymmetric components of the velocity $(\mathbf{u}_H = (u_s, u_\phi))$ and magnetic perturbation $(\mathbf{b}_H = (b_s, b_\phi))$ fields are assumed to be rigid. In addition, according to Eq.(2.14), both $\mathbf{u}$ and $\mathbf{b}$ are solenoidal, allowing them to be written in terms of the toroidal scalar functions ψ and a, respectively. The QG $\mathbf{u}$ and $\mathbf{b}$ fields are then defined as

$$\mathbf{u} = \overline{u_\phi}\mathbf{e}_\phi + \frac{1}{L}\boldsymbol{\nabla} \times (L\psi \mathbf{e}_z) + u_z \mathbf{e}_z\,, \quad \mathbf{b} = \overline{b_\phi}\mathbf{e}_\phi + \frac{1}{L}\boldsymbol{\nabla} \times (La\mathbf{e}_z) + b_z \mathbf{e}_z\,. \tag{2.16}$$

Overbars denote an azimuthal average (see Appendix A.3). Thus, $\overline{u_\phi}$ and $\overline{b_\phi}$ are the zonal flow and zonal magnetic fields, respectively, and are assumed to be rigid. Note that, due to mass conservation and magnetic flux conservation, there are no $\overline{u_s}$ or $\overline{b_s}$ components.

With $\nabla_H^2 = \frac{\partial^2}{\partial s^2} + \frac{1}{s}\frac{\partial}{\partial s} + \frac{1}{s}\frac{\partial}{\partial \phi}$ (see Eq.(A.13) in Appendix A.1), the components of $\mathbf{u}_H$, along with the axial vorticity field $\omega_z \mathbf{e}_z = \boldsymbol{\nabla} \times \mathbf{u}_H$, may be explicitly written

$$u_s = \frac{1}{s}\frac{\partial \psi}{\partial \phi}\,, \quad u_\phi = \overline{u_\phi} - \left(\frac{\partial}{\partial s} + \beta\right)\psi\,, \quad \omega_z = \left(2\frac{\overline{u_\phi}}{s} + \frac{\partial}{\partial s}\overline{u_\phi}\right) - \nabla_H^2 \psi - \frac{1}{s}\frac{\partial}{\partial s}\left(s\beta\psi\right)\,. \tag{2.17}$$

Similarly, the components of $\mathbf{b}_H$, along with the the axial current density field $j_z \mathbf{e}_z = \boldsymbol{\nabla} \times \mathbf{b}_H$, may be written

$$b_s = \frac{1}{s}\frac{\partial a}{\partial \phi}\,, \quad b_\phi = \overline{b_\phi} - \left(\frac{\partial}{\partial s} + \beta\right)a\,, \quad j_z = \left(2\frac{\overline{b_\phi}}{s} + \frac{\partial}{\partial s}\overline{b_\phi}\right) - \nabla_H^2 a - \frac{1}{s}\frac{\partial}{\partial s}\left(s\beta a\right)\,. \tag{2.18}$$

The presence of β in both Eq.(2.17) and Eq.(2.18) shows the influence of the upper and lower boundary geometry on the velocity and magnetic fields. The forms of u_s, u_ϕ, and ω_z used in this model are similar to those used in traditional QG models (e.g. Schaeffer and Cardin, 2005). Choosing similar forms for b_s, b_ϕ, and j_z follows the strategy employed by, for example, Labbé et al. (2015).

2.3.3 Assumptions

The fundamental assumption needed to transform Eqs.(2.11)-(2.14) into their QG form is that the QG approximation itself holds. In practice, this implies (1) that horizontal velocities are rigid (and therefore the scalar potential ψ from which they are calculated is also rigid); (2) that the axial component of vorticity is rigid; and (3) that the horizontal components of vorticity are insignificant compared to the axial component. However, because of the no-penetration condition on the upper and lower spherical boundaries, an axial dependence in u_z is needed if nonzero values of u_s are to be allowed. Defining the unit vector normal to the upper and lower boundaries as $\hat{\mathbf{n}} = s\mathbf{e}_s \pm L\mathbf{e}_z$, the no-penetration boundary condition

holds that

$$\mathbf{u} \cdot \hat{\mathbf{n}}|_{z=\pm L} = 0\,, \tag{2.19}$$

implying that

$$u_z|_{z=\pm L} = \mp \frac{s}{L} u_s\,. \tag{2.20}$$

Eq.(2.20) shows that, since u_s is assumed to be perfectly rigid, the axial velocity has the same magnitude but opposite sign at the upper and lower boundaries. The simplest profile of u_z which produces this relationship is linear and antisymmetric about the equator:

$$u_z = -\frac{s}{L}\frac{z}{L} u_s = \beta u_s z\,. \tag{2.21}$$

Unlike the velocity field, the magnetic perturbation field is not dynamically constrained to remain rigid. However, because the horizontal velocity field which causes magnetic perturbations *is* rigid, we make the assumption that the horizontal magnetic perturbations (along with the scalar potential a from which they are calculated) are also rigid. This significantly simplifies the model, while still allowing the interactions between the convective and magnetic fields needed to magnetically force zonal accelerations. Also in analogy with the velocity field, it is assumed that the horizontal components (j_s, j_ϕ) of the perturbation current density are insignificant compared to the dominant, rigid j_z component.

Again on grounds of simplicity, we assume the upper and lower spherical boundaries have zero resistivity. This imposes the magnetic version of the no-penetration boundary condition on $\mathbf{b}$. An axial variation in b_z must therefore exist to allow nonzero values of b_s. Using the same technique which produced the axial profile of u_z (Eq.(2.21)), we take this profile to be

$$b_z = \beta b_s z\,. \tag{2.22}$$

A mantle with zero resistivity is likely nonphysical in the case of Earth: it implies a lack of electromagnetic core-mantle coupling, and is inconsistent with the perfectly insulating (i.e. infinitely resisting) mantle needed for geomagnetic core flow inversions (Section 1.1). However, our model is intended to study the interplay of mechanical and magnetic forces in a conducting fluid dominated by rotation, not to serve as a perfect analog to the outer core. In this idealized context, it is convenient to choose the simplest boundary conditions, rather than the most realistic. While assuming zero resistivity on the spherical boundaries produces a model less capable of producing realistic behaviour near those boundaries, the effects most of interest to this project occur in the bulk of the fluid, away from the boundaries. In addition, as shown in Appendix F, assuming the b_z profile of Eq.(2.22) is required for the model is to conserve angular momentum.

The magnetic background field is subject to a number of restrictions. Being a magnetic field, it is assumed to be divergence-free ($\boldsymbol{\nabla} \cdot \mathbf{B}_0 = 0$). It is also assumed to be curl-free ($\mathbf{J}_0 = \boldsymbol{\nabla} \times \mathbf{B}_0 = \mathbf{0}$) and harmonic ($\nabla^2 \mathbf{B}_0 = \mathbf{0}$) so as not to impart a Lorentz force or a magnetic perturbation in the absence of convection.

In practice, while assuming the above for the purposes of deriving the QG equations, the background field actually used in the model is somewhat simplified. In particular, while the time-averaged toroidal component of the outer core's magnetic field is likely very significant, we assume $B_{0\phi} = 0$. B_{0s} and B_{0z} are taken to be axisymmetric, with the former assumed to be rigid and the latter chosen so as to obey the magnetic no-penetration boundary condition. The latter is decidedly incorrect in the case of Earth: a steady component of the core-induced magnetic field is observed at Earth's surface on timescales of centuries, so the "background" field in the outer core must also steadily penetrate the CMB. However, adopting a no-penetration condition on the background field makes the equations slightly simpler. Therefore, in analogy with the axial profile of b_z, we take $B_{0z} = \beta B_{0s} z$.

The governing equations are significantly simplified by making use of the Boussinesq approximation (Rayleigh, 1916). This assumes density-dependent differences in inertia are small compared to density-dependent differences in buoyancy. The key outcome of this assumption is that all densities (ρ) in the governing equations are replaced with a single reference density (ρ_0), except in the buoyancy term. In addition to filtering sound waves out of the model, the assumption of constant density allows the full continuity equation (the left-hand equation of Eqs.(B.2)) to be simplified to the $\boldsymbol{\nabla} \cdot \mathbf{u} = 0$ of Eq.(2.14). The Boussinesq approximation is generally applicable only to fluids whose densities are relatively constant throughout, while densities in the outer core differ significantly between the inner core boundary and the CMB. Nevertheless, previous QG models have shown a Boussinesq approach to work reasonably well for the outer core (e.g. Aubert et al., 2003; Gillet and Jones, 2006).

The model assumes convection to be driven purely by a superadiabatic temperature difference between the inner core boundary and the CMB – that is, there is no compositional buoyancy, and no heat sources (i.e. radioactive elements) contained in the fluid itself. Since the Boussinesq approximation implies the heat capacity of the fluid is the same everywhere, the usual heat equation may be replaced with the simpler temperature equation of Eq.(2.12). Density for calculating the buoyancy term of Eq.(2.11) is assumed to depend linearly on the temperature perturbation, with the same thermal expansion coefficient everywhere[3]. To prevent such temperature perturbations from occurring in the absence of convection, the background (conducting) temperature profile T_0 of Eq.(2.15) is assumed to be harmonic ($\nabla^2 T_0 = 0$). Finally, the strength of gravity, which multiplies the density perturbation to give the total buoyancy force, is assumed to vary linearly with the spherically radial distance r.

[3]In fact, this coefficient (α) is estimated to vary by roughly a factor of two between the inner core boundary and the CMB (e.g. Braginsky and Roberts, 1995).

2.3.4 Boundary Conditions

Two conditions are needed on each of the inner ($s = s_1$) and outer ($s = s_2$) boundaries for the velocity streamfunction ψ. The first is provided by the no-slip boundary condition, requiring that $\frac{\partial \psi}{\partial s} = 0$. The second is provided by the no-penetration boundary condition, requiring ψ be constant. For convenience, we choose the constant to be zero ($\psi = 0$), which also ensures that no mean zonal flow is contained within ψ. Instead, as shown by Eq.(2.17), the zonal flow is explicitly represented by $\overline{u_\phi}$.

A single condition in needed on each boundary for $\overline{u_\phi}$. We choose the stress-free condition $\frac{\partial}{\partial s}\left(\frac{\overline{u_\phi}}{s}\right) = 0$. The zonal magnetic field $\overline{b_\phi}$ also requires a single condition on each boundary; we choose to use the magnetic equivalent of the stress-free condition, $\frac{\partial}{\partial s}\left(\frac{\overline{b_\phi}}{s}\right) = 0$.

A single condition is needed on each boundary for the magnetic potential function a. For simplicity, we choose to set $a = 0$ at both $s = s_1$ and $s = s_2$. Since $b_s = \frac{1}{s}\frac{\partial}{\partial \phi} a$ (Eq.(2.18)), this is equivalent to a no-penetration boundary condition on b_s.

The temperature equation requires a single condition on each boundary. We demand $\Theta = 0$ on both. In addition, we set the superadiabatic temperature on the inner boundary to $T_1 = 1$, and the superadiabatic temperature on the outer boundary to $T_2 = 0$. ΔT is therefore 1.

2.3.5 Transformation to QG

The QG equivalent of the momentum equation (Eq.(2.11)) is the axial vorticity equation. It is derived in Appendix D.1 by taking the curl of Eq.(2.11), keeping only the axial component.

The latter is then axially averaged to produce the QG vorticity equation[4]:

$$\frac{\partial \omega_z}{\partial t}+\left(u_s\frac{\partial}{\partial s}+\frac{u_\phi}{s}\frac{\partial}{\partial \phi}\right)\omega_z-(2+\omega_z)\,\beta u_s=\left(B_s\left(\frac{\partial}{\partial s}-\beta\right)+\frac{B_\phi}{s}\frac{\partial}{\partial \phi}\right)j_z+E\,\nabla_H^2\omega_z-Ra^*\frac{\partial}{\partial \phi}\langle\Theta\rangle\ . \tag{2.23}$$

Notably, u_z is *not* explicitly tracked, as it depends only on u_s via Eq.(2.21). Because all quantities in Eq.(2.23) have been axially averaged, they depend only on s and ϕ. The temperature perturbation is kept within angled brackets simply to emphasize this point.

While in principle Eq.(2.23) contains all of the velocity field's information, we are constructing this model to study the zonal accelerations of geostrophic cylinders. It is therefore convenient to derive a separate equation for the zonal velocity. As shown in Appendix D.2, this is done by taking the $\mathbf{e}_\phi$-component of Eq.(2.11), then averaging it axially and azimuthally. The result is

$$\frac{\partial}{\partial t}\left(\overline{\frac{u_\phi}{s}}\right)=\Gamma_\mathrm{V}+\Gamma_\mathrm{R}+\Gamma_{\mathrm{L}_1}+\Gamma_{\mathrm{L}_2}\,, \tag{2.24}$$

where Γ_V, Γ_R, Γ_{L_1}, and Γ_{L_2} are, respectively torques from viscous drag, Reynolds stresses, the axisymmetric Lorentz force[5], and Maxwell stresses:

$$\Gamma_\mathrm{V}=\frac{E}{s^3L}\frac{\partial}{\partial s}\left(s^3L\frac{\partial}{\partial s}\left(\overline{\frac{u_\phi}{s}}\right)\right) \tag{2.25}$$

$$\Gamma_\mathrm{R}=-\overline{\frac{u_s}{s^2}\frac{\partial}{\partial s}\left(su_\phi\right)} \tag{2.26}$$

$$\Gamma_{\mathrm{L}_1}=\frac{1}{s^3L}\frac{\partial}{\partial s}\left(s^3LB_{0s}\left(\overline{\frac{b_\phi}{s}}\right)\right) \tag{2.27}$$

$$\Gamma_{\mathrm{L}_2}=\overline{\frac{b_s}{s^2}\frac{\partial}{\partial s}\left(sb_\phi\right)}\,. \tag{2.28}$$

[4]The linearly-varying u_z specified by Eq.(2.21) produces significant horizontal vorticity, but those components are antisymmetric across the equatorial plane. Their axial averages therefore vanish.

[5]For want of a better term.

It should be noted that the *total* Lorentz torque is the sum of the axisymmetric Lorentz torque and the Maxwell stresses, such that $\Gamma_{\mathrm{L}} = \Gamma_{\mathrm{L}_1} + \Gamma_{\mathrm{L}_2}$. In practice, Eq.(2.24) is used to calculate the zonal flow, and Eq.(2.23) is used to calculate non-axisymmetric vorticity.

The QG induction equation is derived in Appendix D.4 from the $\mathbf{e}_s$-component of the full induction equation, Eq.(2.13). By recasting $\mathbf{b}$ in terms of its potential function a, each side of the resulting equation is operated upon by $\frac{1}{s}\frac{\partial}{\partial\phi}$. Since the quantities being operated upon must then be equal to one another, the $\frac{1}{s}\frac{\partial}{\partial\phi}$ term vanishes to produce

$$\frac{\partial}{\partial t}a = (u_s B_\phi - u_\phi B_s) + \frac{E}{P_m}\left(\nabla_H^2 a + \frac{2\beta a}{s}\right) . \tag{2.29}$$

Similar to the QG vorticity equation, Eq.(2.29) contains, in principle, all magnetic perturbation field information. However, it is again convenient to use a separate, explicit equation for the zonal magnetic field. In Appendix D.5, the azimuthal component of Eq.(2.13) is extracted, then azimuthally and axially averaged to produce

$$\frac{\partial}{\partial t}\left(\frac{\overline{b_\phi}}{s}\right) = -\frac{1}{s}\left(\frac{\partial}{\partial s} + \beta\right)\left(\overline{u_s B_\phi} - \overline{u_\phi B_s}\right) + \frac{1}{s^3}\frac{E}{P_m}\frac{\partial}{\partial s}\left(s^3\frac{\partial}{\partial s}\left(\frac{\overline{b_\phi}}{s}\right)\right) . \tag{2.30}$$

If the operator which converts the magnetic potential field a to the azimuthal perturbation field b_ϕ is (from Eq.(2.18)) $\mathcal{H} = -\left(\frac{\partial}{\partial s} + \beta\right)$, the first term on the right-hand side of Eq.(2.30) is equivalent to applying $\mathcal{H}$ to the first term of Eq.(2.29), azimuthally averaging, and dividing by s, precisely as may be expected. Eq.(2.30) may be written more compactly with reference to Eq.(A.14) as

$$\frac{\partial}{\partial t}\left(\frac{\overline{b_\phi}}{s}\right) = \frac{1}{sL}\frac{\partial}{\partial s}\left(L\left(\overline{u_\phi B_s} - \overline{u_s B_\phi}\right)\right) + \frac{1}{s^3}\frac{E}{P_m}\frac{\partial}{\partial s}\left(s^3\frac{\partial}{\partial s}\left(\frac{\overline{b_\phi}}{s}\right)\right) . \tag{2.31}$$

In practice, Eq.(2.31) is used to evolve the zonal magnetic perturbation field, while Eq.(2.29) is used to evolve the non-axisymmetric magnetic potential.

The temperature field is fully three-dimensional and is not subject to the Taylor-Proudman theorem. However, the temperature perturbation only enters the vorticity Eq.(2.23) as an axially averaged quantity. It is therefore acceptable to track only the axially-averaged quantity itself. As shown in Appendix D.3, the axial average of Eq.(2.12) is

$$\frac{\partial}{\partial t}\left\langle \Theta \right\rangle = -u_s \frac{\partial}{\partial s}\left\langle T_0 \right\rangle - \mathbf{u}_H \cdot \left(\boldsymbol{\nabla}_H \left\langle \Theta \right\rangle \right) + \frac{E}{P_r} \nabla_H^2 \left\langle \Theta \right\rangle \ . \tag{2.32}$$

For the remainder of this thesis, Θ will be assumed to have been axially averaged, and therefore the angled brackets around it will be neglected. The background profile $\langle T_0 \rangle$ is calculated from the Laplace equation. In spherical coordinates, if the inner sphere is held at temperature T_1 and the outer sphere at T_2 (so $\Delta T = T_1 - T_2$),

$$\nabla^2 T_0 = \frac{1}{r^2}\frac{\partial}{\partial r}\left(r^2 \frac{\partial}{\partial r} T_0 \right) = 0 \quad \Rightarrow \quad T_0 = T_2 + \Delta T \left(\frac{1 - \frac{1}{r}}{1 - \frac{1}{r_1}} \right) . \tag{2.33}$$

However, only the cylindrically radial derivative of the axially averaged background field is needed in Eq.(2.32). If $\Delta T = 1$, Appendix D.3 shows that this derivative may be calculated from Eq.(2.33) as

$$\frac{\partial}{\partial s}\left\langle T_0 \right\rangle = -\frac{r_1}{1 - r_1}\beta \left(\frac{1}{L} \sinh^{-1}\left(\frac{L}{s} \right) - \frac{1}{s^2} \right) . \tag{2.34}$$

2.4 Summary of Quasi-Geostrophic Equations

$$\frac{\partial \omega_z}{\partial t} + \left(u_s \frac{\partial}{\partial s} + \frac{u_\phi}{s}\frac{\partial}{\partial \phi} \right) \omega_z - (2 + \omega_z)\, \beta u_s = \left(B_s \left(\frac{\partial}{\partial s} - \beta \right) + \frac{B_\phi}{s}\frac{\partial}{\partial \phi} \right) j_z + E\, \nabla_H^2 \omega_z - Ra^* \frac{\partial \Theta}{\partial \phi} \, , \tag{2.35}$$

$$\frac{\partial}{\partial t}\left(\frac{\overline{u_\phi}}{s} \right) = \Gamma_{\mathrm{V}} + \Gamma_{\mathrm{R}} + \Gamma_{\mathrm{L}_1} + \Gamma_{\mathrm{L}_2} \, , \quad \text{where} \tag{2.36}$$

$$\Gamma_{\mathrm{V}} = \frac{E}{s^3 L}\frac{\partial}{\partial s}\left(s^3 L \frac{\partial}{\partial s}\left(\frac{\overline{u_\phi}}{s}\right)\right) \tag{2.37}$$

$$\Gamma_{\mathrm{R}} = -\overline{\frac{u_s}{s^2}\frac{\partial}{\partial s}\left(s u_\phi\right)} \tag{2.38}$$

$$\Gamma_{\mathrm{L}_1} = \frac{1}{s^3 L}\frac{\partial}{\partial s}\left(s^3 L B_{0s}\left(\frac{\overline{b_\phi}}{s}\right)\right) \tag{2.39}$$

$$\Gamma_{\mathrm{L}_2} = \overline{\frac{b_s}{s^2}\frac{\partial}{\partial s}\left(s b_\phi\right)}\,, \tag{2.40}$$

$$\frac{\partial}{\partial t}a = \left(u_s B_\phi - u_\phi B_s\right) + \frac{E}{P_m}\left(\nabla_H^2 a + \frac{2\beta a}{s}\right)\,, \tag{2.41}$$

$$\frac{\partial}{\partial t}\left(\frac{\overline{b_\phi}}{s}\right) = \frac{1}{sL}\frac{\partial}{\partial s}\left(L\left(\overline{u_\phi B_s} - \overline{u_s B_\phi}\right)\right) + \frac{1}{s^3}\frac{E}{P_m}\frac{\partial}{\partial s}\left(s^3\frac{\partial}{\partial s}\left(\frac{\overline{b_\phi}}{s}\right)\right)\,, \tag{2.42}$$

$$\frac{\partial \Theta}{\partial t} = -u_s\frac{\partial}{\partial s}\langle T_0\rangle - \mathbf{u}_H\cdot\left(\boldsymbol{\nabla}_H\Theta\right) + \frac{E}{P_r}\nabla_H^2\Theta\,, \quad \text{where} \tag{2.43}$$

$$\frac{\partial}{\partial s}\langle T_0\rangle = -\frac{r_1}{1-r_1}\beta\left(\frac{1}{L}\sinh^{-1}\left(\frac{L}{s}\right) - \frac{1}{s^2}\right) \tag{2.44}$$

For the remainder of this thesis, Eq.(2.35) will be called the "axial vorticity equation", Eq.(2.36) will be called the "zonal flow equation", Eq.(2.37) will be called the "viscous torque", Eq.(2.38) will be called the "Reynolds torque", Eq.(2.39) will be called the "axisymmetric Lorentz torque", Eq.(2.40) will be called the "Maxwell torque", Eq.(2.41) will be called the "induction equation", Eq.(2.42) will be called the "zonal induction equation", Eq.(2.43) will be called the "temperature equation", and Eq.(2.44) will be called the "background temperature gradient".

Chapter 3

Implementation

3.1 Solution Scheme

As discussed in Section 2.3.2, the nonaxisymmetric horizontal velocity and nonaxisymmetric horizontal magnetic perturbation fields are represented in terms of the potential functions ψ and a, respectively. The nonaxisymmetric vorticity Eq.(2.35) is therefore recast in terms of ψ – the nonaxisymmetric induction Eq.(2.41) is already written in terms of a.

The potential functions (ψ, a) and the temperature perturbation (Θ) are solved using a semi-spectral method. Second-order finite differences are used on a radial Chebyshev grid, while a Fourier decomposition is used in azimuth. To implement this, the full potential functions are written

$$\psi(t, s, \phi) = \sum_{m=1}^{M_{\max}} \psi_m(t, s) e^{im\phi}\,, \tag{3.1}$$

$$a(t, s, \phi) = \sum_{m=1}^{M_{\max}} a_m(t, s) e^{im\phi}\,, \tag{3.2}$$

and

$$\Theta(t,s,\phi) = \sum_{m=1}^{M_{\max}} \Theta_m(t,s) e^{im\phi}\,, \tag{3.3}$$

where i is the imaginary unit and the (ψ_m, a_m, Θ_m) are complex. Use of a Chebyshev grid ensures fine enough spacing to resolve boundary layers (proportional in thickness to $E^{1/2}$ for the flow field, $\left(\frac{E}{P_m}\right)^{1/2}$ for the magnetic field, and $\left(\frac{E}{P_r}\right)^{1/2}$ for the temperature perturbation), while maintaining reasonable computation times via coarser spacing away from the boundaries. The axisymmetric $\overline{u_\phi}$ and $\overline{b_\phi}$ are calculated on the same radial grid as the potential functions, but do not require the use of an azimuthal Fourier decomposition.

The inner boundary of the model is set to $s_1 = 0.35$, mimicking the thickness ratio of Earth's core, while the outer boundary is set to $s_2 = 0.98$ in order to maintain numerical stability ($\beta \to \infty$ as $s \to 1$).

3.2 Numerical Scheme

A typical differential equation of the function y and independent variable t may be written

$$\frac{\partial y}{\partial t} = f(t,y)\,, \tag{3.4}$$

where f is an arbitrary function. One way of integrating such an equation in t is to use one of a class of techniques known as linear multistep methods. For time indices i and j, and dummy index k, the value of y may be approximated as

$$y_{i+j} + \sum_{k=1}^{j} a_{j-k}\, y_{i+j-k} = \Delta t \sum_{k=0}^{j} b_{j-k}\, f\left(t_{i+j-k}, y_{i+j-k}\right)\,. \tag{3.5}$$

The choice of coefficients a and b determine the specific method being used. In particular, techniques with $b_j = 0$ are "explicit" since they do not require (notional) knowledge of the system's state at y_{i+j} to be used, while those with $b_j \neq 0$ are "implicit".

The (implicit) first-order Adams-Moulton scheme (sometimes called the Crank-Nicolson scheme) sets $j = 1$, $a_0 = -1$, and $b_0 = b_1 = 1/2$. Eq.(3.5) then becomes

$$\frac{y_{i+1} - y_i}{\Delta t} = \frac{1}{2}\left(f(t_{i+1}, y_{i+1}) + f(t_i, y_i)\right) . \tag{3.6}$$

The (explicit) second-order Adams-Bashforth scheme sets $j = 2$, $a_1 = -1$, $a_0 = 0$, $b_2 = 0$, $b_1 = 3/2$, and $b_0 = -1/2$. Relabeling $i \to i - 1$, Eq.(3.5) then becomes

$$\frac{y_{i+1} - y_i}{\Delta t} = \frac{3}{2} f(t_i, y_i) + \frac{1}{2} f(t_{i-1}, y_{i-1}) . \tag{3.7}$$

The QG differential equations may be written in the general form

$$\mathbf{A} \cdot \frac{\partial \mathbf{y}}{\partial t} = \mathbf{B} \cdot \mathbf{y} + \mathbf{N} . \tag{3.8}$$

Here, $\mathbf{y}$ is a column vector describing the state of the system, $\mathbf{A}$ and $\mathbf{B}$ are linear operators, and $\mathbf{N}$ is a column vector containing nonlinear terms. The right-hand side of Eq.(3.8) is therefore a linear combination of linear contributions ($\mathbf{A} \cdot \mathbf{y}$) and nonlinear contribution ($\mathbf{N}$). These contributions can be integrated separately, using the Adams-Moulton method for the linear portion and the Adams-Bashforth for the nonlinear:

$$\frac{1}{\Delta t}\mathbf{A} \cdot (\mathbf{y}_{i+1} - \mathbf{y}_i)|_{\text{linear}} = \frac{1}{2}\mathbf{B} \cdot \mathbf{y}_{i+1} + \frac{1}{2}\mathbf{B} \cdot \mathbf{y}_i , \tag{3.9}$$

$$\frac{1}{\Delta t}\mathbf{A} \cdot (\mathbf{y}_{i+1} - \mathbf{y}_i)|_{\text{nonlinear}} = \frac{3}{2}\mathbf{N}_i - \frac{1}{2}\mathbf{N}_{i-1} . \tag{3.10}$$

The two contributions can then be added to arrive at the final approximation for y_{i+1}:

$$\frac{1}{\Delta t}\mathbf{A}\cdot(\mathbf{y}_{i+1}-\mathbf{y}_i) = \frac{1}{\Delta t}\mathbf{A}\cdot\left((\mathbf{y}_{i+1}-\mathbf{y}_i)|_{\text{linear}} + (\mathbf{y}_{i+1}-\mathbf{y}_i)|_{\text{nonlinear}}\right) \tag{3.11}$$

$$= \frac{1}{2}\mathbf{B}\cdot\mathbf{y}_{i+1} + \frac{1}{2}\mathbf{B}\cdot\mathbf{y}_i + \frac{3}{2}\mathbf{N}_i - \frac{1}{2}\mathbf{N}_{i-1}\,. \tag{3.12}$$

$$\Rightarrow \left(\frac{1}{\Delta t}\mathbf{A} - \frac{1}{2}\mathbf{B}\right)\cdot\mathbf{y}_{i+1} = \left(\frac{1}{\Delta t}\mathbf{A} + \frac{1}{2}\mathbf{B}\right)\cdot\mathbf{y}_i + \frac{3}{2}\mathbf{N}_i - \frac{1}{2}\mathbf{N}_{i-1}\,. \tag{3.13}$$

So, the final expression to be solved is

$$\mathbf{C}\cdot\mathbf{y}_{i+1} = \mathbf{D}\cdot\mathbf{y}_i + \frac{3}{2}\mathbf{N}_i - \frac{1}{2}\mathbf{N}_{i-1}\,, \quad \text{where} \quad \mathbf{C} = \frac{1}{\Delta t}\mathbf{A} - \frac{1}{2}\mathbf{B}\,, \quad \mathbf{D} = \frac{2}{\Delta t}\mathbf{A} - \mathbf{C}\,. \tag{3.14}$$

This Adams-Bashforth-Moulton scheme has been shown (e.g. He and Sun, 2007) to be both stable and convergent in the context of the Navier-Stokes equations. In the case of the axial vorticity equation, $\mathbf{C}$ has five entries across the diagonal, so the resulting matrix equation is solved with LU decomposition (e.g. Press et al., 1992). For all other governing equations, $\mathbf{C}$ is tridiagonal, and the resulting matrix equations are solved using the tridiagonal algorithm from Press et al. (1992). In both cases, a fixed timestep Δt is used.

3.2.1 Velocity Equations

For a functional W which maps ψ to ω_z, the matrices for solving the axial vorticity equation (2.35) are

$$\mathbf{A}: \quad W(\psi): \psi \to \omega_z = -\nabla_H^2 \psi - \frac{1}{s}\frac{\partial}{\partial s}\left(s\beta\psi\right) \tag{3.15}$$

$$\mathbf{B}_m: \quad \left(E\nabla_H^2\left(W\right) + \frac{2\beta}{s} im\right)\psi_m \tag{3.16}$$

$$\mathbf{N}: \quad \left(B_s\left(\frac{\partial}{\partial s} - \beta\right) + \frac{B_\phi}{s}\frac{\partial}{\partial \phi}\right) j_z - \left(u_s\left(\frac{\partial}{\partial s} - \beta\right) + \frac{u_\phi}{s}\frac{\partial}{\partial \phi}\right)\omega_z - Ra^*\frac{\partial \Theta}{\partial \phi}\,. \tag{3.17}$$

However, as discussed in Section 4.1, the influence of the magnetic field will be ignored in the vorticity equation in the majority of models run. In such cases, the nonlinear vector becomes

$$\mathbf{N} = -\left(u_s\left(\frac{\partial}{\partial s} - \beta\right) + \frac{u_\phi}{s}\frac{\partial}{\partial \phi}\right)\omega_z - Ra^*\frac{\partial \Theta}{\partial \phi}\,. \tag{3.18}$$

With $\mathbf{I}$ denoting the identity matrix, the zonal flow equation (2.36) becomes

$$\mathbf{A}: \quad \mathbf{I} \tag{3.19}$$

$$\mathbf{B}: \quad \Gamma_{\mathrm{V}} = E\left(\frac{\partial^2}{\partial s^2} + \left(\frac{3}{s} + \beta\right)\frac{\partial}{\partial s}\right)\left(\overline{\frac{b_\phi}{s}}\right) \tag{3.20}$$

$$\mathbf{N}: \quad \Gamma_{\mathrm{R}} + \Gamma_{\mathrm{L}_1} + \Gamma_{\mathrm{L}_2} = -\frac{1}{s}\left(\overline{\frac{u_s}{s}\frac{\partial}{\partial s} s u_\phi}\right) + \frac{1}{s^3 L}\frac{\partial}{\partial s}\left(s^3 L B_{0s}\left(\overline{\frac{b_\phi}{s}}\right)\right) + \frac{1}{s}\left(\overline{\frac{b_s}{s}\frac{\partial}{\partial s} s b_\phi}\right)\,. \tag{3.21}$$

3.2.2 Magnetic Equations

For the induction equation (2.41),

$$\mathbf{A}: \quad \mathbf{I} \tag{3.22}$$

$$\mathbf{B}: \quad \frac{E}{P_m}\left(\nabla_H^2 + \frac{2\beta}{s}\right) a \tag{3.23}$$

$$\mathbf{N}: \quad u_s B_\phi - u_\phi B_s \,. \tag{3.24}$$

Note here that, since $B_{0\phi} = 0$, $B_\phi \to b_\phi$. For the zonal induction equation (2.42),

$$\mathbf{A}: \quad \mathbf{I} \tag{3.25}$$

$$\mathbf{B}: \quad \frac{1}{s^3}\frac{E}{P_m}\frac{\partial}{\partial s}\left(s^3\frac{\partial}{\partial s}\right)\left(\frac{\overline{b_\phi}}{s}\right) \tag{3.26}$$

$$\mathbf{N}: \quad B_{0s}\frac{\partial}{\partial s}\left(\frac{\overline{u_\phi}}{s}\right) + \frac{1}{sL}\frac{\partial}{\partial s}\left(L\left(\overline{u_\phi b_s} - \overline{u_s b_\phi}\right)\right) \,. \tag{3.27}$$

3.2.3 Temperature Equation

For the temperature equation (2.43),

$$\mathbf{A}: \quad \mathbf{I} \tag{3.28}$$

$$\mathbf{B}: \quad \frac{E}{P_r}\nabla_H^2\Theta \tag{3.29}$$

$$\mathbf{N}: \quad -u_s\frac{\partial}{\partial s}\langle T_0\rangle - \mathbf{u}_H\cdot(\boldsymbol{\nabla}_H\Theta) \,. \tag{3.30}$$

3.3 Axisymmetric Nonlinear Averages

Normally, calculation of the nonlinear products contained within the **N** vectors must be performed in real space. For example, to calculate the $u_s B_\phi$ term in Eq.(3.24), both the u_ϕ and b_ϕ fields are transformed from Fourier space to real space, multiplied with one another,

and the result transformed back to Fourier space for time integration. Because the forward and inverse Fourier transforms are computationally expensive, and must be performed at each timestep, techniques have been developed to avoid them where possible.

One such technique is used when the azimuthal average of a nonlinear product is needed: Appendix A.5 demonstrates that the entire operation may be performed in Fourier space, avoiding the need to transform to and from real space. Appendix E uses the final result of Appendix A.5, Eq.(A.79), to calculate the Γ_{R} and Γ_{L_2} terms in Eq.(3.21) and the $\overline{u_\phi b_s} - \overline{u_s b_\phi}$ term of Eq.(3.27) as

$$\begin{aligned} \Gamma_{\mathrm{R}} &= \frac{2}{s^2} \sum_{m=1}^{\infty} m \left(\Re\left(\psi_m\right) \Im\left(\alpha_m\right) - \Im\left(\psi_m\right) \Re\left(\alpha_m\right) \right) \\ \text{where} \quad \alpha_m &= \left(\frac{\partial^2}{\partial s^2} + \left(\beta + \frac{1}{s} \right) \frac{\partial}{\partial s} + \left(\frac{\beta}{s} + \frac{\partial \beta}{\partial s} \right) \right) \psi_m \,, \end{aligned} \tag{3.31}$$

$$\begin{aligned} \Gamma_{\mathrm{L}_2} &= \frac{2}{s^2} \sum_{m=1}^{\infty} m \left(\Im\left(a_m\right) \Re\left(\gamma_m\right) - \Re\left(a_m\right) \Im\left(\gamma_m\right) \right) \\ \text{where} \quad \gamma_m &= \left(\frac{\partial^2}{\partial s^2} + \left(\beta + \frac{1}{s} \right) \frac{\partial}{\partial s} + \left(\frac{\beta}{s} + \frac{\partial \beta}{\partial s} \right) \right) a_m \,, \end{aligned} \tag{3.32}$$

and

$$\frac{1}{sL} \frac{\partial}{\partial s} \left(L \left(\overline{u_\phi b_s} - \overline{u_s b_\phi} \right) \right) = \frac{2}{s^2} \sum_{n=1}^{3} \sum_{m=1}^{\infty} m \left[\Im\left(\alpha_n^m\right) \Re\left(\gamma_n^m\right) - \Re\left(\alpha_n^m\right) \Im\left(\gamma_n^m\right) \right] , \tag{3.33}$$

with

n	α_n^m	γ_n^m
1	a^m	$\left(\frac{\partial^2}{\partial s^2} + \left(\beta - \frac{1}{s}\right)\frac{\partial}{\partial s} + \left(\frac{\partial \beta}{\partial s} - \frac{\beta}{s}\right)\right)\psi^m$
2	$-\psi^m$	$\left(\frac{\partial^2}{\partial s^2} - \frac{1}{s}\frac{\partial}{\partial s}\right)a^m$
3	$2\frac{\partial}{\partial s}a^m$	$\left(\frac{\partial}{\partial s} + \beta\right)\psi^m$

3.4 Parameters

3.4.1 Maintaining Model Validity

In the absence of magnetic forces, the QG model's assumption of rigidity remains valid provided that Coriolis forces dominate inertial forces. The relative strength of each is captured by the Rossby number R_o. For a velocity scale $\mathcal{U}$ and a length scale $\mathcal{L}$,

$$R_o = \frac{|\text{inertial forces}|}{|\text{Coriolis forces}|} = \frac{\mathcal{U}}{\Omega \mathcal{L}} \ll 1\,. \tag{3.34}$$

As shown in Table 2.2, the typical velocity scale in the core is $\mathcal{U} \approx 3 \times 10^{-4}$ m s^{-1}, the typical length scale is $\mathcal{L} \approx 3 \times 10^6$ m, and the rotation rate is $\Omega \approx 7 \times 10^{-5}$ s^{-1}, resulting in a Rossby number of about 10^{-6}. Similarly, Rossby numbers in our model must be kept much less than 1. Because the nondimensionalization method we use implies that model velocities $\mathbf{u}$ are equivalent to local Rossby numbers, this restriction amounts to ensuring that $|\mathbf{u}| \ll 1$.

While magnetic forces are in principle capable of breaking the geostrophic assumption, in practice flows remain rigid so long as the timescale of inertial waves remains much less than the timescales of magnetic waves (Jault, 2008; Jault and Finlay, 2015). The ratio between the two timescales is captured by the Lehnert (or magnetic Rossby) number λ, written in terms of the Alfvén velocity as

$$\lambda = \frac{u_A}{\Omega \mathcal{L}} \ll 1\,. \tag{3.35}$$

Using the values in Table 2.1, Eq.(1.8) shows u_A to be

$$u_A = \frac{|\mathbf{B}|}{\sqrt{\rho_0 \mu_0}} \approx 3 \times 10^{-2}\,\mathrm{m\,s^{-1}}\,, \tag{3.36}$$

implying a Lehnert number of about 5×10^{-4}. Clearly, rotational forces dominate in the outer core even in the presence of the magnetic field. Much like the model's nondimensional velocity field being equivalent to local Rossby number, the model's magnetic perturbation field $\mathbf{b}$ is nondimensionalized to be equivalent to the local Lehnert number. Thus, to maintain rigidity (and therefore the validity of the QG approximation), the model's control parameters must be chosen such that $\mathbf{b} \ll 1$ at all times.

Finally, the modified Rayleigh number Ra^* represents the strength ratio of buoyancy and rotational forces. To maintain rigidity, the Coriolis force must dominate. Indeed, Table 2.3 shows that Ra^* in the outer core is $\ll 1$. Similarly, Ra^* in the model must be kept $\ll 1$.

3.4.2 Control Parameters

The behaviour of the QG model constructed for this thesis is dictated by five control parameters: the Ekman number E, the modified Rayleigh number Ra^*, the background radial magnetic field strength B_{0s}, the Prandtl number P_r, and the magnetic Prandtl number P_m. Section 3.4.4 will outline the procedure for selecting control parameters which both respect the QG assumptions (discussed in Section 3.4.1) and correspond to the region of (diagnostic) parameter space in which the model behaves in a somewhat Earth-like fashion (to be discussed in Section 3.4.3). First, however, it is useful to discuss how each control parameter affects the model's behaviour.

The Ekman number represents the ratio in strength between viscous and Coriolis forces. It

is linked to the thickness of the viscous boundary layer, proportional to $E^{1/2}$, and to the length scale of viscously-controlled convective eddies, proportional to $E^{1/3}$. The extremely small value of $E \approx 10^{-15}$ in the outer core implies that important convective dynamics are likely to occur at even extremely small length scales, and extremely rapidly.

The Prandtl number is the ratio between the timescales of thermal and viscous diffusion. The smaller P_r, the more easily heat can be conducted through a fluid and the less likely convection is to occur for a given amount of thermal stress. Because the value of P_r in the outer core is close to 1 (see Table 2.3), we simply set it to that value when tuning our model.

As discussed in the previous section, the modified Rayleigh number measures the strength ratio between buoyant and Coriolis forces through a combination of the traditional Rayleigh number (a measure of convective vigor), the Ekman number, and the Prandtl number. There is a critical value of Ra^* above which the primary mechanism to transport heat in the system switches from conduction to convection. Higher values of supercritical Ra^* correspond to more vigorous convection: heat is transported more rapidly, and root-mean-square (RMS) velocities increase.

The magnetic Prandtl number is the ratio of magnetic to viscous diffusion timescales. It controls the rate of magnetic diffusion: smaller values of P_m correspond to enhanced magnetic diffusion. Thus, the lower the value of P_m, the less tightly the magnetic field is bound to the flow and the smaller the amount of magnetic induction occurs. Put another way, smaller values of P_m result in weaker and larger magnetic structures.

Our nondimensionalization of the magnetic field means $u_A = |\mathbf{B}| = |\mathbf{B}_0 + \mathbf{b}|$. In practice, the strength of $\mathbf{b}$ is proportional to the strength of B_{0s}, implying $u_A \propto |B_{0s}|$. Thus, $|B_{0s}|$ controls both the speed of free Alfvén waves and, through its influence on the magnitude of

b, the strength of magnetic forces.

In summary, larger values of Ra^* correspond to larger RMS velocities, while larger magnitudes of B_{0s} correspond to larger RMS magnetic perturbation fields. Meanwhile, smaller values of E correspond to smaller convective length scales and weaker viscous diffusion, while smaller values of P_m correspond to larger magnetic length scales and enhanced magnetic diffusion.

3.4.3 Earth-Like Regime

While the QG model constructed for this thesis is highly idealized and has been optimized for investigating a very specific problem, the control parameters we choose should still reflect the conditions of Earth's core if we hope for our results to be meaningful.

Section 1.5 shows that convective velocities (u_C) must be smaller than the Alfvén velocity (u_A) if the zonal accelerations are to be forced by the underlying convective structure. This relationship is captured by the Alfvén number, $\mathcal{A} = \frac{u_C}{u_A}$. As shown in Section 1.5, $\mathcal{A}$ in the core is thought to be about 0.01. Since Ra^* controls our model's convective velocities and $|B_{0s}|$ controls its Alfvén velocity, Ra^* and B_{0s} must then be picked such that $\mathcal{A} \ll 1$ if we expect to reproduce the force regime of the outer core.

While this constrains the modified Rayleigh number and the background magnetic field strength for any given Ekman number, it does not provide any guidance on choosing a magnetic Prandtl number. However, if the Maxwell torque of Eq.(2.40) dominates the torque balance responsible for zonal accelerations, as we hypothesize, it must also dominate the Reynolds torque of Eq.(2.38). Because the value of $|\mathbf{b}|$ is controlled by the values of $|B_{0s}|$ and P_m, and because $|B_{0s}|$ is already constrained by the Alfvén number, this suggests a way

to constrain P_m.

Maxwell torques are proportional to $|\mathbf{b}|^2$; Reynolds torques, to $|\mathbf{u}|^2$. Using the root-mean-square values $b_{\text{RMS}} = \left|\mathbf{b} - \overline{b_\phi}\mathbf{e}_\phi\right|$ and $u_{\text{RMS}} = |\mathbf{u} - \overline{u_\phi}\mathbf{e}_\phi|$ as proxies for the field strengths, the requirement that Maxwell torques be greater than Reynolds torques implies $b_{\text{RMS}} \gg u_{\text{RMS}}$. The induction equation (2.41) provides an avenue to find how the ratio of b_{RMS} and u_{RMS} scales. When the model has achieved statistical equilibrium, the magnitude of its source and diffusion terms must be in balance:

$$|\boldsymbol{\nabla} \times ((\mathbf{B}_0 + \mathbf{b}) \times \mathbf{u})| = \left|\frac{E}{P_m}\boldsymbol{\nabla}_H^2 \mathbf{b}\right| . \tag{3.37}$$

Using local flow length scale ℓ_c and local magnetic field length scale ℓ_b, and assuming $|\mathbf{B}| \approx B_{0s}$ (for a uniform B_{0s}), this scales as

$$\frac{|\mathbf{B}|\,|\mathbf{u}|}{\ell_c} = \frac{E}{P_m}\frac{|\mathbf{b}|}{\ell_b^2} \quad \Rightarrow \frac{B_{0s} u_{\text{RMS}}}{\ell_c} = \frac{E}{P_m}\frac{b_{\text{RMS}}}{\ell_b^2} . \tag{3.38}$$

Rearranging, and recalling that we need $b_{\text{RMS}} \gg u_{\text{RMS}}$,

$$\frac{b_{\text{RMS}}}{u_{\text{RMS}}} = \frac{B_{0s}}{\ell_c}\frac{P_m \ell_b^2}{E} \gg 1 . \tag{3.39}$$

While local magnetic length scales are typically longer than local viscous length scales, the difference in the model is generally somewhat less than an order of magnitude. Eq.(3.39) therefore places a constraint on which values of P_m may be chosen against a given $\frac{B_{0s}}{E}$ ratio if $b_{\text{RMS}} \gg u_{\text{RMS}}$ is to be maintained. In practice, numerical constraints limit both the minimum size of E and the maximum size of B_{0s}, while the latter value is further constrained by the requirement that, according to the QG assumption, $u_A \approx B_{0s} < 1$ (that is, magnetic waves travel more slowly than inertial waves). Thus, while Table 2.3 shows that $P_m \approx 10^{-6}$ in the outer core, a model with $B_{0s} = 0.1$ and $E = 10^{-6}$ (so that $\frac{B_{0s}}{E} = 10^5$) would require $P_m \approx 10^{-2}$ to ensure $b_{\text{RMS}} \gg u_{\text{RMS}}$.

As a side note, it may be seen that the structure of Eq.(3.39) is not a mere mathematical curiosity. By defining a local magnetic diffusion timescale, $\tau_{d_b} = P_m E^{-1} \ell_b^2$, and a local Alfvén timescale, $\tau_a = \ell_c B_{0s}^{-1}$ (since $B_{0s} \approx u_A$), Eq.(3.39) may be expressed in terms of the ratio of the two timescales. This ratio is the Lundquist number, Lu:

$$\mathrm{Lu} = \frac{\tau_{d_b}}{\tau_a} = \frac{B_{0s}}{\ell_c} \frac{P_m \ell_b^2}{E} \gg 1 \,. \tag{3.40}$$

Requiring a Lundquist number much greater than one implies information may be transmitted via magnetic waves with minimal distortion by magnetic diffusion. Clearly this must be the case if decadal-timescale, magnetically-forced accelerations are to occur in the core.

In summary, to ensure convective and magnetic conditions comparable to those found in the outer core, (1) Ra^* (corresponding to convective velocities) and B_{0s} (corresponding to the Alfvén velocity) must be chosen such that $\mathcal{A} \ll 1$, and (2) P_m must be chosen such that, for a given B_{0s} and E, a Lundquist number $\mathrm{Lu} \gg 1$ is maintained.

3.4.4 Selection Procedure

The first parameter to be chosen is the Ekman number. Since the Ekman number sets the minimum length scale of the model, its value also determines the number of radial grid points and the number of azimuthal Fourier modes. While lower Ekman numbers are generally desirable, they are limited by the computational resources available.

Rational values for the magnetic control parameters depend largely upon the typical flow velocities in any given model. However, the flow velocities themselves depend upon the control parameters. Fortunately, the parameter they depend upon *most* is Ra^*. Therefore, lacking prior knowledge of Ra^*'s critical value, various values are tried and the model is run without

magnetic feedback on the velocity equations[1]. Acceptable values are much less than 1, in keeping with the QG assumptions, and produce fully turbulent convection with velocities much less than 1, also in keeping with the QG assumptions.

With length scales set by the Ekman number and velocity scales set (for the nonmagnetic case) by the modified Rayleigh number, the magnetic control parameters may then be chosen. First, the Alfvén number is used as a guide for selecting the strength of the magnetic background field. While

$$\mathcal{A} = \frac{u_C}{u_A} \approx \frac{u_C}{B_{0s}} \tag{3.41}$$

is about 0.01 in Earth's core, in the models we generally use a less numerically aggressive target of $\mathcal{A} \approx 0.1$. In other words, we typically set B_{0s} to about $0.1\, u_C$.

Finally, P_m is chosen so as to balance the conflicting demands of a strong magnetic diffusivity (corresponding to low P_m), and a high Lundquist number (corresponding to high P_m). While in the core $P_m \approx 10^{-6}$, we find that in our models values of $10^{-1} - 10^{-3}$ produce better results. As will be seen in Chapter 4, values of B_{0s} and/or P_m which are too high result in flows which are locked to the background magnetic field, unable to form the large-scale, time-dependent eddies necessary to distort the magnetic field on convective timescales. Selecting the proper values of each is the crux of this project.

While not strictly a control parameter, the choice of timestep is critical for model performance. Too high, and the model will be numerically unstable. Too low, and computation times can become unreasonable. In our model, lower Ekman numbers, higher velocities, and higher magnetic background field strengths tend to require smaller timesteps, though

[1]Since the magnetic field is not needed for calculation of the flow field in these experiments, the induction equations are also not calculated, significantly speeding the process.

lower magnetic Prandtl numbers can somewhat ease the effects of a strong B_{0s}. Because the model's timestep is static and set at runtime, choosing it is largely a matter of trial and error. When a timestep is found that results in a somewhat stable model, it is generally halved to ensure stability. The timestep, number of radial grid points, and number of azimuthal Fourier modes are collectively referred to as the "grid parameters".

Chapter 4

Results

4.1 The Non-Axisymmetric Lorentz Torque

In a fully dynamical, Earth-like system, both the flow and magnetic fields tend to align themselves so as to limit induction by shear (e.g. Moffatt, 1978; Schaeffer et al., 2017). However, because the background magnetic field we impose on our model is constant in time, such a dynamic reorganization of the magnetic field is not possible . This means the non-axisymmetric Lorentz torque in the axial vorticity equation strongly opposes any shearing of the magnetic field, causing the flow to become "locked" onto the radial magnetic field lines of the imposed magnetic background field. Such a configuration was common in many of the early experiments we ran, with a snapshot of the vorticity and current fields from a typical experiment (#11) shown in Figure 4.1.

The long, thin, stationary convection cells which form in such a configuration span nearly the entire radial domain of the model, and do not much resemble the large-scale flows found in the outer core. With time-varying eddy structures unable to form in the flow field, similar structures are not induced in the magnetic perturbation field. As a result, free Alfvén waves, excited as the zonal flow adjusts to small perturbations in the magnetic field, are the

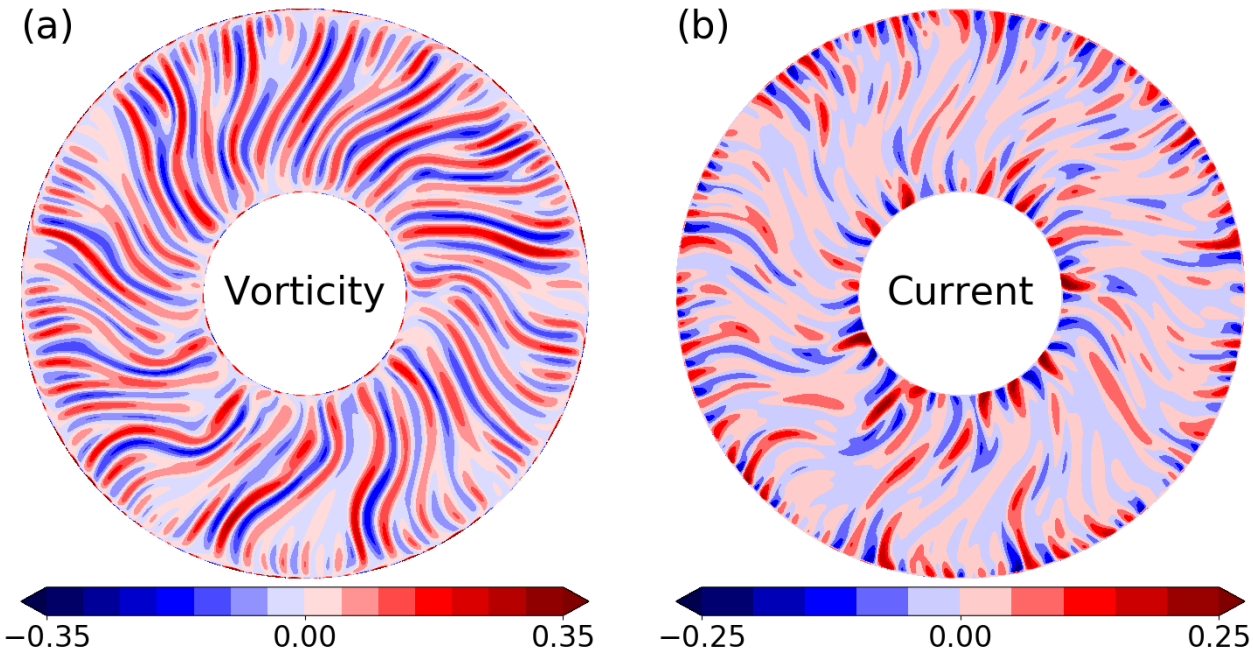

Figure 4.1: Snapshots in time of (a) the nonaxisymmetric vorticity ω_z and (b) the nonaxisymmetric axial current j_z for Experiment #11, which includes the non-axisymmetric Lorentz torque in the non-axisymmetric vorticity equation. The view is downwards from the north pole.

dominant magnetically-forced zonal accelerations which occur. The regular zonal accelerations shown in Figure 4.2 are magnetically-controlled in this way, with the period of the accelerations matching very closely with the fundamental Alfvén timescale[1]

Recognizing that the flow field was being unduly constrained by the magnetic field, some attempt was made to allow the former to "slip" through the latter by lowering P_m. In theory, this would enhance the rate of magnetic diffusion, allowing larger velocity shears to develop before being braked by magnetic forces. In practice, values of P_m which allowed sufficient velocity shears enhanced magnetic diffusion so much that the scale of magnetic perturbations became comparable to, or smaller than, the scale of the velocity field. In other words, the Lundquist number dropped below 1, and magnetically-dominated zonal accelerations

[1]In fact, the period of the accelerations is slightly greater than τ_A. This is not surprising given that the speed of a free Alfvén wave depends on the local magnetic field strength, $|\mathbf{B}| = |\mathbf{B}_{0s} + \mathbf{b}|$. Since we define u_A and τ_A globally in terms of B_{0s}, however, the true Alfvén velocity and timescale will generally be larger and smaller than u_A and τ_A, respectively.

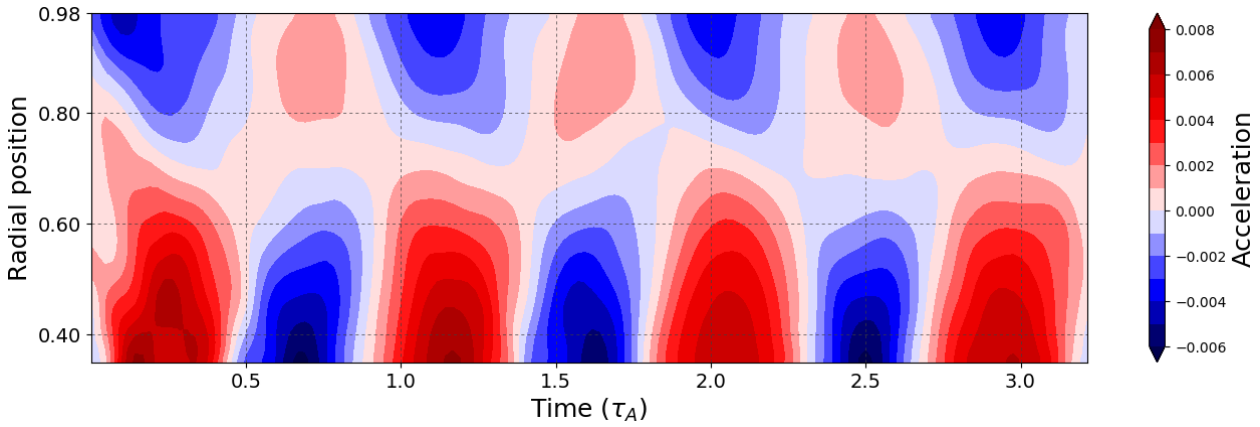

Figure 4.2: The zonal angular acceleration from Experiment #11, which includes the non-axisymmetric Lorentz torque in the non-axisymmetric vorticity equation. The Alfvén timescale τ_A is that of the fundamental Alfvén wave mode, $\tau_A = 2(s_2 - s_1)/u_A$.

became impossible. Attempts to magnify what perturbations *were* induced by increasing B_{0s} were unsuccessful.

Because we wish to demonstrate the mechanism by which large-scale flows can interact with the magnetic field to generate slow zonal accelerations, our models must exhibit some degree of large-scale, time-dependent convection – structures which are consistent in form with those found in the outer core, if not in their governing force balances. One way to force our model to form such structures is to exclude the non-axisymmetric Lorentz torque from the axial vorticity equation. In other words, the first term on the right-hand side of Eq.(2.35) is set to zero, reducing the equation to

$$\frac{\partial \omega_z}{\partial t} + \left(u_s \frac{\partial}{\partial s} + \frac{u_\phi}{s} \frac{\partial}{\partial \phi} \right) \omega_z - (2 + \omega_z)\, \beta u_s = E\, \nabla_H^2 \omega_z - Ra^* \frac{\partial \Theta}{\partial \phi}\,. \tag{4.1}$$

In effect, convective eddies are allowed to distort the magnetic field, but the magnetic field is not allowed to feed back on the convective eddies. However, because the primary objective of this thesis is to show that the sum of small-scale magnetic torques can be the dominant driver of large-scale zonal accelerations, the axisymmetric Lorentz torque $\Gamma_{\rm L} = \Gamma_{\rm L_1} + \Gamma_{\rm L_2}$ is retained in the zonal flow equation.

4.2 Overview of Results

4.2.1 Model Initialization

To initialize a model from scratch, the vectors for ψ, a, and the nonlinear terms used for timestepping (see Section 3.2) were set to zero. The entries in the ψ vector corresponding to Fourier modes 20 to 25 were then perturbed according to $\psi(i,m) = 10^{-7} s_i \sin(\pi s_i)\, e^{-400(s_i-0.65)^2}$, where s_i is the radial position of the i-th radial grid point and m is the Fourier mode.

To reduce spinup times for subsequent models, however, a basic model was first run from scratch until it reached statistical equilibrium (see Section 4.3). The final output values from this basic model were then used as the synthetic initial state for the daughter models catalogued in Table 4.1. The basic model had the following control and grid parameters: $E = 5.0 \times 10^{-6}$, $Ra^* = 0.0125$, $B_{0s} = 0.001$, $P_m = 1.0$, 601 radial grid points, 767 azimuthal Fourier modes[2], timestep $\Delta t = 0.001$, and the non-axisymmetric Lorentz torque included in the non-axisymmetric vorticity equation.

4.2.2 Exploration of Parameter Space

As illustrated by the "family tree" in Figure 4.3, many of the experiments shown in Table 4.1 are daughters of other experiments, rather than the basic initial model. In either case, one or more of the control or grid parameters are generally changed in the from one model to the next[3]. As our understanding of the problem grew, more intelligent parameter choices

[2]This seemingly unusual choice is made because our model uses the FFTW (Fastest Fourier Transform in the West) library to perform forward and inverse Fourier transforms. FFTW is most efficient with $2^n 3^m - 1$ nonzero Fourier modes, where n and m are non-negative integers (Frigo and Johnson, 2005); $767 = 2^8 3^1 - 1$.

[3]In cases where the previous model had crashed, one of the output files it generated *before* it crashed was used as the initial state of the subsequent model, with the latter usually having higher resolution in space

Experiment number	Restarted from	Ra^*,	B_{0s}	P_m	NS	Mmax	Δt, $\times 10^{-4}$	NALT	Crash	u_{RMS}, $\times 10^{-3}$	b_{RMS}, $\times 10^{-3}$	RMS $\left(\frac{\overline{u_\phi}}{s}\right)$, $\times 10^{-3}$	RMS $\left(\frac{\partial}{\partial t}\left(\frac{\overline{u_\phi}}{s}\right)\right)$, $\times 10^{-4}$	$\mathcal{A}$	Lu
01	-	0.0250	0.001	1.00	600	767	10.0	Y	Y	27.008	32.503	4.91	1.85	27.01	1.20
02	-	0.0250	0.001	1.00	600	767	10.0	N	Y	24.806	77.059	1.38	0.50	24.81	3.11
03	-	0.0125	0.003	1.00	600	767	10.0	Y	N	1.310	1.446	0.37	1.91	0.44	1.10
04	-	0.0125	0.003	1.00	600	767	10.0	N	Y	20.427	72.363	1.54	3.25	6.81	3.54
05	-	0.0125	0.001	0.50	600	767	10.0	Y	N	2.018	1.095	0.71	0.57	2.02	0.54
06	-	0.0125	0.001	1.00	600	767	10.0	N	N	2.277	3.357	9.67	1.53	2.28	1.47
07	-	0.0250	0.001	1.00	800	767	10.0	Y	Y	-	-	-	-	-	-
08	-	0.0250	0.001	1.00	900	767	5.0	N	Y	-	-	-	-	-	-
09	3	0.0125	0.003	1.00	600	767	10.0	Y	N	1.148	2.012	0.44	0.09	0.38	1.75
10	5	0.0125	0.001	0.50	600	767	10.0	Y	N	1.751	0.985	0.76	0.05	1.75	0.56
11	10	0.0125	0.003	0.50	600	767	10.0	Y	N	1.269	1.030	0.88	0.40	0.42	0.81
12	10	0.0125	0.003	0.50	600	767	10.0	N	N	2.631	7.165	2.19	0.61	0.88	2.72
13	10	0.0175	0.003	0.50	600	767	10.0	Y	N	1.949	1.410	0.93	0.27	0.65	0.72
14	10	0.0175	0.003	0.50	600	767	10.0	N	N	4.596	11.241	2.54	1.09	1.53	2.45
15	6	0.0175	0.001	1.00	600	767	10.0	N	N	3.601	5.862	0.56	0.46	3.60	1.63
16	-	0.0175	0.001	1.00	600	767	10.0	N	N	4.048	6.278	4.76	1.09	4.05	1.55
17	-	0.0175	0.001	1.00	900	767	5.0	N	N	0.086	0.079	11.05	1.07	0.09	0.93
18	14	0.0175	0.003	0.50	600	767	10.0	N	N	4.421	11.746	3.06	1.33	1.47	2.66
19	16	0.0175	0.001	1.00	600	767	10.0	N	N	3.808	5.325	0.93	0.52	3.81	1.40
20	17	0.0175	0.001	1.00	900	767	5.0	N	N	6.262	8.988	4.33	1.88	6.26	1.44
21	14	0.0175	0.005	0.50	600	767	10.0	N	N	4.552	22.257	3.28	1.79	0.91	4.89
22	16	0.0175	0.003	1.00	600	767	10.0	N	N	6.145	27.832	2.50	3.02	2.05	4.53
23	18	0.0175	0.003	0.50	600	767	10.0	N	N	4.718	13.139	2.58	1.35	1.57	2.79
24	19	0.0175	0.001	1.00	600	767	10.0	N	N	3.474	5.180	0.63	0.43	3.47	1.49
25	20	0.0175	0.001	1.00	900	767	5.0	N	N	3.479	5.052	0.64	0.70	3.48	1.45
26	21	0.0175	0.005	0.50	600	767	10.0	N	Y	17.317	45.426	2.98	2.34	3.46	2.62
27	16	0.0175	0.003	1.00	750	767	5.0	N	Y	13.451	47.250	3.13	6.13	4.48	3.51
28	16	0.0175	0.003	1.00	900	767	5.0	N	Y	14.482	83.257	3.16	7.87	4.83	5.75
29	16	0.0175	0.003	1.00	1200	1023	2.5	N	Y	20.389	117.630	3.39	13.58	6.80	5.77
30	28	0.0175	0.003	1.00	1200	1023	5.0	N	Y	-	-	-	-	-	-
31	28	0.0175	0.003	1.00	1200	1023	2.5	N	Y	-	-	-	-	-	-
32	16	0.0175	-	-	1200	1023	5.0	-	Y	0.157	-	11.55	0.08	-	-
33	16	0.0125	0.003	1.00	1200	1023	2.5	N	Y	6.605	23.033	3.31	7.40	2.20	3.49
34	16	0.0175	0.003	0.50	1200	1023	2.5	N	Y	29.738	50.389	10.89	14.36	9.91	1.69
35	16	0.0125	0.006	0.50	1200	1023	2.5	N	Y	14.753	48.531	-	-	2.46	3.29
36	25	0.0175	0.005	0.10	900	767	5.0	N	N	3.897	8.479	4.30	1.02	0.78	2.18
37	25	0.0175	0.010	0.10	900	767	5.0	N	N	4.820	17.327	4.66	2.82	0.48	3.59
38	37	0.0175	0.030	0.10	900	767	5.0	N	N	4.788	51.749	4.30	3.67	0.16	10.81
39	37	0.0225	0.010	0.10	900	767	5.0	N	N	7.677	23.056	4.48	5.62	0.77	3.00
40	37	0.0125	0.010	0.10	900	767	5.0	N	N	3.055	11.545	3.29	1.39	0.31	3.78
41	37	0.0125	0.030	0.10	900	767	5.0	N	N	2.569	31.651	3.26	1.73	0.09	12.32
42	38	0.0175	0.050	0.10	900	767	5.0	N	N	4.375	72.886	4.30	2.82	0.09	16.66
43	38	0.0175	0.075	0.10	900	767	5.0	N	N	4.423	144.878	4.23	2.26	0.06	32.75
44	38	0.0175	0.100	0.03	900	767	5.0	N	N	4.754	88.170	3.91	1.97	0.05	18.54
45	41	0.0125	0.060	0.10	900	767	5.0	N	N	2.555	65.266	3.56	0.85	0.04	25.55
46	41	0.0125	0.075	0.10	900	767	5.0	N	N	2.621	71.513	3.71	1.01	0.03	27.29
47	41	0.0125	0.100	0.03	900	767	5.0	N	N	2.819	41.555	2.72	1.19	0.03	14.74
48	43	0.0175	0.150	0.10	900	767	5.0	N	N	4.696	267.639	4.50	2.16	0.03	56.99
49	46	0.0125	0.150	0.10	900	767	5.0	N	N	2.375	149.353	3.39	1.07	0.02	62.87
50	44	0.0175	0.300	0.03	900	767	5.0	N	N	4.150	223.732	3.89	1.90	0.01	53.91
51	47	0.0125	0.300	0.03	900	767	5.0	N	N	2.594	135.196	2.55	1.31	0.01	52.11
52	46	0.0125	0.150	0.10	900	767	5.0	N	N	2.445	144.591	3.41	5.50	0.02	59.14
53	44	0.0175	0.300	0.03	900	767	5.0	N	N	4.103	221.960	3.89	15.42	0.01	54.10
54	46	0.0125	0.150	0.10	900	767	5.0	N	N	2.649	142.493	3.51	5.51	0.02	53.80
55	52	0.0125	0.300	0.05	900	767	2.5	N	N	2.518	180.967	2.86	32.06	0.01	71.88

Table 4.1: Summary of experiments. All models were run with Ekman number $E = 5.0 \times 10^{-6}$ and Prandtl number $P_r = 1$. Models restarted from '-' use the synthetic initial state specified in Section 4.2.1. 'NS' is the number of radial grid points, 'Mmax' is the maximum azimuthal Fourier mode, Δt is the timestep, 'NALT' is whether or not the non-axisymmetric Lorentz torque was included in the axial vorticity equation, and 'Crash' is whether or not the model crashed. u_{RMS} is the root-mean-square value of the non-axisymmetric velocity field at the final output of the model (or the final output before the model crashed), and b_{RMS} is the same but for the magnetic perturbation field. RMS$(\cdot)$ is the root-mean-square value of $(\cdot)$, calculated across all model outputs. The Alfvén and Lundquist numbers are defined in Eq.(4.2)

could be made (see Section 3.4.4).

All models used an Ekman number $E = 5.0 \times 10^{-6}$ and Prandtl number $P_r = 1.0$. The modified Rayleigh number was varied by only a factor of two across all experiments, as values of $0.0125 - 0.0250$ were clearly above the critical value while also producing velocities $\ll 1$ as required by the QG approximation.

Most modifications of the model's behaviour were therefore made by adjusting the background magnetic field strength B_{0s}, the magnetic Prandtl number P_m, and whether or not the non-axisymmetric Lorentz torque was included in the axial vorticity equation (that is, whether Eq.(2.35) or Eq.(4.1) was used). Most of the models which excluded the non-axisymmetric Lorentz torque exhibited slow zonal accelerations (compared to the Alfvén timescale) controlled to a greater (higher Lundquist number) or lesser (lower Lundquist number) extent by the zonal Lorentz torque.

For ease of discussion, I have focused the remainder of this thesis on one model which produces particularly good, though not atypical, results: Experiment #52 in Table 4.1. With control parameters of $E = 5.0 \times 10^{-6}$, $P_r = 1$, $Ra^* = 0.0125$, $B_{0s} = 0.15$, and $P_m = 0.1$, it uses 901 radial grid points, 768 azimuthal Fourier modes, and a timestep of 5×10^{-4}. The relatively high number of radial points results in points near the boundary being separated by about 2×10^{-6}. With the thickness of the viscous boundary layer being proportional to $E^{1/2} \approx 0.002$, such a small grid size gives us confidence that the model's spatial resolution near the boundaries is adequate. At the same time, with points in the centre of the model domain separated by about 1×10^{-3}, reasonable computational efficiency is maintained.

and/or time in an attempt to stabilize the instability.

Figure 4.3: Hierarchy of experiments. The statistical equilibrium of the synthetic initial state described in Section 4.2.1 is represented by the white box. A red box indicates that a model crashed, while a green box indicates that it ran to completion. Connecting lines show which previous model a particular model was restarted from. Dotted lines indicate that some set of parameters was changed compared to the previous model, while solid lines indicate that a model is a strict continuation of its parent. Notes in each box denote what was changed from the parent experiment. See Table 4.1 for a summary of model parameters and statistics.

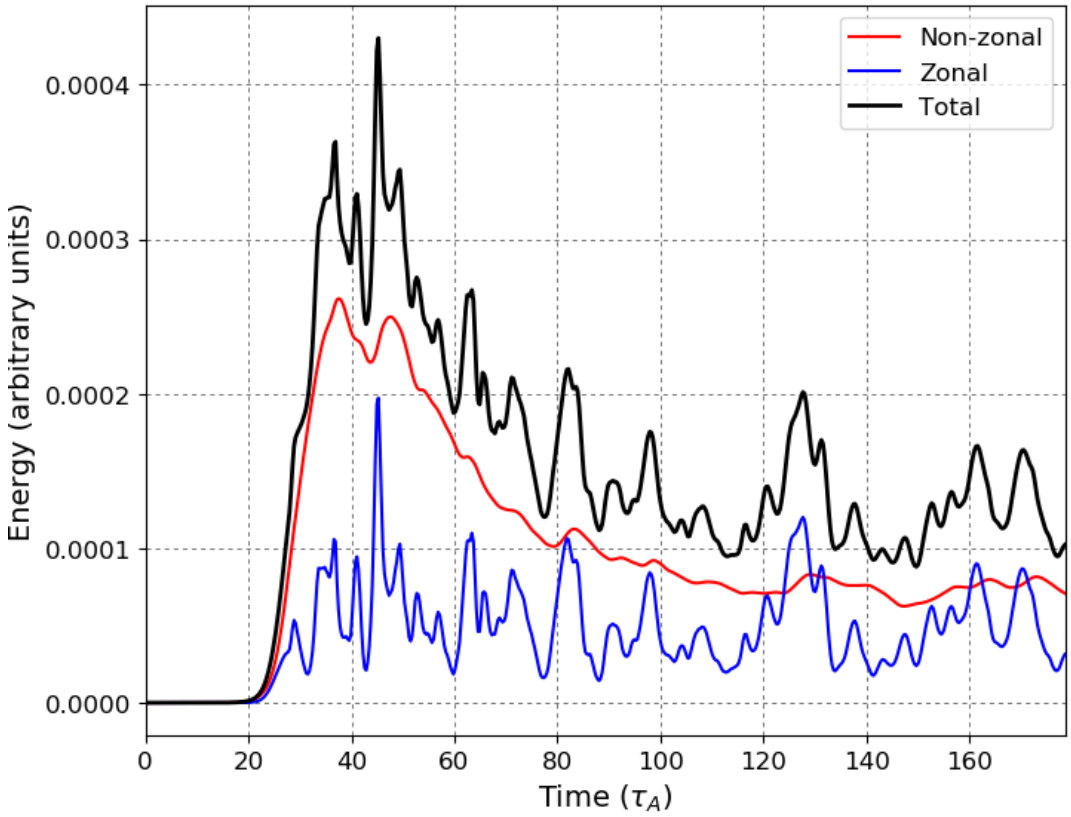

Figure 4.4: Evolution of the mechanical energy in a version of Experiment #52 which was initialized from scratch (that is, was not restarted from a previous experiment; see Section 4.2.1). Time has been scaled by the Alfvén timescale $\tau_A = 2(s_2 - s_1)/u_A$, with $u_A = B_{0s}$.

4.3 General features of Experiment #52

Because all of the models listed in Table 4.1 were started from previous models, not from scratch, it is not possible to determine how long it takes a typical model to reach statistical equilibrium. In an effort to constrain the time required, however, a model using the same control and grid parameters as Experiment #52 was started "from scratch", as specified in Section 4.2.1. Figure 4.4 shows the evolution of the mechanical energy in this model, while Figure 4.5 shows the evolution of its thermal energy.

Both energy plots clearly illustrate the different regimes a model passes through when it is started. Initially, the small-scale, small-amplitude features introduced in the ψ vector experience unstable, exponential growth in size and strength. When energy peaks, nonlinear

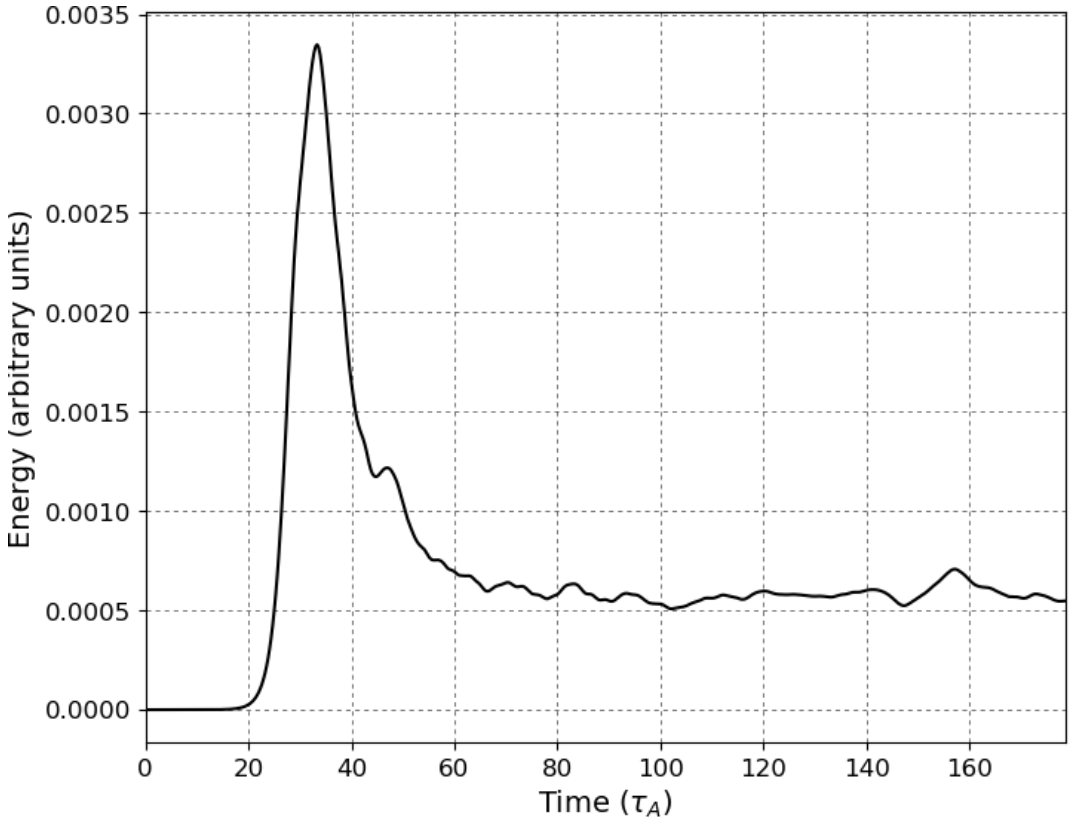

Figure 4.5: Evolution of the thermal energy in a version of Experiment #52 which was initialized from scratch (that is, was not restarted from a previous experiment; see Section 4.2.1). Time has been scaled by the Alfvén timescale $\tau_A = 2(s_2 - s_1)/u_A$, with $u_A = B_{0s}$.

effects begin to dominate the model's dynamics – flows become turbulent and thermal energy is transported from the inner to the outer boundary more efficiently. As the built-up thermal energy is expunged, the model settles around a statistical equilibrium, with energies fluctuating about a mean value. Transient dynamics have at this point died away, and the model has entered a state which may be sensibly analyzed. Figures 4.4 and 4.5 show this regime to be entered after about 100 Alfvén timescales, or around 130 rotations of the system. For the remainder of this thesis, is is assumed that the models being discussed are in this statistical equilibrium.

Figure 4.6 shows how the magnetic and mechanical components of the zonal energy in the same experiment vary with time. Again, both fluctuate about a mean energy level after about 70 Alfvén timescales. Of greater note is how changes in the mechanical energy lead changes in the magnetic energy. This is because much of the zonal magnetic field is induced by shear in the zonal flow. As zonal flow velocities increase, so will the amount of zonal induction, which after a period of time leads to an increase in the magnitude of the zonal magnetic field.

Figure 4.7 shows a snapshot in time of the non-axisymmetric vorticity, ω_z, and the non-axisymmetric current, j_z, after Experiment #52 has reached statistical equilibrium. The presence of eddies in both the flow and in the magnetic perturbation field are clearly visible. The magnetic perturbation field exhibits structures with larger wavelengths than those in the flow field, and with smoother features. This is a consequence of setting $P_m = 0.1$, causing magnetic diffusion to be stronger than viscous diffusion.

Figure 4.8 illustrates the radial and azimuthal components of the non-axisymmetric velocity field at the same time point as that shown in Figure 4.7, and Figure 4.9 does the same for the non-axisymmetric magnetic perturbation field. While both u_ϕ and b_ϕ exhibit similar spiral patterns as does j_z, u_s and b_s do not appear very similar to either ω_z or j_z. Despite

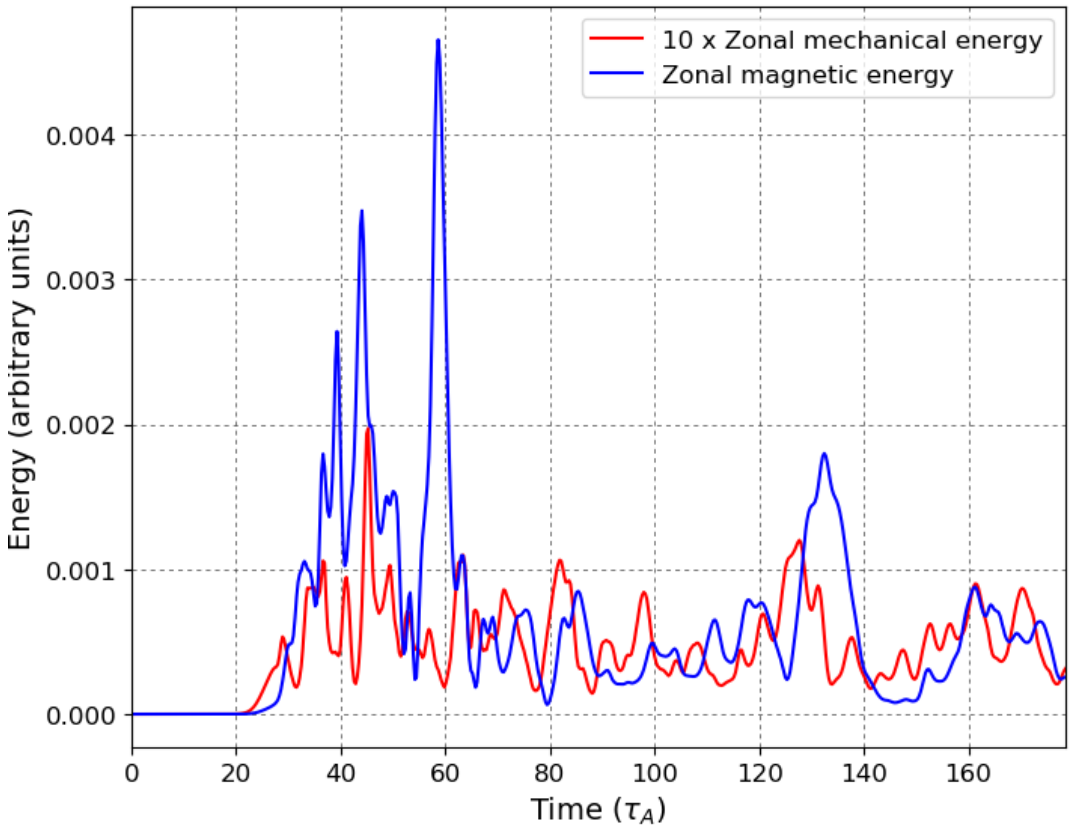

Figure 4.6: Evolution of the magnetic (blue) and mechanical (red) zonal energy in a version of Experiment #52 which was initialized from scratch (that is, was not restarted from a previous experiment; see Section 4.2.1). Time has been scaled by the Alfvén timescale $\tau_A = 2(s_2 - s_1)/u_A$, with $u_A = B_{0s}$.

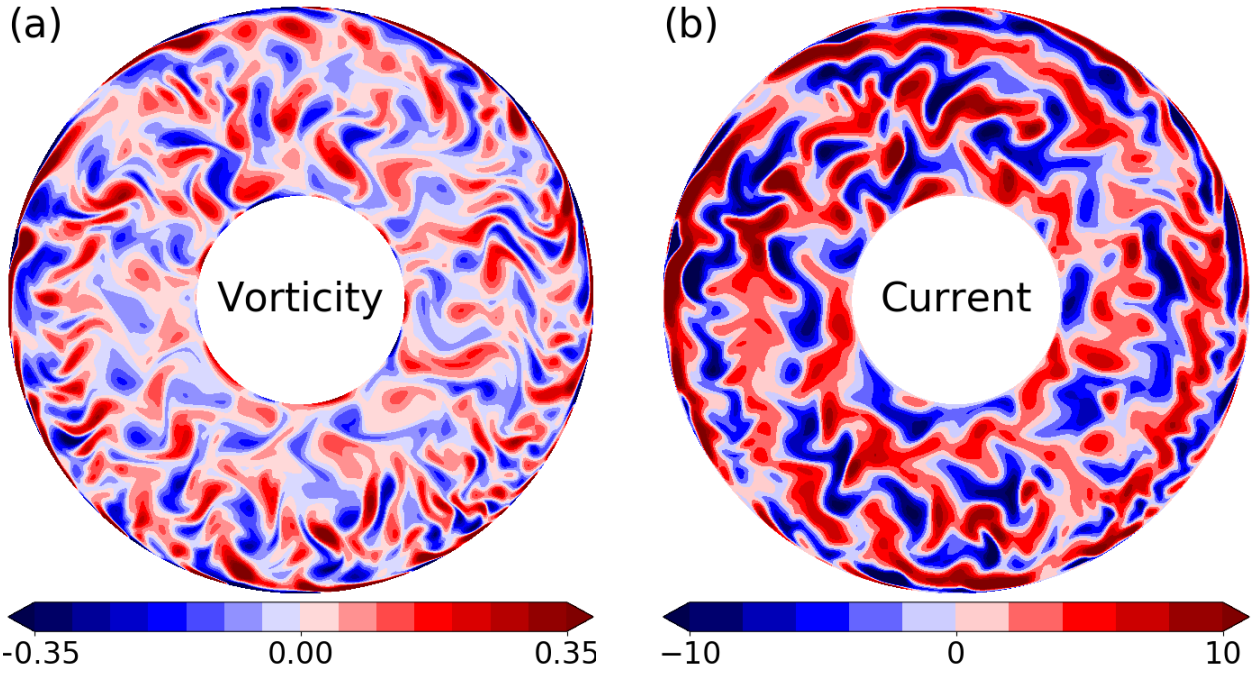

Figure 4.7: Snapshots of Experiment #52 at time equivalent to $44\tau_A$ on Figure 4.12, showing (a) the non-axisymmetric vorticity ω_z and (b) the non-axisymmetric axial current j_z, as seen looking downward from the north pole. Root-mean-square values are $\mathrm{RMS}(\omega_z) = 0.12$, $\mathrm{RMS}(j_z) = 5.19$.

this, the overall structures of the velocity and magnetic perturbation fields are clearly very strongly related to one another, as is expected from the equations coupling them together.

Typical u_{RMS} and b_{RMS} values after equilibration are 0.003 and 0.15, respectively. Because $|\mathbf{u}|$ is equivalent to the local Rossby number, and $|\mathbf{b}|$ to the local Lehnert number, we have $R_o \ll 1$ and $\lambda < 1$. The QG approximation is therefore valid, if only just in the case of the magnetic field.

Defining the experimental Alfvén and Lundquist numbers as

$$\mathcal{A} = \frac{u_{\mathrm{RMS}}}{B_{0s}} \quad \text{and} \quad \mathrm{Lu} = \frac{b_{\mathrm{RMS}}}{u_{\mathrm{RMS}}}\,, \tag{4.2}$$

Experiment #52 has a typical $\mathcal{A} \approx 0.02$ and $\mathrm{Lu} \approx 56$. This is within the region of parameter space where we expect a clear separation of magnetic and eddy timescales, and where we

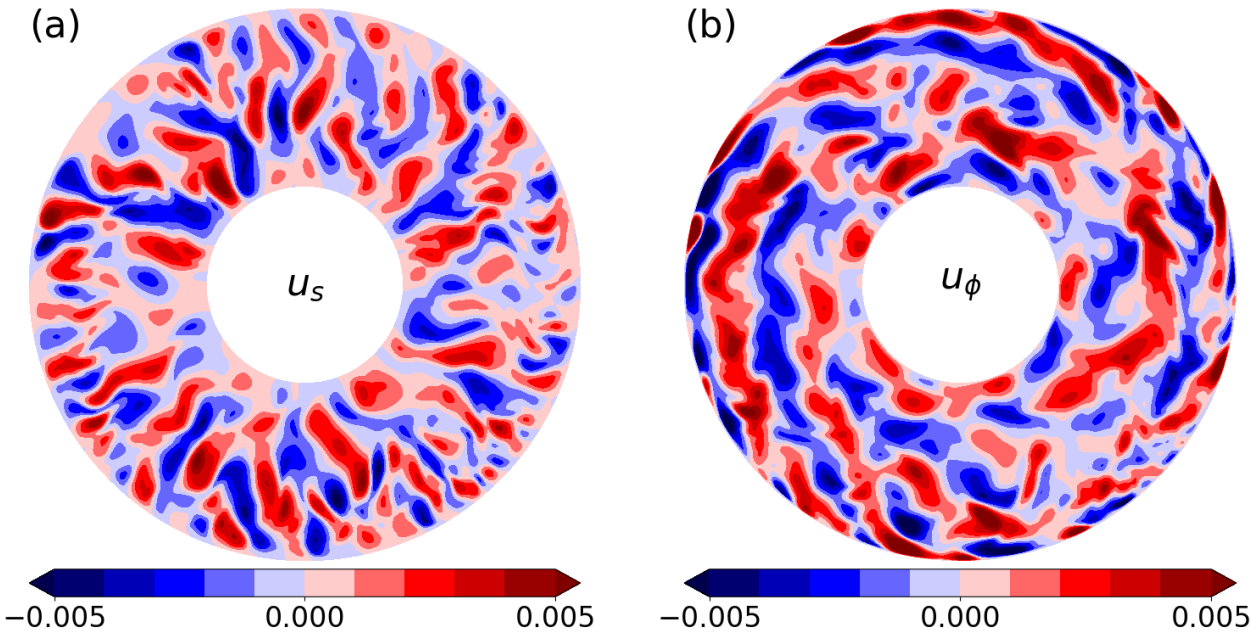

Figure 4.8: Snapshots of Experiment #52 at time equivalent to $44\tau_A$ on Figure 4.12, showing (a) the non-axisymmetric radial velocity u_s and (b) the non-axisymmetric azimuthal velocity u_ϕ, as seen looking downward from the north pole. Root-mean-square values are $\mathrm{RMS}(u_s) \approx 1.64 \times 10^{-3}$ and $\mathrm{RMS}(u_\phi) \approx 2.12 \times 10^{-3}$ ($u_{\mathrm{RMS}} \approx 2.68 \times 10^{-3}$).

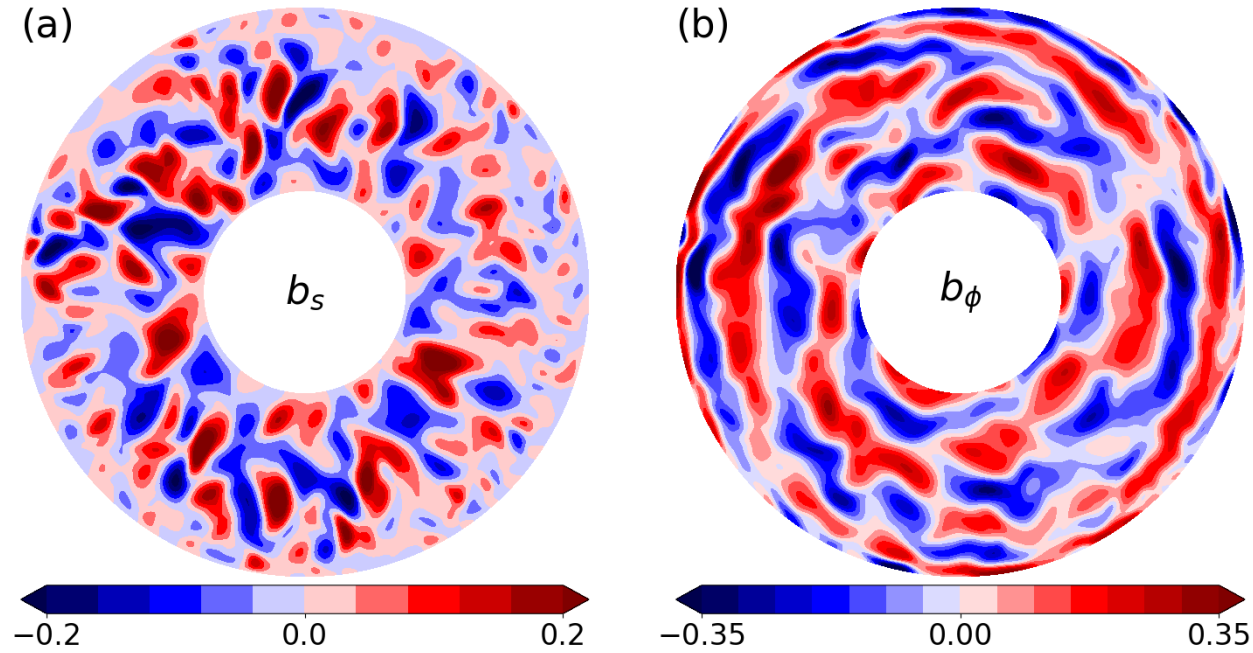

Figure 4.9: Snapshots of Experiment #52 at time equivalent to $44\tau_A$ on Figure 4.12, showing (a) the non-axisymmetric radial magnetic perturbation field b_s and (b) the non-axisymmetric azimuthal magnetic perturbation field b_ϕ, as seen looking downward from the north pole. Root-mean-square values are $\mathrm{RMS}(b_s) \approx 0.071$ and $\mathrm{RMS}(b_\phi) \approx 0.131$ ($b_{\mathrm{RMS}} \approx 0.150$).

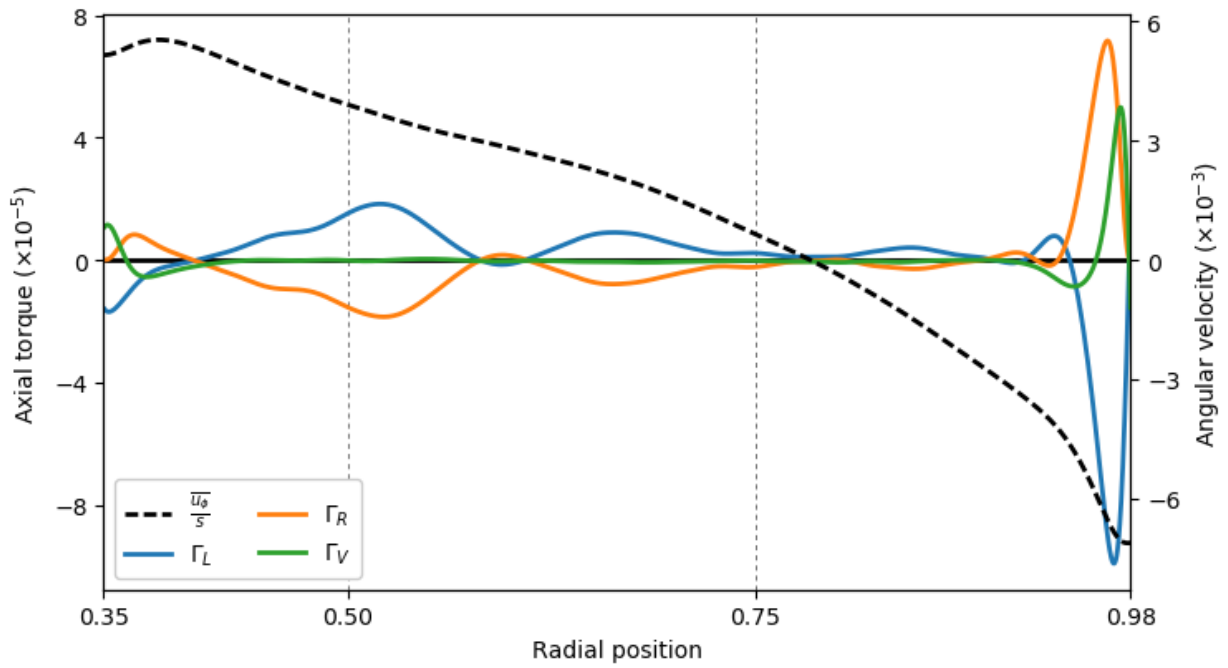

Figure 4.10: Time-averaged mean axial torques (solid lines) and time-averaged zonal angular velocity (dashed line) as a function of radius for Experiment #52.

expect the Lorentz torque ($\Gamma_{\mathrm{L}} = \Gamma_{\mathrm{L}_1} + \Gamma_{\mathrm{L}_2}$) to dominate the Reynolds torque (Γ_{R}). In short, this is a regime where long-timescale, magnetically-forced zonal accelerations similar to those in Earth's core should reside.

4.4 Time-averaged axisymmetric torque balance

The dashed black line of Figure 4.10 shows the time-averaged zonal angular velocity. Its profile is dominated by a shear flow spanning the whole of the modelled region, retrograde at the outer boundary and prograde at the inner boundary. The amplitude of this shear flow is of the same order of magnitude as the amplitude of typical convective eddies.

The mean zonal flow of Figure 4.10 differs from the one typically observed in the absence of a magnetic field. In non-magnetic convection with stress-free boundaries, the direction

of the mean zonal flow is reversed – it is prograde at the equator – and its characteristic velocity is much larger than the velocities associated with convective eddies. It results from time-averaged Reynolds stresses, themselves being the product of the topographic beta effect acting on convective eddies (e.g. Cardin and Olson, 1994; Christensen, 2001). In such experiments, zonal mechanical energies typically dominate non-zonal mechanical energies.

In the presence of an axisymmetric radial magnetic field, the same shear flow induces an axisymmetric Lorentz torque (Γ_{L_1}) opposing the shear which limits the growth of the zonal flow. In three-dimensional models, this zonal flow is not z-invariant (e.g. Aubert, 2005). In our QG model, because the magnetic perturbation is defined with a built-in topographic beta effect identical to that of the flow, a time-averaged Maxwell torque (Γ_{L_2}) is maintained in the same way as the time-averaged Reynolds stress. Since Γ_{L_2} has the same form, but opposite sign, as Γ_{R}, and since the former typically dominates the latter in our model, the direction of the driven mean zonal flow is reversed to that produced in non-magnetic convection. The effective braking of the zonal wind results in zonal mechanical energies in magnetoconvection experiments to be comparable to the nonzonal mechanical energies, as shown in Figure 4.4.

The time-averaged $\frac{\overline{u_\phi}}{s}$ profile is, then, the result of a balance between the time-averaged Lorentz torque and the time-averaged Reynolds torque. Figure 4.10 illustrates this, showing the time-averaged part of the Reynolds (orange), Lorentz (blue), and viscous (green) torques as functions of radius. Γ_{V} plays a secondary role in the balance near the boundaries, especially the outer one where the β effect amplifies all three torques. Away from the boundaries, the Reynolds and Lorentz torques largely balance one another. Note that both Γ_{L_1} and Γ_{L_2} are individually much larger than Γ_{R}, as shown by Figure 4.11. However, they tend to cancel one another, leaving a net Lorentz torque several orders of magnitude smaller than either one individually. This self-cancellation will be re-examined in Section 4.6.

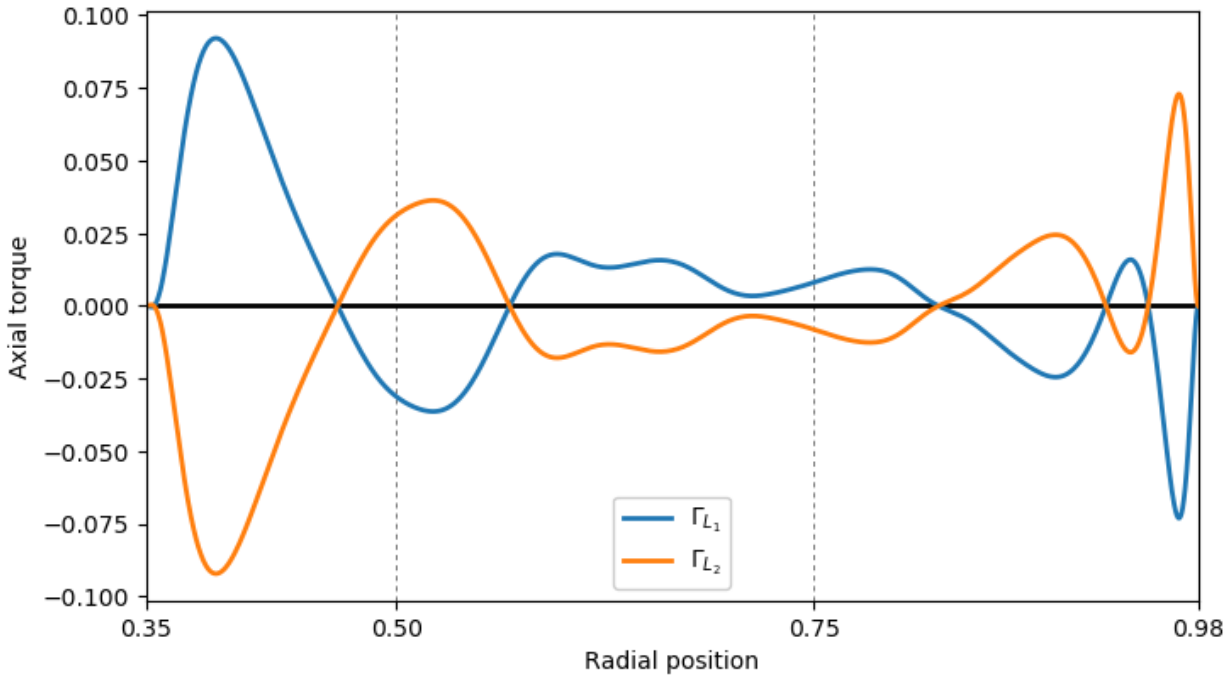

Figure 4.11: Time-averaged components of the mean axial Lorentz torque as a function of radius for Experiment #52.

4.5 Zonal accelerations

Fluctuations in time with respect to this mean torque balance are the main focus of our study. Figure 4.12 shows the zonal angular accelerations (top panel) and the time-varying parts of Γ_{L}, Γ_{R}, and Γ_{V} (bottom three panels) after the system has equilibrated. Fluctuations in Γ_{L} have a typical amplitude five times larger than those of Γ_{R}: $\sim 6.6 \times 10^{-5}$ versus $\sim 1.2 \times 10^{-5}$. Γ_{V} is afforded a tertiary role in the time-dependent dynamics, with RMS fluctuations of the order of $\sim 0.3 \times 10^{-5}$.

Thus, fluctuations in our model's mean zonal accelerations are mainly controlled by the Lorentz torque. Indeed, the upper two panels of Figure 4.12 suggest a strong correlation at all times and radii between $\frac{\partial}{\partial t}\left(\frac{\overline{u_\phi}}{s}\right)$ and Γ_{L}. Time on Figure 4.12 has been scaled to the timescale of the fundamental Alfvén wave mode, $\tau_A = 2(s_2 - s_1)/u_A$. An estimate of the characteristic timescale of the slow zonal flow fluctuations is $\tau_{\mathrm{slow}} \approx 10\ \tau_A$. Scaling τ_{slow} to

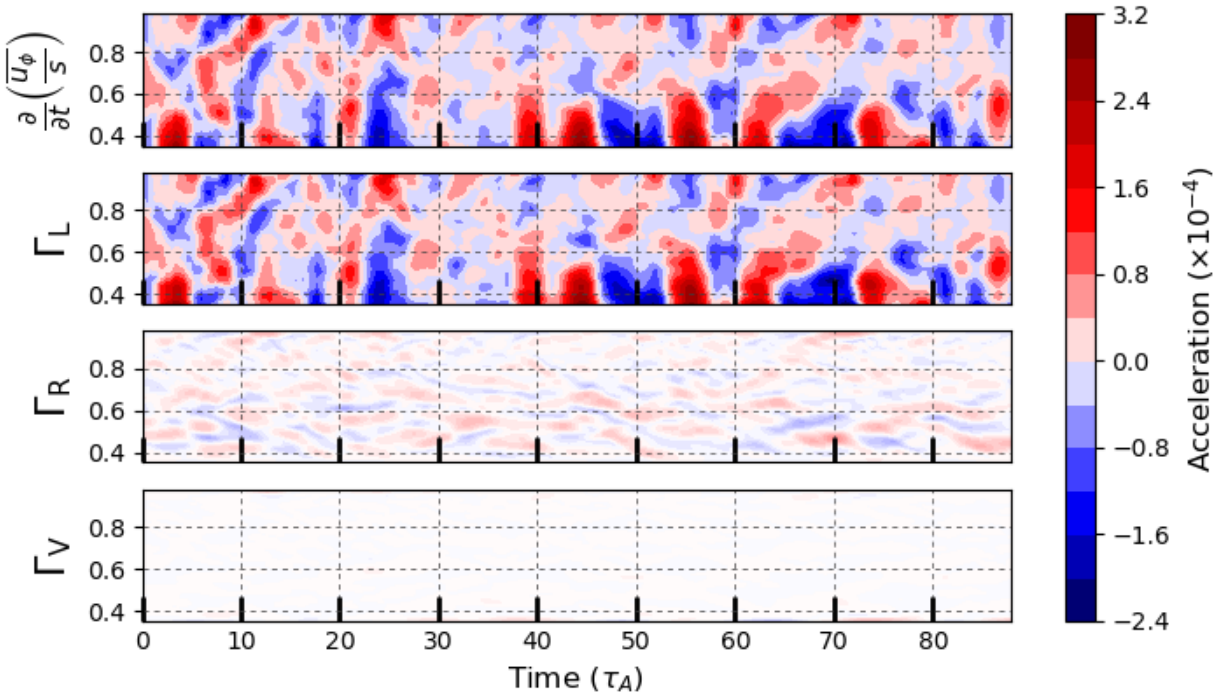

Figure 4.12: The zonal angular acceleration (top panel), and the time-dependent parts of the Lorentz (second panel), Reynolds (third panel) and viscous (bottom panel) torques, as functions of cylindrical radius and time from Experiment #52. The time-averaged contribution to each torque (shown in Fig.4.10) has been removed. Time has been scaled by the Alfvén timescale $\tau_A = 2(s_2 - s_1)/u_A$, with $u_A = B_{0s}$.

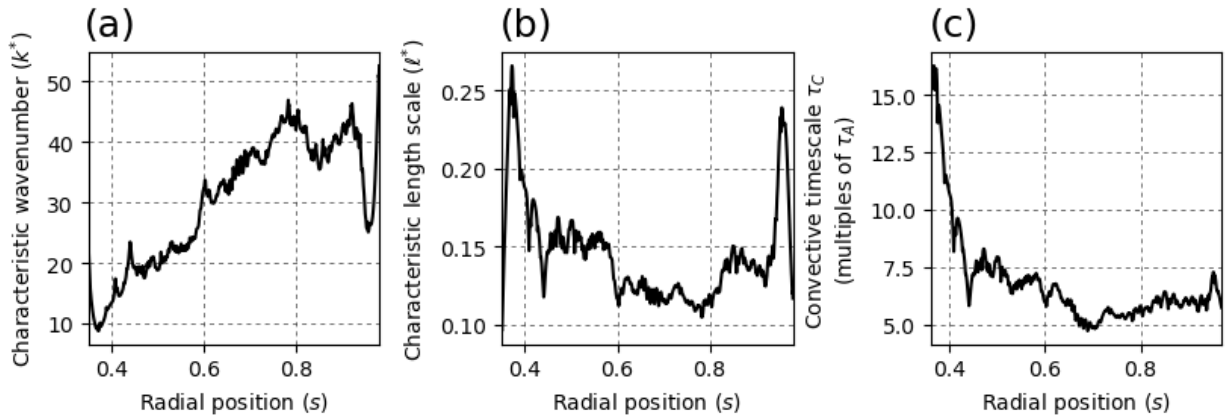

Figure 4.13: Characteristic (a) wave numbers, (b) length scales, and (c) time scales as a function of radius for Experiment #52, calculated at time $44\tau_A$ in Figure 4.12.

Earth's core, taking $\tau_A \approx 6$ yr, gives a timescale of 60 yr for these slow zonal accelerations – a similar timescale to the zonal accelerations inferred to exist within Earth's core. As would be expected for a parameter regime in which $\mathcal{A} < 1$, the fluctuations in $\mathbf{b}$ which lead to these slow zonal accelerations must therefore occur on timescales longer than the Alfvén wave propagation timescale.

To further demonstrate that the slow magnetic field fluctuations originate from the underlying convective dynamics, the characteristic wave number (e.g. Takahashi et al., 2008) is computed at each radius s from the convective speed $u = |\mathbf{u}|$:

$$k^*(s) = \frac{\int k' u(k')\,\mathrm{d}k'}{\int u(k')\,\mathrm{d}k'}\,. \tag{4.3}$$

The result of this calculation as a function of radius, for a typical snapshot of the model, is shown in panel (a) of Figure 4.13. The characteristic convective length scale $\ell_C(s)$ is then calculated from the characteristic wavenumber as

$$\ell_C(s) = \frac{2\pi s}{k^*(s)}\,. \tag{4.4}$$

The characteristic convective length scale for all radial positions is shown in panel (b) of

Figure 4.13. Dividing these length scales by the RMS velocities at each radius yields the characteristic convective timescales:

$$\tau_C(s) = \frac{\ell_c}{u_{\rm RMS}} \approx 6\tau_{\mathcal{A}}\,. \tag{4.5}$$

As shown in panel (c) of Figure 4.13, these timescales vary somewhat with radius, and they also vary slightly with time. However, in the bulk of the fluid, τ_C – which represents the time required for the flow to create significant changes in the magnetic field – is typically $5-8\tau_{\mathcal{A}}$ for this experiment, which is of the same order as $\tau_{\rm slow}$. Thus, the results shown on Figure 4.12 demonstrate that it is possible to drive decadal zonal accelerations in Earth's core by fluctuating Lorentz torques, themselves driven by underlying convective flows shearing and advecting the magnetic field.

In addition to the slow fluctuations of Figure 4.12, the convective dynamics also generate free Alfvén waves. Figure 4.14 shows the second half of the zonal acceleration and Lorentz torque panels of Figure 4.12 after applying a highpass filter to remove fluctuations with periods longer than 1.19 τ_A. This reveals the presence of periodic fluctuations with a period of approximately 1 τ_A. The correlation between the acceleration and Lorentz torque shows that these are indeed Alfvén waves. (Applying the same highpass filter to $\Gamma_{\rm R}$ and $\Gamma_{\rm V}$ produces only low-amplitude noise.)

Left on their own, free Alfvén oscillations should decay away because of ohmic dissipation. In our model, they are continuously re-excited by the underlying convective dynamics, though resonant amplification remains modest and their amplitude does not rise much higher than that resulting from the forced background accelerations. Their typical RMS velocities of 1×10^{-4} are approximately 7 times smaller than the RMS velocities of 7×10^{-4} found for the slower zonal flow fluctuations. This is the reason why Alfvén waves, though present, are not apparent on Figure 4.12.

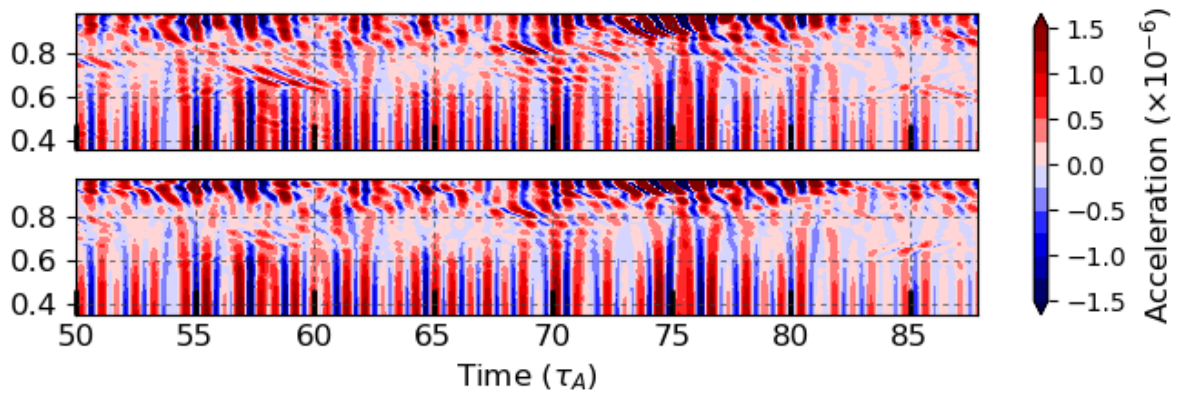

Figure 4.14: Output of a highpass filter applied to the second half of the zonal angular accelerations (top panel) and Lorentz torques (bottom panel) of Fig.4.12. In our nondimensional time units, the 8th-order digital Butterworth filter's -3 dB frequency is 1/10.

The Alfvén waves on Figure 4.14 which we observe in our model are also observed in the Earth's core, with a typical amplitude of ~ 0.2 km yr^{-1} and a typical period of 6 yr (Gillet et al., 2010, 2015). The typical amplitude of the observed decadal zonal flows is of the order of 2 km yr^{-1}, or 10 times greater – the same difference of an order of magnitude achieved by our model. Furthermore, our model also reproduces the amplitude ratio between the decadal zonal flows and typical large scale flow eddy velocities. At the top of Earth's core, the flow amplitude is approximately 10 km yr^{-1}, or 5 times greater than that of the decadal oscillations. In our model, the RMS amplitude of zonal flows is 2.4×10^{-3}, or 3 times that of the slow fluctuations. Thus, the approximate ratios between both the amplitudes of the total zonal flow and decadal fluctuations and between the decadal fluctuations and free Alfvén waves are captured by our model. This gives us confidence that our model is a good analogy for the zonal flow dynamics of Earth's core.

4.6 Taylorization

As discussed in Section 1.5, Taylor (1963) showed that in the absence of inertia and viscosity, magnetic torques must vanish when integrated over the surface of a geostrophic cylinder in order to maintain a steady-state solution. This does not imply that the local magnetic torque at any individual point on the geostrophic cylinder is zero. Instead, there is perfect cancellation: local magnetic torques, possibly quite large, cancel one another out when averaged over the entire surface.

In a more dynamic system, local magnetic torques averaged over geostrophic cylinders may not exhibit perfect cancellation, resulting in azimuthal accelerations of those cylinders. The "Taylorization" of such a system is simply a measure of how *much* the local magnetic torques cancel when averaged. In our model, where the magnetic field (and therefore the magnetic torque) is assumed to be axially invariant, the Taylorization is measured by the factor $\mathcal{T}$:

$$\mathcal{T}(s) \equiv \frac{\left| \oint \mathcal{M}_\phi(s,\phi)\, \mathrm{d}\phi \right|}{\oint |\mathcal{M}_\phi(s,\phi)|\, \mathrm{d}\phi} = \frac{|\Gamma_\mathrm{L}(s)|}{\oint |\mathcal{M}_\phi(s,\phi)|\, \mathrm{d}\phi}\,, \tag{4.6}$$

where $\mathcal{M}_\phi(s,\phi)$ represents the azimuthal component of the local magnetic torque. A system with low Taylorization has $\mathcal{T} \lesssim 1$, while a system with a high Taylorization has $\mathcal{T} \ll 1$. Typical geodynamo simulations achieve $\mathcal{T} \approx 10^{-1} - 10^{-3}$ (e.g. Rotvig and Jones, 2002; Wicht and Christensen, 2010; Teed et al., 2014).

Figure 4.15 shows the Taylorization factor of our model as a function of cylindrical radius and time. Typical RMS values of $\mathcal{T}$ are approximately 3.2×10^{-4}, with peak values of 2.6×10^{-3}. As shown in the previous section, temporal fluctuations of the magnetic field lead to temporal fluctuations of the Lorentz torque. Thus, Taylor's constraint is continually broken, with the Lorentz torque fluctuations being accommodated by rigid zonal accelerations. This can be observed in Figure 4.12, where the times and radii of the largest zonal

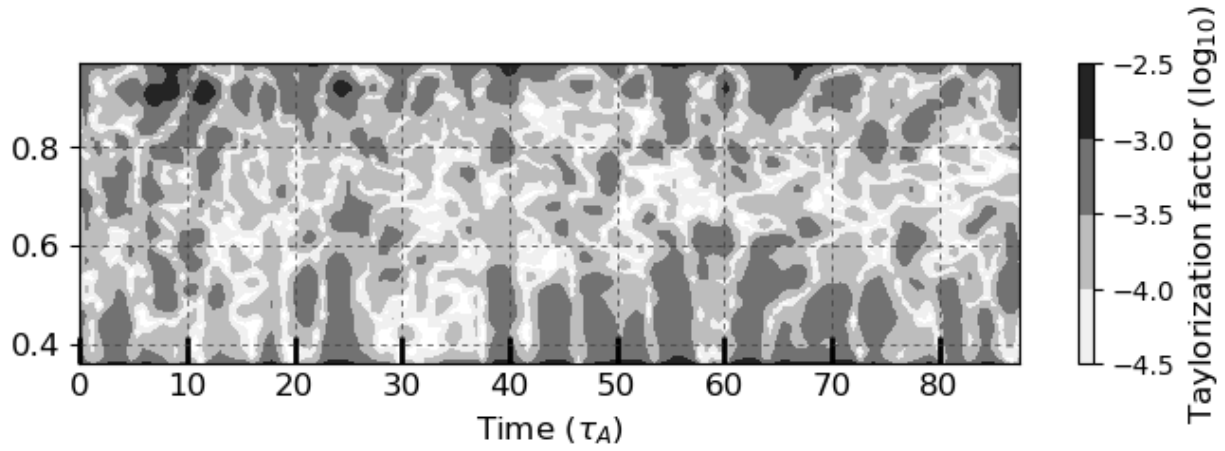

Figure 4.15: Taylorization factor $\mathcal{T}$ as a function of radius and time for Experiment #52. With our choice of boundary conditions, the Taylorization factor equals 1 at the boundaries. Only $s \in [0.36, 0.97]$ is shown.

accelerations often coincide with the largest values of $\mathcal{T}$ in Figure 4.15.

Therefore, our model is not in a perfect Taylor state at any given moment, but instead fluctuates about a state characterized by a low Taylorization factor. A part of the large cancellation of the Lorentz torque over any given geostrophic cylinder is inherent to the form of the Maxwell torque (Γ_{L_2}), as it involves products of the magnetic field vectors which change direction at different azimuthal points. Much of the remaining cancellation results from the sum of Γ_{L_1} and Γ_{L_2}, as shown by Figure 4.11.

If our model is to conserve angular momentum in the absence of inertia (Γ_R) and viscosity (Γ_V), the time-averaged Lorentz torque $\{\Gamma_L\} = \{\Gamma_{L_1} + \Gamma_{L_2}\}$ must be zero. However, Figure 4.10 shows that $\{\Gamma_L\} \neq 0$. This is because Γ_R and Γ_V *are* included: angular momentum is conserved by balancing $\{\Gamma_L\}$ against the next-largest time-averaged torque. Figure 4.10 shows this next-largest torque to be $\{\Gamma_R\}$.

Chapter 5

Discussion

5.1 Slow Zonal Accelerations

Our model shows that in an Earth-like parameter regime characterized by $\mathcal{A} \ll 1$ and $\mathrm{Lu} \gg 1$, convective flows can drive fluctuations in the magnetic field which then lead to temporal fluctuations in the magnetic torque. The latter generates zonal accelerations in the form of free Alfvén waves, but also slower forced zonal accelerations on a timescale related to the convective flows. Our results suggest that the inferred decadal zonal accelerations of geostrophic cylinders in the Earth's core can be explained by forced fluctuations of the Lorentz torque, themselves driven by the underlying convection.

Although our dynamical model is in the correct parameter regime in terms of $\mathcal{A} \ll 1$ and $\mathrm{Lu} \gg 1$, other parameters remain far from Earth-like, notably the Ekman number (5.0×10^{-6}, vs. $\sim 10^{-15}$ in the outer core) and magnetic Prandtl number (0.1, vs. $\sim 10^{-5}$ in the outer core). Care must then be taken when extrapolating our results to Earth's core. To further confirm that our results appropriately capture the decadal timescale dynamics of zonal flows in the core, it would be desirable to conduct many more numerical experiments, systematically varying some of the input parameters in order to develop scaling properties for our

model. An alternative approach would be to attempt the tuning of a 3D self-sustaining dynamo model to produce the magnetically-forced zonal accelerations we argue are responsible for decadal fluctuations in the length of day. Some existing geodynamo models are approaching the parameter regime of $\mathcal{A} \ll 1$ and $\mathrm{Lu} \gg 1$ already (e.g. Aubert et al., 2017; Schaeffer et al., 2017). Short of doing this, some speculation may be made as to how the use of more Earth-like Ekman and magnetic Prandtl numbers would affect the dynamics of zonal flows.

For the relatively large Ekman numbers of our numerical experiments, viscous forces remain important in the establishment of the large-scale, core-size eddies visible on Figure 4.7 (e.g Aurnou et al., 2015). However, at $E \sim 10^{-15}$, as inferred for Earth's core, the $E^{1/3}$ scaling law suggests that the typical size of viscously-controlled eddies should be much smaller, at about 10^{-5} times the size of the core or roughly of the order of 10-100 m. These are *much* smaller than those shown in Figure 4.7. Such small eddies would be inefficient at generating the core-size changes in the magnetic field required to drive large-scale zonal accelerations.

However, the geomagnetic secular variation allows the presence of large-scale eddies in Earth's core to be inferred. The length scale of such eddies must necessarily be set by something other than viscous forces. Two mechanisms may play a role. First, sufficiently low Ekman numbers, small-scale structures feed their energy to larger scales via an inverse energy cascade driven by geostrophic turbulence (e.g. Guervilly et al., 2014; Stellmach et al., 2014). Second, the influence of the Lorentz force should lead to larger convective length scales (e.g. Roberts and King, 2013). In fact, this effect is starting to be seen in numerical models (e.g. Matsui et al., 2014; Yadav et al., 2016; Schaeffer et al., 2017). While both of these efects are likely present in Earth's core, both are absent in our models.

However, the mechanism we demonstrate for driving decadal-timescale zonal accelerations

depends only on the presence of such large-scale eddies, not the dynamics governing them. While those of our model are not formed in the same way as in the core, they nevertheless serve the same purpose, stretching and shearing the magnetic field on convective timescales.

The magnetic Prandtl number in the core is much lower than the one we have chosen in our numerical experiment. Since a lower P_m corresponds to enhanced magnetic diffusion, temporal changes in the magnetic field would be dominantly controlled by the largest length scales of the underlying convective flow. Thus, while small-scale eddies certainly exist in the core, changes in the magnetic field should still preferentially occur at the largest length scale. We therefore expect that temporal changes in the Lorentz torque can drive decadal zonal accelerations at core-size wavelength in the radial direction, just as we observe in our numerical experiment of limited spatial resolution.

5.2 Free Alfvén waves

As shown in Fig. 4.14, our dynamical model excites free Alfvén waves. The ratio between the amplitudes of the slow zonal acceleration and the free Alfvén waves is of the order of 10, as is the case in Earth's core. Although we capture this ratio correctly, the spatio-temporal properties of Alfvén waves in our model differ from those detected in Earth's core. In our model, they are dominated by a standing wave oscillation of the fundamental mode. In Earth's core, they take the form of outward travelling waves (Gillet et al., 2010, 2015).

The reason why Alfvén waves in Earth's core travel outward, as well as their excitation mechanism, remain unclear. Outward travelling Alfvén waves resulting from a quasi-periodic triggering near the tangent cylinder are observed in some numerical models (Teed et al., 2014, 2015; Schaeffer et al., 2017). When approaching an Earth-like regime, Lorentz forces are responsible for this torque, but the precise physical mechanism has not been clearly identified.

It would be a valuable effort to investigate where and how Alfvén waves are excited in our model. Since we do not see a preferential propagation direction, excitation appears to be distributed evenly within the domain of integration. The region close to the tangent cylinder does not appear to be the seat of of any form of recurrent instability, although this may be because we have not modelled the dynamics inside the tangent cylinder.

Given that convective flows in our model induce changes the magnetic field on a broad range of timescales, Alfvén waves on Fig. 4.14 may simply represent the resonant response to fluctuations of the Lorentz torque that occur in the vicinity of their free period range. Indeed, correlations between Figs. 4.14 and 4.15 suggest that this is the case: notable increases in the Taylorization factor are often, though not always, associated with an amplitude enhancement of free Alfvén waves. This argues along the same line of a recent study which has shown that applying a stochastic forcing in the volume of the core readily excites Alfvén waves (Gillet et al., 2017). Moreover, the study of Gillet et al. (2017) has also shown that electromagnetic dissipation at the CMB transforms standing Alfvén waves into outward travelling waves, with similar characteristics as those detected in the Earth's core. Our model constitutes a dynamical realization of such a stochastic forcing and supports the idea that Alfvén waves in Earth's core are simply the response to sub-decadal changes in the Lorentz torque within the bulk of the core. Our model does not include dissipation at the CMB, but we believe (though this should be tested) that adding it would also transform our standing Alfvén waves into outwardly propagating waves.

5.3 Taylorization

Taylor's constraint is continuously being broken in our model, generating zonal accelerations in response. The numerical value of the Taylorization factor associated with these fluctuations is of the order of 10^{-3}, similar to that extrapolated for the outer core using recent geodynamo models (Aubert et al., 2017). The time-average state about which these fluctuations occur is characterized by a higher degree of Taylorization, though it is not a perfect Taylor state. The degree to which Taylor's constraint is broken depends on the strength of the largest of the non-magnetic torques ($\Gamma_{\mathrm{R}}, \Gamma_{\mathrm{V}}$). In our model, the torque from Reynolds stresses dominates the viscous torque and acts as the main balance to the time-averaged Lorentz torque.

The results of our model suggest that, as was pointed out by Dumberry and Bloxham (2003), the torque from Reynolds stresses in Earth's core likely also provides the leading order departure from a time-averaged Taylor state. Because the Alfvén number in our model is similar to that in Earth's core, the baseline Taylorization factor of approximately 10^{-4} in Fig. 4.15 may also be representative of that expected in Earth's core. As our model is two-dimensional, extrapolation of our results to the three-dimensional magnetic field of Earth is clearly not straightforward. Nevertheless, with such a high Taylorization, large cancellations in Lorentz torque over a cylinder must still occur. It this sense, exploring dynamo solutions in the limit of a vanishing Lorentz torque remains a worthy goal (e.g. Livermore et al., 2008; Wu and Roberts, 2015). This being said, one must keep in mind that the correct Taylorization factor in Earth's core may not be asymptotically close to zero, but may instead be closer to 10^{-4}.

Chapter 6

Conclusion

For this thesis, a two-dimensional reduced model of rotationally-dominated magnetoconvection was constructed. This model is capable of producing distinct accelerations in the mean zonal flow on both short and long timescales. The short-timescale accelerations are the signature of free Alfvén waves, while the long-timescale accelerations are magnetically forced by the Maxwell torque. The temporal changes in the magnetic field which drive the time-varying Maxwell torque are produced by the underlying convective flows, which shear and advect the magnetic field on a timescales associated with convective eddies. These results provide a dynamical explanation for the rigid decadal zonal accelerations that are inferred to exist in Earth's core on the basis of changes in the observed magnetic field and changes in the length of day (LOD).

This explanation offers an alternative to the suggestion that the decadal zonal accelerations are the signature of free MAC waves propagating through a stably-stratified layer at the top of the outer core (Buffett, 2014; Buffett et al., 2016). While such MAC waves may well exist, they must coexist with the deep-seated, convectively-driven zonal flows predicted by our model. In fact, the reverse of the effect proposed by Buffett et al. (2016) may be true: instead of deep zonal flows resulting from MAC waves in a stratified layer coupling with the

deeper core, zonal flows in the deep core may couple to the stratified layer and induce MAC waves. However, because of the strong match between the observed LOD and predictions based on purely rigid flows, we speculate that any non-rigid MAC waves make up only a fraction of the total zonal flow.

6.1 Future Directions

The modest computational resources required by our model make it well-suited to simulating dynamics which conventional three-dimensional models may find too numerically demanding, especially at lower Ekman numbers. While recent 3D models have reached Ekman numbers of $\sim 10^{-7}$ (e.g. Schaeffer et al., 2017), they remain far from the $10^{-14}-10^{-15}$ estimated for the outer core. Previous studies have found that, as the Ekman number decreases, the length scale of the magnetic field does not decrease as quickly as the length scale of convection (e.g. Takahashi et al., 2008). In the context of zonal accelerations, this suggests the nature of interaction between the convective and magnetic fields may also change as the Ekman number is decreased. For example, if magnetic features remain relatively constant in size as convective features shrink, the separation in timescale between free and forced oscillations may decrease if convective velocities remain the same. As the Ekman number is decreased further and convective length scales become small enough to start an inverse energy cascade, the magnetic perturbations responsible for the forced zonal accelerations may switch from being driven by small-scale convection to large-scale vortices arising from the cascade (e.g. Guervilly et al., 2014).

Future work should note that the magnetic background field used for this thesis is not consistent with the assumptions made in the derivation of the QG equations. In particular, while it is assumed that $\boldsymbol{\nabla} \cdot \mathbf{B}_0 = 0$, the use of $B_{0z} = \beta B_{0s} z$ with a uniform B_{0s} produces

a background field with a true divergence of $\boldsymbol{\nabla} \cdot \mathbf{B}_0 = B_{0s}\left(\frac{1}{s} + \beta\right)$. A divergence-free field could be achieved with the same B_{0z} profile by instead taking $B_{0s} = \frac{C}{sL}$, were C is an arbitrary constant. Such a field is stronger near the boundaries than in the bulk of the modelled region, which would likely have a significant impact on the behaviour of free Alfvén waves. In particular, since $u_A = |\mathbf{B}|$, the radial gradient in $\mathbf{B}$ would lead to a radially-dependent Alfvén velocity with a minimum at $s = \sqrt{\frac{1}{2}} \approx 0.707$. This could cause either the breaking or the excitation of Alfvén waves, whose propagation direction likely depends on the magnetic boundary conditions (Gillet et al., 2017).

Beyond zonal accelerations, our model could be adapted to study the coupling mechanisms which transfer angular momentum between the core and the mantle. There are several such mechanisms, including viscous forces, the flow field pushing against mantle topography, electromagnetic coupling, and gravitational coupling involving the inner core (e.g. Buffett, 2015). The second two in particular could be explored with our model.

If a radial magnetic field is allowed to penetrate the core-mantle boundary, the advection of the magnetic field by the flow at the top of the core will cause eddy currents to be induced in the lower mantle. The resulting Lorentz forces tend to brake the flow, and impart a net torque on the mantle itself (e.g. Stix and Roberts, 1984). This mechanism has been shown to be strong enough to potentially explain the observed LOD variations (e.g. Holme, 1998), though there remains some debate over the conductivity structure required at the bottom of the mantle to account not only for the LOD variations, but also for Earth's nutations (Buffett, 2015). At present, all boundaries in our model are assumed to have zero resistivity, or infinite conductivity. This implies that the spherically radial magnetic field must drop to zero at the spherical boundaries, precluding any electromagnetic coupling. Our model could be adapted to include electromagnetic coupling by allowing a radial magnetic field on the boundaries. This would amount to implementing a finite, nonzero conductivity at $s = s_1$

and $s = s_2$, as well as on the upper and lower spherical boundaries. In addition, the assumed B_{0z} and b_z profiles would need to be adjusted since the no-penetration boundary condition would no longer apply. The relatively modest computational requirements of our model would make this a more efficient (if also a slightly less realistic) way of studying various forms of electromagnetic coupling compared to a fully three-dimensional model.

If processes in the mantle deform the shape of the core-mantle boundary, the structure of the gravitational potential within the core will also change. If, for example, the core-mantle boundary is deformed such that its projection onto the equatorial plane is elliptical, the inner core will be deformed by gravity into a similar elliptical shape (e.g. Mound and Buffett, 2003). If the inner core is then rotated by couplings with process in the outer core (e.g. Glatzmaier and Roberts, 1996; Buffett and Glatzmaier, 2000), a gravitational restoring torque will be induced between the inner core and the mantle. This is gravitational coupling (e.g. Buffett, 1996a,b). Such a coupling could be incorporated into our model by tracking an additional parameter: the azimuthal displacement between the inner and outer annular boundaries caused by viscous or electromagnetic torques. An additional, gravitational, torque could then be calculated on the boundaries in proportion to the offset angle, possibly dependent on time to account for viscous relaxation of the inner core's shape. In conjunction with the electromagnetic core-mantle coupling described above, a study could then be made of the relative importance of the two types of coupling in the case of Earth.

Finally, the dynamics of a model never precisely match those of the real-life system being modelled, and over time the model tends to drift even further from the system's "true" state. For example, Hu and Skaggs (2009) report that precipitation levels in 6-10 day weather forecasts of the continental United States are accurate about 40% of the time. Data assimilation techniques use observations from the system's "true" state to nudge the model towards the "true" dynamics. These techniques have been well established in meteorology (e.g. Ghil

et al., 1991; Kalnay, 2003) and oceanography (e.g. Bertino et al., 2003), where they are used both in forward modelling (forecasting) and reanalyses (hindcasting) (e.g. Carton et al., 2000). Similar techniques could be applied to recover more accurate dynamics from appropriately modified core flow models (e.g. Fournier et al., 2010). Since the numerical cost of processing geodynamic and geomagnetic observations into model corrections tends to be quite high (Fournier et al., 2010), such techniques may be more easily adapted to reduced models such as ours than to fully three-dimensional models.

Bibliography

D. Alfè. The ab initio treatment of high-pressure and high-temperature mineral properties and behavior. In G. Schubert, editor, *Treatise on Geophysics*, chapter 2.15, pages 369–392. Elsevier, Oxford, 2nd edition, 2015.

H. Alfvén. On the existence of electromagnetic-hydrodynamic waves. *Arkiv För Matematik, Astronomi Och Fysik*, 29(2), 1943.

C. J. Allègre, J.-P. Poirier, E. Humler, and A. W. Hofmann. The chemical composition of the Earth. *Earth Planet. Sci. Lett.*, 134(3-4):515–526, 1995.

A. P. Anufriev, C. A. Jones, and A. M. Soward. The Boussinesq and anelastic liquid approximations for convection in the Earth's core. *Phys. Earth Planet. Inter.*, 152(3):163–190, 2005.

J. Aubert. Steady zonal flows in spherical shell dynamos. *J. Fluid Mech.*, 542:53–67, 2005.

J. Aubert, N. Gillet, and P. Cardin. Quasigeostrophic models of convection in rotating spherical shells. *Geochem. Geophys. Geosyst.*, 4(7):1052, 2003.

J. Aubert, T. Gastine, and A. Fournier. Spherical convective dynamos in the rapidly rotating asymptotic regime. *J. Fluid Mech.*, 813:558–593, 2017.

J. Aurnou, M. A. Calkins, J. S. Cheng, E. M. King, D. Nieves, K. M. Soderlund, and S. Stellmach. Rotating convective turbulence in Earth and planetary cores. *Phys. Earth Planet. Inter.*, 246:52–71, 2015.

G. E. Backus. Kinematics of geomagnetic secular variation in a perfectly conducting core. *Philos. Trans. R. Soc. London, Ser. A*, 263(1141):239–266, 1968.

L. Bertino, G. Evensen, and H. Wackernagel. Sequential data assimilation techniques in oceanography. *International Statistical Review*, 71(2):223–241, 2003.

J. Bloxham and A. Jackson. Fluid flow near the surface of Earth's outer core. *Rev. Geophys.*, 29(1):97–120, 1991.

S. I. Braginsky. Torsional magnetohydrodynamic vibrations in the Earth's core and variations in day length. *Geomag. Aeron.*, 10:1–10, 1970.

S. I. Braginsky and P. H. Roberts. Equations governing convection in Earth's core and the geodynamo. *Geophys. Astrophys. Fluid Dyn.*, 79:1–97, 1995.

D. Brouwer. A New Discussion of the Changes in the Earth's Rate of Rotation. *PNAS*, 38 (1):1–12, 1952.

S. G. Brush. Discovery of the Earth's core. *Am. J. Phys*, 48(9):705–724, 1980.

B. A. Buffett. A mechanism for decade fluctuations in the length of day. *Geophys. Res. Lett.*, 23(25):3803–3806, 1996a.

B. A. Buffett. Gravitational oscillations in the length of day. *Geophys. Res. Lett.*, 23(17): 2279–2282, 1996b.

B. A. Buffett. Tidal dissipation and the strength of the Earth's internal magnetic field. *Nature*, 468:952–954, 2010.

B. A. Buffett. Geomagnetic fluctuations reveal stable stratification at the top of the Earth's core. *Nature*, 507:484–487, 2014.

B. A. Buffett. Core-mantle interactions. In G. Schubert, editor, *Treatise on Geophysics*, chapter 8.08, pages 213–224. Elsevier, Oxford, 2nd edition, 2015.

B. A. Buffett and G. A. Glatzmaier. Gravitational braking of inner-core rotation in geodynamo simulations. *Geophys. Res. Lett.*, 27(19):3125–3128, 2000.

B. A. Buffett, N. Knezek, and R. Holme. Evidence for MAC waves at the top of Earth's core and implications for variations in length of day. *Geophys. J. Int.*, 204:1789–1800, 2016.

F. H. Busse and A. C. Or. Convection in a rotating cylindrical annulus: thermal Rossby waves. *J. Fluid Mech.*, 166:173–187, 1986.

P. Cardin and P. Olson. Chaotic thermal convection in a rapidly rotating spherical shell: consequences for flow in the outer core. *Phys. Earth Planet. Inter.*, 82(3-4):235–259, 1994.

J. A. Carton, G. Chepurin, X. Cao, and B. Giese. A Simple Ocean Data Assimilation Analysis of the Global Upper Ocean 1950-95. Part I: Methodology. *J. Phys. Oceanogr.*, 30(2):294–309, 2000.

B. F. Chao, W. Y. Chung, Z. R. Shih, and Y. K. Hsieh. Earth's rotation variations: a wavelet analysis. *Terra Nova*, 26(4):260–264, 2014.

U. R. Christensen. Zonal flow driven by deep convection in the major planets. *Geophys. Res. Lett.*, 28:2553–2556, 2001.

U. R. Christensen. A deep dynamo generating Mercury's magnetic field. *Nature*, 444:1056–1058, 2006.

D. C. Christodoulidis, D. E. Smith, R. G. Williamson, and S. M. Klosko. Observed tidal braking in the Earth/Moon/Sun system. *J. Geophys. Res.*, 93(B6):2156–2202, 1988.

T. G. Cowling. The dynamo maintenance of steady magnetic fields. *Q. J. Mech. Appl. Math.*, X(2):129–136, 1957.

G. A. de Wijs, G. Kresse, L. Vočadlo, D. Dobson, D. Alfè, M. J. Gillan, and G. D. Price. The viscosity of liquid iron at the physical conditions of the Earth's core. *Nature*, 392: 805–807, 1998.

V. Dehant and P. M. Mathews. Earth rotation variations. In G. Schubert, editor, *Treatise on Geophysics*, chapter 3.10, pages 263–305. Elsevier, Oxford, 2nd edition, 2015.

J. O. Dickey, P. L. Bender, J. E. Faller, X. X. Newhall, R. L. Ricklefs, J. G. Ries, P. J. Shelus, C. Veillet, A. L. Whipple, J. R. Wiant, J. G. Williams, and C. F. Yoder. Lunar laser ranging: A continuing legacy of the Apollo program. *Science*, 265(5171):482–490, 1994.

J. O. Dickey, S. L. Marcus, O. de Viron, and I. Fukumori. Recent Earth oblateness variations: Unraveling climate and postglacial rebound effects. *Science*, 298(5600):1975–1977, 2002.

M. Dumberry. Course 7 taylor's constraint and torsional oscillations. *Les Houches*, 88: 383–401, 2008.

M. Dumberry and J. Bloxham. Torque balance, Taylor's constraint and torsional oscillations in a numerical model of the geodynamo. *Phys. Earth Planet. Inter.*, 140(1-3):29–51, 2003.

M. Dumberry and C. C. Finlay. Eastward and westward drift of the Earth's magnetic field for the last three millennia. *Earth Planet. Sci. Lett.*, 254(1-2):146–157, 2007.

A. M. Dziewonski and D. L. Anderson. Preliminary reference Earth model. *Phys. Earth Planet. Inter.*, 25(4):297–356, 1981.

W. M. Elsasser. Induction Effects in Terrestrial Magnetism. Part I. Theory. *Phys. Rev.*, 69 (3-4):106–116, 1946a.

W. M. Elsasser. Induction Effects in Terrestrial Magnetism. Part II. The Secular Variation. *Phys. Rev.*, 70(3-4):202–212, 1946b.

W. M. Elsasser. Induction Effects in Terrestrial Magnetism. Part III. Electric Modes. *Phys. Rev.*, 72(9):821–833, 1947.

C. C. Finlay, M. Dumberry, A. Chulliat, and M. A. Pais. Short timescale core dynamics: Theory and observations. *Space Sci. Rev.*, 155(1):177–218, 2010.

A. Fournier, G. Hulot, D. Jault, W. Kuang, A. Tangborn, N. Gillet, E. Canet, J. Aubert, and F. Lhuillier. An introduction to data assimilation and predictability in geomagnetism. *Space Sci. Rev.*, 155(1-4):247–291, 2010.

M. Frigo and S. G. Johnson. The design and implementation of FFTW3. *Proceedings of the IEEE*, 93(2):216–231, 2005.

M. Ghil, , and P. Malanotte-Rizzoli. Data assimilation in meteorology and oceanography. *Advances in Geophysics*, 33:141–266, 1991.

N. Gillet and C. A. Jones. The quasi-geostrophic model for rapidly rotating spherical convection outside the tangent cylinder. *J. Fluid Mech.*, 554:343–370, 2006.

N. Gillet, D. Jault, E. Canet, and A. Fournier. Fast torsional waves and strong magnetic field within the Earth's core. *Nature*, 465(7294):74–77, 2010.

N. Gillet, N. Schaeffer, and D. Jault. Rationale and geophysical evidence for quasi-geostrophic rapid dynamics within the Earth's outer core. *Phys. Earth Planet. Inter.*, 202-203:78–88, 2012.

N. Gillet, D. Jault, and C. C. Finlay. Planetary gyre, time-dependent eddies, torsional waves, and equatorial jets at the Earth's core surface. *J. Geophys. Res. Solid Earth*, 120: 3991–4013, 2015.

N. Gillet, D. Jault, and E. Canet. Excitation of traveling torsional normal modes in an Earth's core model. *Geophys. J. Int.*, 210(3):1503–1516, 2017.

G. A. Glatzmaier and P. H. Roberts. A three-dimensional self-consistent computer simulation of a geomagnetic field reversal. *Nature*, 377(6546):203–209, 1995.

G. A. Glatzmaier and P. H. Roberts. Rotation and magnetism of Earth's inner core. *Science*, 274(5294):1887–1891, 1996.

H. P. Greenspan. *The Theory of Rotating Fluids*. Cambridge Monographs on Mechanics and Applied Mathematics. Cambridge University Press, 1968.

R. S. Gross. Earth rotation variations – long period. In G. Schubert, editor, *Treatise on Geophysics*, chapter 3.09, pages 215–261. Elsevier, Oxford, 2nd edition, 2015.

C. Guervilly, D. W. Hughes, and C. A. Jones. Large-scale vortices in rapidly rotating Rayleigh–Bénard convection. *J. Fluid Mech.*, 758:407–435, 2014.

E. Halley. An Account of the cause of the Change of the Variation of the Magnetical Needle; with an Hypothesis of the Structure of the Internal parts of the Earth: as it was proposed to the Royal Society in one of their late Meetings. *Philosophical Transactions*, 16(191): 563–578, 1692.

Y. He and W. Sun. Stability and convergence of the Crank-Nicolson/Adams-Bashforth scheme for the time-dependent Navier-Stokes equations. *SIAM J. Numer. Anal.*, 45(2): 837–869, 2007.

R. Hide, D. H. Boggs, and J. O. Dickey. Angular momentum fluctuations within the Earth's liquid core and torsional oscillations of the core-mantle system. *Geophys. J. Int.*, 143(3): 777–786, 2000.

K. Hirose, S. Labrosse, and J. Hernlund. Composition and state of the core. *Annu. Rev. Earth Planet. Sci.*, 41:657–691, 2013.

R. Holme. Electromagnetic core-mantle coupling - I. Explaining decadal changes in the length of day. *Geophys. J. Int.*, 132(1):167–180, 1998.

R. Holme. Large-scale flow in the core. In G. Schubert, editor, *Treatise on Geophysics*, chapter 8.04, pages 91–113. Elsevier, Oxford, 2nd edition, 2015.

R. Holme and O. de Viron. Characterization and implications of intradecadal variations in length of day. *Nature*, 499:202–205, 2013.

R. Holme and N. Olsen. Core surface flow modelling from high-resolution secular variation. *Geophys. J. Int.*, 166(2):518–528, 2006.

S. S. Hough. On the Application of Harmonic Analysis to the Dynamical Theory of the Tides. Part I. On Laplace's "Oscillations of the First Species," and on the Dynamics of Ocean Currents. *Philos. Trans. R. Soc. London, Ser. A*, 189:201–257, 1897.

Q. S. Hu and K. Skaggs. Accuracy of 6-10 day precipitation forecasts and its improvement in the past six years. In *7th NOAA annual climate prediction application science workshop*, 2009.

G. Hulot, C. C. Finlay, C. G. Constable, N. Olsen, and M. Mandea. The Magnetic Field of Planet Earth. *Space Sci. Rev.*, 152(1-4):159–222, 2010.

A. Jackson. Time-dependency of tangentially geostrophic core surface motions. *Phys. Earth Planet. Inter.*, 103(3-4):293–311, 1997.

A. Jackson, A. R. T. Jonkers, and M. R. Walker. Four centuries of geomagnetic secular variation from historical records. *Philos. Trans. R. Soc. London, Ser. A*, 358(1768):957–990, 2000.

D. Jault. Axial invariance of rapidly varying diffusionless motions in the earth's core interior. *Phys. Earth Planet. Inter.*, 166(1-2):67–76, 2008.

D. Jault and C. Finlay. Waves in the core and mechanical core-mantle interactions. In G. Schubert, editor, *Treatise on Geophysics*, chapter 8.09, pages 225–244. Elsevier, Oxford, 2nd edition, 2015.

D. Jault, C. Gire, and J.-L. Le Mouël. Westward drift, core motions and exchanges of angular momentum between core and mantle. *Nature*, 333:353–356, 1988.

H. Jeffreys. The Rigidity of the Earth's Central Core. *Geophys. J. Int.*, 1(7):371–383, 1926.

C. A. Jones. Thermal and compositional convection in the outer core. In G. Schubert, editor, *Treatise on Geophysics*, chapter 8.05, pages 115–159. Elsevier, Oxford, 2nd edition, 2015.

E. Kalnay. *Atmospheric modeling, data assimilation and predictability*. Cambridge University Press, 2003.

R. R. Kerswell and W. V. R. Malkus. Tidal instability as the source for Io's magnetic signature. *Geophys. Res. Lett.*, 25(5):603–606, 1998.

C. Kutzner and U. Christensen. Effects of driving mechanisms in geodynamo models. *Geophys. Res. Lett.*, 27(1):29–32, 2000.

F. Labbé, D. Jault, and N. Gillet. On magnetostrophic inertia-less waves in quasi-geostrophic models of planetary cores. *Geophys. Astrophys. Fluid Dyn.*, 109(6):587–610, 2015.

J. Larmor. How could a rotating body such as the sun become a magnet? *Reports of the British Association for the Advancement of Science*, 87:159–160, 1919.

M. Le Bars, D. Cébron, and P. Le Gal. Flows driven by libration, precession, and tides. *Ann. Rev. Fluid Mech.*, 47(1):163–193, 2015.

J. Li and C. B. Agee. Geochemistry of mantle-core differentiation at high pressure. *Nature*, 381(6584):686–689, 1996.

J. Li and Y. Fei. Experimental constraints on core composition. In R. Carlson, editor, *Treatise on Geochemistry*, chapter 3.15, pages 527–557. Elsevier, 2nd edition, 2014.

J. R. Lister and B. A. Buffett. The strength and efficiency of thermal and compositional convection in the geodynamo. *Phys. Earth Planet. Inter.*, 91(1-3):17–30, 1995.

P. W. Livermore, G. Ierley, and A. Jackson. The structure of Taylor's constraint in three dimensions. *Proc. R. Soc. London, Ser. A*, 464:3149–3174, 2008.

S. L. Marcus, Y. Chao, J. O. Dickey, and P. Gegout. Detection and modeling of nontidal ocean effects on Earth's rotation rate. *Science*, 281(5383):1656–1659, 1998.

P. M. Mathews, B. A. Buffett, T. A. Herring, and I. I. Shapiro. Forced nutations of the Earth: Influence of inner core dynamics: 2. Numerical results and comparisons. *J. Geophys. Res.*, 96(B5):8243–8257, 1991.

H. Matsui, E. King, and B. Buffett. Multiscale convection in a geodynamo simulation with uniform heat flux along the outer boundary. *Geochem. Geophys. Geosyst.*, 15(8):3212–3225, 2014.

S. Maus. On the applicability of the frozen flux approximation in core flow modelling as a function of temporal frequency and spatial degree. *Geophys. J. Int.*, 175(3):853–856, 2008.

W. F. McDonough. Compositional model for the Earth's core. In R. Carlson, editor, *Treatise on Geochemistry*, chapter 3.16, pages 559–577. Elsevier-Pergamon, 2nd edition, 2014.

J. X. Mitrovica, C. C. Hay, E. Morrow, R. E. Kopp, M. Dumberry, and S. Stanley. Reconciling past changes in Earth's rotation with 20th century global sea-level rise: Resolving Munk's enigma. *Sci. Adv.*, 1(11):e1500679, 2015.

H. K. Moffatt. *Magnetic Field Generation in Electrically Conducting Fluids*. Cambridge University Press, 1978.

C. More and M. Dumberry. Convectively driven decadal mean zonal accelerations in Earth's fluid core. *Submitted for publication to Geophys. J. Int.*, 2017.

L. V. Morrison and F. R. Stephenson. Historical eclipses and the variability of the Earth's rotation. *J. Geodyn.*, 32(1-2):247–265, 2001.

L. V. Morrison and C. G. Ward. An analysis of the transits of Mercury: 1677-1973. *Mon. Not. R. Astron. Soc.*, 173(1):183–206, 1975.

J. E. Mound and B. A. Buffett. Interannual oscillations in length of day: implications for the structure of the mantle and core. *J. Geophys. Res. Solid Earth*, 108(B7):2156–2202, 2003.

W. Munk and R. Revelle. On the geophysical interpretation of irregularities in the rotation of the Earth. *Geophys. J. Int.*, 6(6):331–347, 1952.

H.-C. Nataf and N. Schaeffer. Turbulence in the core. In G. Schubert, editor, *Treatise on Geophysics*, chapter 8.06, pages 161–181. Elsevier, Oxford, 2nd edition, 2015.

F. Nimmo. Energetics of the core. In G. Schubert, editor, *Treatise on Geophysics*, chapter 8.02, pages 215–261. Elsevier, Oxford, 2nd edition, 2015.

P. Olson. Core Dynamics: An Introduction and Overview. In G. Schubert, editor, *Treatise on Geophysics*, chapter 8.01, pages 1–25. Elsevier, Oxford, 2nd edition, 2015.

A. Pais and G. Hulot. Length of day decade variations, torsional oscillations and inner core superrotation: evidence from recovered core surface zonal flows. *Phys. Earth Planet. Inter.*, 118(3-4):291–316, 2000.

H. Palme, K. Lodders, and A. Jones. Solar system abundances of the elements. In R. Carlson, editor, *Treatise on Geochemistry*, chapter 2.2, pages 15–36. Elsevier, 2nd edition, 2014.

M. Pozzo, C. Davies, D. Gubbins, and D. Alfè. Thermal and electrical conductivity of iron at Earth's core conditions. *Nature*, 485(7398):355–358, 2012.

T. Pratchett. *The Light Fantastic*. Number 2 in The Discworld Series. Colin Smythe, 1986.

W. H. Press, S. A. Teukolsky, W. T. Vetterling, and B. P. Flannery. *Numerical Recipes in Fortran*. Cambridge University Press, 2nd edition, 1992.

J. Proudman. On the motion of solids in a liquid possessing vorticity. *Proc. R. Soc. London, Ser. A*, 92(642):408–424, 1916.

L. Rayleigh. On convection currents in a horizontal layer of fluid, when the higher temperature is on the under side. *Philosophical Magazine*, 32(192):529–546, 1916.

A. E. Ringwood. The Bakerian Lecture, 1983: The Earth's Core: Its Composition, Formation and Bearing Upon the Origin of the Earth. *Proc. R. Soc. London, Ser. A*, 395(1808):1–46, 1984.

P. H. Roberts. Theory of the geodynamo. In G. Schubert, editor, *Treatise on Geophysics*, chapter 8.03, pages 57–90. Elsevier, Oxford, 2nd edition, 2015.

P. H. Roberts and E. M. King. On the genesis of the Earth's magnetism. *Rep. Prog. Phys.*, 76(9):096801, 2013.

P. H. Roberts and S. Scott. On analysis of the secular variation. *J. Geomagn. Geoelec.*, 17 (2):137–151, 1965.

R. D. Rosen and D. A. Salstein. Comment on "A seasonal budget of the Earth's axial angular momentum" by Naito and Kikuchi. *Geophys. Res. Lett.*, 18(10):1925–1926, 1991.

J. Rotvig and C. A. Jones. Rotating convection-driven dynamos at low Ekman number. *Phys. Rev. E: Stat. Nonlinear Soft Matter Phys.*, 66(5):056308, 2002.

N. Schaeffer and P. Cardin. Quasigeostrophic model of the instabilities of the Stewartson layer in flat and depth-varying containers. *Phys. Fluids*, 17:104111, 2005.

N. Schaeffer, D. Jault, H.-C. Nataf, and A. Fournier. Turbulent geodynamo simulations: a leap towards Earth's core. *Geophys. J. Int.*, 211(1):1–29, 2017.

A. Souriau and M. Calvet. Deep Earth Structure: The Earth's Cores. In G. Schubert, editor, *Treatise on Geophysics*, chapter 1.23, pages 725–757. Elsevier, Oxford, 2nd edition, 2015.

S. Stellmach, M. Lischper, K. Julien, G. Vasil, J. S. Cheng, A. Ribeiro, E. M. King, and J. M. Aurnou. Approaching the asymptotic regime of rapidly rotating convection: boundary layers versus interior dynamics. *Phys. Rev. Lett.*, 113:254501, 2014.

F. R. Stephenson and L. V. Morrison. Long-term fluctuations in the Earth's rotation: 700 BC to AD 1990. *Philos. Trans. R. Soc. London, Ser. A*, 351(1695):165–202, 1995.

M. Stix and P. H. Roberts. Time-dependent electromagnetic core-mantle coupling. *Phys. Earth Planet. Inter.*, 36(1):49–60, 1984.

L. Stixrude and R. Jeanloz. Constraints on Seismic Models from Other Disciplines - Constraints from Mineral Physics on Seismological Models. In G. Schubert, editor, *Treatise on Geophysics*, chapter 1.26, pages 829–852. Elsevier, Oxford, 2nd edition, 2015.

F. Takahashi, M. Matsushima, and Y. Honkura. Scale variability in convection-driven MHD dynamos at low Ekman number. *Phys. Earth Planet. Inter.*, 167:168–178, 2008.

G. I. Taylor. Motion of solids in fluids when the flow is not irrotational. *Proc. R. Soc. London, Ser. A*, 93(648):99–113, 1917.

J. B. Taylor. The magneto-hydrodynamics of a rotating fluid and the Earth's dynamo problem. *Proc. R. Soc. London, Ser. A*, 274(1357):274–283, 1963.

R. J. Teed, C. A. Jones, and S. M. Tobias. The dynamics and excitation of torsional waves in geodynamo simulations. *Geophys. J. Int.*, 196(2):724–735, 2014.

R. J. Teed, C. A. Jones, and S. M. Tobias. The transition to Earth-like torsional oscillations in magnetoconvection simulations. *Earth Planet. Sci. Lett.*, 419:22–31, 2015.

E. H. Vestine. On variations of the geomagnetic field, fluid motions, and the rate of the Earth's rotation. *J. Geophys. Res.*, 58(2):127–145, 1953.

E. H. Vestine and A. B. Kahle. The westward drift and geomagnetic secular change. *Geophys. J. R. Astron. Soc.*, 15(1-2):29–37, 1968.

M. Walker, S. Johnsen, S. O. Rasmussen, T. Popp, J. P. Steffensen, P. Gibbard, W. Hoek, J. Lowe, J. Andrews, S. Björk, L. C. Cwynar, K. Hughen, P. Kershaw, B. Kromer, T. Litt,

D. J. Lowe, T. Nakagawa, R. Newnham, and J. Schwander. Formal definition and dating of the GSSP (Global Stratotype Section and Point) for the base of the Holocene using the Greenland NGRIP ice core, and selected auxiliary records. *J. Quat. Sci.*, 24(1):3–17, 2009.

H. Wänke and G. Dreibus. Chemical composition and accretion history of terrestrial planets. *Philos. Trans. R. Soc. London, Ser. A*, 325(1587):545–557, 1988.

J. T. Wasson and G. W. Kallemeyn. Composition of chondrites. *Philos. Trans. R. Soc. London, Ser. A*, 325(1587):535–544, 1988.

K. A. Whaler. Geomagnetic evidence for fluid upwelling at the core-mantle boundary. *Geophys. J. Int.*, 86(2):563–588, 1986.

J. Wicht and U. R. Christensen. Torsional oscillations in dynamo simulations. *Geophys. J. Int.*, 181(3):1367–1380, 2010.

C.-C. Wu and P. H. Roberts. On magnetostrophic mean-field solutions of the geodynamo equations. *Geophys. Astrophys. Fluid Dyn.*, 109:84–110, 2015.

R. K. Yadav, T. Gastine, U. R. Christensen, S. J. Wolk, and K. Poppenhaeger. Approaching a realistic force balance in geodynamo simulations. *PNAS*, 113(43):12065–12070, 2016.

S. Zatman and J. Bloxham. Torsional oscillations and the magnetic field within the Earth's core. *Nature*, 388(6644):760–763, 1997.

Appendix A

Useful Mathematical Relations

This appendix assumes a cylindrical coordinate system (s, ϕ, z), with its $\mathbf{e}_z$-axis aligned with the axis of rotation. In a spherical container, the distance in the axial direction from the equatorial plane to either the upper or lower boundary is the same, being

$$L = \sqrt{1 - s^2}\,, \tag{A.1}$$

with

$$\beta = \frac{1}{L}\frac{\partial L}{\partial s} = -\frac{s}{L^2}\,. \tag{A.2}$$

The radial derivatives of L and β are

$$\frac{\partial L}{\partial s} = -\frac{s}{L} = L\beta, \quad \frac{\partial^2 L}{\partial s^2} = -\frac{1}{L^3}\,, \tag{A.3}$$

$$\frac{\partial \beta}{\partial s} = -\frac{1 + s^2}{L^4}\,. \tag{A.4}$$

A.1 Gradient Operator

The gradient operator in cylindrical (s, ϕ, z) coordinates is

$$\boldsymbol{\nabla} = \mathbf{e}_s \frac{\partial}{\partial s} + \frac{\mathbf{e}_\phi}{s} \frac{\partial}{\partial \phi} + \mathbf{e}_z \frac{\partial}{\partial z} \,. \tag{A.5}$$

So, for a scalar function f and vector functions $\mathbf{F}$ and $\mathbf{G}$,

$$\boldsymbol{\nabla} f = \left(\mathbf{e}_s \frac{\partial}{\partial s} + \mathbf{e}_\phi \frac{1}{s} \frac{\partial}{\partial \phi} + \mathbf{e}_z \frac{\partial}{\partial z} \right) f \tag{A.6}$$

$$\boldsymbol{\nabla} \cdot \mathbf{F} = \frac{1}{s} \frac{\partial}{\partial s} (s F_s) + \frac{1}{s} \frac{\partial}{\partial \phi} F_\phi + \frac{\partial}{\partial z} F_z \tag{A.7}$$

$$\begin{aligned} \boldsymbol{\nabla} \times \mathbf{F} = \; & \mathbf{e}_s \left(\frac{1}{s} \frac{\partial}{\partial \phi} F_z - \frac{\partial}{\partial z} F_\phi \right) \\ & + \mathbf{e}_\phi \left(\frac{\partial}{\partial z} F_s - \frac{\partial}{\partial s} F_z \right) \\ & + \mathbf{e}_z \frac{1}{s} \left(\frac{\partial}{\partial s} (s F_\phi) - \frac{\partial}{\partial \phi} F_s \right) \end{aligned} \tag{A.8}$$

$$\nabla^2 f = \left(\frac{\partial^2}{\partial s^2} + \frac{1}{s} \frac{\partial}{\partial s} + \frac{1}{s^2} \frac{\partial^2}{\partial \phi^2} + \frac{\partial^2}{\partial z^2} \right) f \tag{A.9}$$

$$\begin{aligned} \nabla^2 \mathbf{F} = \; & \mathbf{e}_s \left(\nabla^2 F_s - \frac{F_s}{s^2} - \frac{2}{s^2} \frac{\partial}{\partial \phi} F_\phi \right) \\ & + \mathbf{e}_\phi \left(\nabla^2 F_\phi - \frac{F_\phi}{s^2} + \frac{2}{s^2} \frac{\partial}{\partial \phi} F_s \right) \\ & + \mathbf{e}_z \nabla^2 F_z \end{aligned} \tag{A.10}$$

$$\begin{aligned} (\mathbf{F} \cdot \boldsymbol{\nabla}) \, \mathbf{G} = \; & \mathbf{e}_s \left(F_s \frac{\partial}{\partial s} G_s + \frac{A_\phi}{s} \frac{\partial}{\partial \phi} G_s + F_z \frac{\partial}{\partial z} G_s - \frac{F_\phi G_\phi}{s} \right) \\ & + \mathbf{e}_\phi \left(F_s \frac{\partial}{\partial s} G_\phi + \frac{A_\phi}{s} \frac{\partial}{\partial \phi} G_\phi + F_z \frac{\partial}{\partial z} G_\phi + \frac{F_\phi G_s}{s} \right) \\ & + \mathbf{e}_z \left(F_s \frac{\partial}{\partial s} G_z + \frac{F_\phi}{s} \frac{\partial}{\partial \phi} F_z + F_z \frac{\partial}{\partial z} G_z \right) \end{aligned} \tag{A.11}$$

It will often be the case that only the horizontal (s, ϕ) components of these operators will be needed. In particular, if $\boldsymbol{\nabla}_H \equiv \boldsymbol{\nabla}_{s,\phi}$,

$$\boldsymbol{\nabla}_H f = \left(\mathbf{e}_s \frac{\partial}{\partial s} + \mathbf{e}_\phi \frac{1}{s} \frac{\partial}{\partial \phi} \right) f \tag{A.12}$$

$$\nabla_H^2 f = \left(\frac{\partial^2}{\partial s^2} + \frac{1}{s} \frac{\partial}{\partial s} + \frac{1}{s^2} \frac{\partial^2}{\partial \phi^2} \right) f \tag{A.13}$$

A.2 Cylindrically Radial Derivatives

For an arbitrary function f and integers (m, n), the following may be shown to be equivalent. The conversion of linear (f) to angular $\left(\frac{f}{s}\right)$ derivatives is inferred from calculating the $n = 1, 2, 3, 4$ cases, and inferring that the pattern will continue.

$$\frac{1}{s^n L^m} \frac{\partial}{\partial s} \left(s^n L^m f \right) = \left(\frac{\partial}{\partial s} + \frac{n}{s} + m\beta \right) f \tag{A.14}$$

$$\frac{1}{s^n} \frac{\partial^2}{\partial s^2} \left(s^n f \right) = \left(\frac{\partial^2}{\partial s^2} + \frac{2n}{s} \frac{\partial}{\partial s} + \frac{n\left(n-1\right)}{s^2} \right) f \tag{A.15}$$

$$\frac{\partial^n}{\partial s^n} f = s \left(\frac{\partial^n}{\partial s^n} + \frac{n}{s} \frac{\partial^{n-1}}{\partial s^{n-1}} \right) \left(\frac{f}{s} \right) . \tag{A.16}$$

A.3 Azimuthal Averaging

The average of a function f in the $\mathbf{e}_\phi$-direction is denoted with an overbar:

$$\overline{f} = \frac{1}{2\pi s} \int_0^{2\pi} f(t, s, \phi, z) s \, \mathrm{d}\phi = \frac{1}{2\pi} \int_0^{2\pi} f(t, s, \phi, z) \, \mathrm{d}\phi \tag{A.17}$$

Because all the fields we deal with are continuous in ϕ, azimuthally averaging the Laplace operator removes the $\mathbf{e}_\phi$-component:

$$\overline{\nabla^2 f} = \overline{\nabla_s^2 f} + \overline{\nabla_z^2 f} + \overline{\nabla_\phi^2 f} \tag{A.18}$$

$$= \left(\nabla_s^2 + \nabla_z^2\right) \overline{f} + \overline{\frac{1}{s^2}\frac{\partial^2}{\partial \phi^2} f} \tag{A.19}$$

$$= \nabla_{s,z}^2 \overline{f} + \frac{1}{2\pi s^2} \left.\frac{\partial}{\partial \phi} f\right|_0^{2\pi} \tag{A.20}$$

$$\Rightarrow \overline{\nabla^2 f} = \nabla_{s,z}^2 \overline{f} \tag{A.21}$$

The azimuthal average of the vector Laplacian operator is slightly more complicated:

$$\overline{\boldsymbol{\nabla}^2 f} = \overline{\boldsymbol{\nabla}_s^2 f} + \overline{\boldsymbol{\nabla}_z^2 f} + \overline{\boldsymbol{\nabla}_\phi^2 f} \tag{A.22}$$

$$= \left(\overline{\nabla^2 f_s - \frac{f_s}{s^2} - \frac{2}{s^2}\frac{\partial f_\phi}{\partial \phi}}\right) \mathbf{e}_s + \left(\overline{\nabla^2 f_\phi - \frac{f_\phi}{s^2} + \frac{2}{s^2}\frac{\partial f_s}{\partial \phi}}\right) \mathbf{e}_\phi + \left(\overline{\nabla^2 f_z}\right) \mathbf{e}_z \tag{A.23}$$

$$= \left(\nabla_{s,z}^2 \overline{f_s} - \frac{\overline{f_s}}{s^2} - \frac{1}{\pi s^2}\, f_\phi|_0^{2\pi}\right) \mathbf{e}_s + \left(\nabla_{s,z}^2 \overline{f_\phi} - \frac{\overline{f_\phi}}{s^2} + \frac{1}{\pi s^2}\, f_s|_0^{2\pi}\right) \mathbf{e}_\phi + \left(\nabla_{s,z}^2 \overline{f_z}\right) \mathbf{e}_z \tag{A.24}$$

$$\Rightarrow \overline{\boldsymbol{\nabla}^2 f} = \mathbf{e}_s \left(\nabla_{s,z}^2 - \frac{1}{s^2}\right) \overline{f_s} + \mathbf{e}_\phi \left(\nabla_{s,z}^2 - \frac{1}{s^2}\right) \overline{f_\phi} + \mathbf{e}_z \nabla_{s,z}^2 \overline{f_z} \tag{A.25}$$

A.4 Axial Averaging

The average of a function f in the $\mathbf{e}_z$-direction between boundaries at $z = a$ and $z = b$ is denoted with angled brackets:

$$\langle f \rangle = \frac{1}{b-a} \int_a^b f(t, s, \phi, z)\, \mathrm{d}z\,. \tag{A.26}$$

The spherical container which defines the boundaries of our system is symmetric across the equatorial plane. Therefore, with $L \equiv \sqrt{1 - s^2}$, $b = -a = L$:

$$\langle f \rangle_{\text{spherical}} = \frac{1}{2L} \int_{-L}^{L} f(t, s, \phi, z)\, \mathrm{d}z\,. \tag{A.27}$$

If $f(t, s, \phi, z)$ is also symmetric across the equator, Eq.(A.27) simplifies to

$$\langle f \rangle_{\text{fully symmetric}} = \frac{1}{L} \int_0^L f(t, s, \phi, z) \, \mathrm{d}z \, . \tag{A.28}$$

A.4.1 First Radial Derivative

Because the position of the boundaries a and b may change with radius, care must be taken when taking the axial average of a function involving a radial derivative. According to the Leibniz integral rule,

$$\frac{\partial}{\partial s} \int_a^b f \, \mathrm{d}z = \int_a^b \frac{\partial}{\partial s} f \, \mathrm{d}z + f|_{z=b} \frac{\partial b}{\partial s} - f|_{z=a} \frac{\partial a}{\partial s} \, . \tag{A.29}$$

Applying this theorem to the radial derivative of a function's axial average,

$$\frac{\partial}{\partial s} \langle f \rangle = \frac{\partial}{\partial s} \left(\frac{1}{b-a} \int_a^b f \, \mathrm{d}z \right) \tag{A.30}$$

$$= \frac{\partial}{\partial s} \left(\frac{1}{b-a} \right) \left(\int_a^b f \, \mathrm{d}z \right) + \left(\frac{1}{b-a} \right) \left(\frac{\partial}{\partial s} \int_a^b f \, \mathrm{d}z \right) \tag{A.31}$$

$$= -\frac{\frac{\partial}{\partial s}(b-a)}{(b-a)^2} \int_a^b f \, \mathrm{d}z + \left(\frac{1}{b-a} \right) \left(\int_a^b \frac{\partial}{\partial s} f \, \mathrm{d}z + \frac{\partial b}{\partial s} f|_{z=b} - \frac{\partial a}{\partial s} f|_{z=a} \right) \tag{A.32}$$

$$= -\frac{\frac{\partial}{\partial s}(b-a)}{b-a} \langle f \rangle + \left\langle \frac{\partial}{\partial s} f \right\rangle + \frac{1}{b-a} \left(\frac{\partial b}{\partial s} f|_{z=b} - \frac{\partial a}{\partial s} f|_{z=a} \right) \tag{A.33}$$

$$\boxed{\Rightarrow \left\langle \frac{\partial}{\partial s} f \right\rangle = \frac{\partial}{\partial s} \langle f \rangle + \frac{1}{b-a} \left(\frac{\partial b}{\partial s} \left(\langle f \rangle - f|_{z=b} \right) - \frac{\partial a}{\partial s} \left(\langle f \rangle - f|_{z=a} \right) \right) \, .} \tag{A.34}$$

Eq.(A.34) can be simplified by placing various assumptions on the form of f, a, and b:

Spherical Geometry, $b = -a = L$**:**

$$\left\langle \frac{\partial}{\partial s} f \right\rangle = \frac{\partial}{\partial s} \langle f \rangle + \beta \left(\langle f \rangle - \frac{1}{2} \left(f|_{z=L} + f|_{z=-L} \right) \right) \tag{A.35}$$

Symmetric, $f|_{z=L} = f|_{z=-L}$**:**

$$= \frac{\partial}{\partial s} \langle f \rangle + \beta \left(\langle f \rangle - f|_{z=L} \right) \tag{A.36}$$

Antisymmetric, $f|_{z=L} = -f|_{z=-L}$**:**

$$= \left(\frac{\partial}{\partial s} + \beta \right) \langle f \rangle \tag{A.37}$$

Rigid, $f|_{z=L} = f|_{z=-L} = \langle f \rangle$**:**

$$= \frac{\partial}{\partial s} \langle f \rangle \tag{A.38}$$

Axial Average of the First Radial Derivative

Second Radial Derivative

Using the same approach as for the axial average of the first derivative,

$$\frac{\partial^2}{\partial s^2} \langle f \rangle = \frac{\partial}{\partial s} \left(\frac{\partial}{\partial s} \langle f \rangle \right) = \frac{\partial}{\partial s} \left(\frac{\partial}{\partial s} \left(\frac{1}{b-a} \int_a^b f \, \mathrm{d}z \right) \right) \tag{A.39}$$

$$= \frac{\partial}{\partial s} \left(\frac{\partial}{\partial s} \left(\frac{1}{b-a} \right) \int_a^b f \, \mathrm{d}z + \frac{1}{b-a} \frac{\partial}{\partial s} \int_a^b f \, \mathrm{d}z \right) \tag{A.40}$$

$$= \underbrace{\frac{\partial^2}{\partial s^2} \left(\frac{1}{b-a} \right) \int_a^b f \, \mathrm{d}z}_{①} + \underbrace{2 \frac{\partial}{\partial s} \left(\frac{1}{b-a} \right) \frac{\partial}{\partial s} \int_a^b f \, \mathrm{d}z}_{②} + \underbrace{\frac{1}{b-a} \frac{\partial}{\partial s} \left(\frac{\partial}{\partial s} \int_a^b f \, \mathrm{d}z \right)}_{③} . \tag{A.41}$$

The first term becomes

$$① = -\frac{1}{b-a}\left(\frac{\partial^2}{\partial s^2}(b-a) - 2\frac{\left(\frac{\partial}{\partial s}(b-a)\right)^2}{b-a}\right)\langle f\rangle \ . \tag{A.42}$$

The second term becomes

$$② = 2\left(\frac{\partial}{\partial s}\left(\frac{1}{b-a}\right)\right)\frac{\partial}{\partial s}\int_a^b f\,\mathrm{d}z \tag{A.43}$$

$$= 2\left(-\frac{1}{(b-a)^2}\frac{\partial}{\partial s}(b-a)\right)\frac{\partial}{\partial s}\left(\frac{b-a}{b-a}\int_a^b f\,\mathrm{d}z\right) \tag{A.44}$$

$$= -\left(\frac{2}{(b-a)^2}\frac{\partial}{\partial s}(b-a)\right)\frac{\partial}{\partial s}\left((b-a)\langle f\rangle\right) \tag{A.45}$$

$$= -\left(\frac{2}{(b-a)^2}\frac{\partial}{\partial s}(b-a)\right)\left(\frac{\partial}{\partial s}(b-a)\langle f\rangle + (b-a)\frac{\partial}{\partial s}\langle f\rangle\right) \tag{A.46}$$

$$② = -\frac{1}{b-a}\left(2\frac{\left(\frac{\partial}{\partial s}(b-a)\right)^2}{b-a} + 2\frac{\partial}{\partial s}(b-a)\frac{\partial}{\partial s}\right)\langle f\rangle \ . \tag{A.47}$$

We now have

$$① + ② = -\frac{1}{b-a}\left(\underbrace{\frac{\partial^2}{\partial s^2}(b-a) - 2\frac{\left(\frac{\partial}{\partial s}(b-a)\right)^2}{b-a}}_{①} + \underbrace{2\frac{\left(\frac{\partial}{\partial s}(b-a)\right)^2}{b-a} + 2\frac{\partial}{\partial s}(b-a)\frac{\partial}{\partial s}}_{②}\right)\langle f\rangle \tag{A.48}$$

$$① + ② = -\frac{1}{b-a}\left(\frac{\partial^2}{\partial s^2}(b-a) + 2\frac{\partial}{\partial s}(b-a)\frac{\partial}{\partial s}\right)\langle f\rangle \ . \tag{A.49}$$

Finally, term ③ becomes

$$
\begin{aligned}
③ =& \frac{1}{b-a}\frac{\partial}{\partial s}\left(\int_a^b \frac{\partial f}{\partial s}\,\mathrm{d}z + \frac{\partial b}{\partial s}\,f|_{z=b} - \frac{\partial a}{\partial s}\,f|_{z=a}\right) && \text{(A.50)}\\
=& \frac{1}{b-a}\int_a^b \frac{\partial^2 f}{\partial s^2}\,\mathrm{d}z \\
&+ \frac{1}{b-a}\left(\frac{\partial b}{\partial s}\,\frac{\partial f}{\partial s}\bigg|_{z=b} - \frac{\partial a}{\partial s}\,\frac{\partial f}{\partial s}\bigg|_{z=a} + \frac{\partial b}{\partial s}\frac{\partial}{\partial s}\left(f|_{z=b}\right) - \frac{\partial a}{\partial s}\left(\frac{\partial}{\partial s}\,f|_{z=a}\right)\right) \\
&+ \frac{1}{b-a}\left(\frac{\partial^2 b}{\partial s^2}\,f|_{z=b} - \frac{\partial^2 a}{\partial s^2}\,f|_{z=a}\right). && \text{(A.51)}
\end{aligned}
$$

Combining Eqs.(A.41), A.49 and A.51, factoring terms of similar boundary derivative order, and solving for $\left\langle \frac{\partial^2 f}{\partial s^2} \right\rangle$, I get

$$
\begin{aligned}
\left\langle \frac{\partial^2 f}{\partial s^2} \right\rangle =& \frac{\partial^2}{\partial s^2}\left\langle f \right\rangle \\
&+ \frac{1}{b-a}\left(\frac{\partial^2 b}{\partial s^2}\left(\left\langle f \right\rangle - f|_{z=b}\right) - \frac{\partial^2 a}{\partial s^2}\left(\left\langle f \right\rangle - f|_{z=a}\right)\right) \\
&+ \frac{1}{b-a}\left(\frac{\partial b}{\partial s}\left(2\frac{\partial}{\partial s}\left\langle f \right\rangle - \frac{\partial}{\partial s}\left(f|_{z=b}\right) - \frac{\partial f}{\partial s}\bigg|_{z=b}\right)\right) \\
&- \frac{1}{b-a}\left(\frac{\partial a}{\partial s}\left(2\frac{\partial}{\partial s}\left\langle f \right\rangle - \frac{\partial}{\partial s}\left(f|_{z=a}\right) - \frac{\partial f}{\partial s}\bigg|_{z=a}\right)\right)
\end{aligned}
\qquad \text{(A.52)}
$$

Similar to the case of the single radial derivative, Eq.(A.52) can be simplified with various assumptions on the system's geometry and the symmetry of the field being averaged:

Spherical Geometry, $b = -a = L$**:**

$$\left\langle \frac{\partial^2 f}{\partial s^2} \right\rangle = \frac{\partial^2}{\partial s^2} \langle f \rangle - \frac{1}{2L^4} \left(2 \langle f \rangle - f|_{z=L} - f|_{z=-L} \right) + \frac{\beta}{2} \left(4 \frac{\partial}{\partial s} \langle f \rangle - \frac{\partial}{\partial s} \left(f|_{z=L} \right) - \frac{\partial}{\partial s} \left(f|_{z=-L} \right) - \left. \frac{\partial f}{\partial s} \right|_{z=L} - \left. \frac{\partial f}{\partial s} \right|_{z=-L} \right) \tag{A.53}$$

Symmetric, $f|_{z=L} = f|_{z=-L}$, $\left. \frac{\partial f}{\partial s} \right|_{z=L} = \left. \frac{\partial f}{\partial s} \right|_{z=-L}$**:**

$$= \frac{\partial^2}{\partial s^2} \langle f \rangle - \frac{1}{L^4} \left(\langle f \rangle - f|_{z=L} \right) + \beta \left(2 \frac{\partial}{\partial s} \langle f \rangle - \frac{\partial}{\partial s} \left(f|_{z=L} \right) - \left. \frac{\partial f}{\partial s} \right|_{z=L} \right) \tag{A.54}$$

Antisymmetric, $f|_{z=L} = -f|_{z=-L}$, $\left. \frac{\partial f}{\partial s} \right|_{z=L} = -\left. \frac{\partial f}{\partial s} \right|_{z=-L}$**:**

$$= \frac{\partial^2}{\partial s^2} \langle f \rangle - \left(\frac{1}{L^4} - 2\beta \frac{\partial}{\partial s} \right) \langle f \rangle \tag{A.55}$$

Rigid, $f|_{z=L} = f|_{z=-L} = \langle f \rangle$, $\left. \frac{\partial f}{\partial s} \right|_{z=L} = \left. \frac{\partial f}{\partial s} \right|_{z=-L} = \frac{\partial \langle f \rangle}{\partial s}$**:**

$$= \frac{\partial^2}{\partial s^2} \langle f \rangle \tag{A.56}$$

Axial Average of the Second Radial Derivative

Scalar Laplace Operator

Using the axial averaging operators derived in the previous section allows us to calculate the form of the axially-averaged Laplace operator. Assuming the case of spherical geometry, but with no assumptions on the form of the function f being operated on,

$$\left\langle \nabla^2 f \right\rangle = \frac{1}{2L}\int_{-L}^{L} \nabla^2 f \,\mathrm{d}z \tag{A.57}$$

$$= \frac{1}{2L}\int_{-L}^{L} \left(\frac{\partial^2 f}{\partial s^2} + \frac{1}{s}\frac{\partial f}{\partial s} + \frac{1}{s^2}\frac{\partial^2 f}{\partial \phi^2} + \frac{\partial^2 f}{\partial z} \right) \mathrm{d}z \tag{A.58}$$

$$= \left\langle \frac{\partial^2 f}{\partial s^2} \right\rangle + \frac{1}{s}\left\langle \frac{\partial f}{\partial s} \right\rangle + \frac{1}{s^2}\frac{\partial^2}{\partial \phi^2}\left\langle f \right\rangle + \frac{1}{2L}\left.\frac{\partial f}{\partial z}\right|_{-L}^{L} \tag{A.59}$$

In general, $f = f(t, s, \phi, z)$. However, to save space, I shall use $f(a) \equiv f|_{z=a}$ and $F|_a \equiv F|_{z=a}$ (for some function or operator F) for the rest of this section. Substituting the expansions of $\left\langle \frac{\partial f}{\partial s} \right\rangle$ and $\left\langle \frac{\partial^2 f}{\partial s^2} \right\rangle$ from Eqs.(A.35) and (A.53), respectively, results in

$$\begin{aligned}
\left\langle \nabla^2 f \right\rangle = &\left[\frac{\partial^2}{\partial s^2}\left\langle f \right\rangle - \frac{1}{2L^4}\left(2\left\langle f \right\rangle - f(L) - f(-L)\right) \right. \\
&\left. + \frac{\beta}{2}\left(4\frac{\partial}{\partial s}\left\langle f \right\rangle - \frac{\partial}{\partial s}f(L) - \frac{\partial}{\partial s}f(-L) - \left.\frac{\partial f}{\partial s}\right|_{L} - \left.\frac{\partial f}{\partial s}\right|_{-L} \right) \right] \\
&+ \frac{1}{s}\left[\frac{\partial}{\partial s}\left\langle f \right\rangle + \beta\left(\left\langle f \right\rangle - \frac{1}{2}\left(f(L) + f(-L)\right) \right) \right] \\
&+ \frac{1}{s^2}\frac{\partial^2}{\partial \phi^2}\left\langle f \right\rangle + \frac{1}{2L}\left.\frac{\partial f}{\partial z}\right|_{-L}^{L}
\end{aligned} \tag{A.60}$$

$$\begin{aligned}
= &\left(\left(\frac{\partial^2}{\partial s^2} + \frac{1}{s}\frac{\partial}{\partial s} + \frac{1}{s^2}\frac{\partial^2}{\partial \phi^2} \right)\left\langle f \right\rangle + \frac{1}{2L}\left.\frac{\partial f}{\partial z}\right|_{-L}^{L} \right) \\
&+ \left(\beta\frac{\partial}{\partial s} + \frac{\beta}{s} - \frac{1}{L^4} \right)\left(\left\langle f \right\rangle - \frac{1}{2}\left(f(L) + f(-L)\right) \right) \\
&+ \beta\left(\frac{\partial}{\partial s}\left\langle f \right\rangle - \frac{1}{2}\left(\left.\frac{\partial f}{\partial s}\right|_{L} + \left.\frac{\partial f}{\partial s}\right|_{-L} \right) \right)
\end{aligned} \tag{A.61}$$

$$\boxed{\begin{aligned}
\left\langle \nabla^2 f \right\rangle = &\left(\nabla_{s,\phi}^2\left\langle f \right\rangle + \frac{1}{2L}\left.\frac{\partial f}{\partial z}\right|_{-L}^{L} \right) \\
&+ \beta\left(\frac{\partial}{\partial s} + \frac{1}{s} + \frac{1}{sL^2} \right)\left(\left\langle f \right\rangle - \frac{1}{2}\left(f(L) + f(-L)\right) \right) \\
&+ \beta\left(\frac{\partial}{\partial s}\left\langle f \right\rangle - \frac{1}{2}\left(\left.\frac{\partial f}{\partial s}\right|_{L} + \left.\frac{\partial f}{\partial s}\right|_{-L} \right) \right)
\end{aligned}} \tag{A.62}$$

As usual, this can be simplified for various symmetries:

Symmetric, $f(L) = f(-L)$, $\left.\frac{\partial f}{\partial s}\right|_L = \left.\frac{\partial f}{\partial s}\right|_{-L}$, $\left.\frac{\partial f}{\partial z}\right|_L = -\left.\frac{\partial f}{\partial z}\right|_{-L}$**:**

$$\begin{aligned}\left\langle \nabla^2 f \right\rangle =& \nabla^2_{s,\phi} \langle f \rangle + \beta \left(\frac{\partial}{\partial s} + \frac{1}{s} + \frac{1}{sL^2} \right) (\langle f \rangle - f(L)) \\ &+ \beta \left(\frac{\partial}{\partial s} \langle f \rangle - \left.\frac{\partial f}{\partial s}\right|_L \right) + \frac{1}{L} \left.\frac{\partial f}{\partial z}\right|_L \end{aligned} \tag{A.63}$$

Antisymmetric, $f(L) = -f(-L)$, $\left.\frac{\partial f}{\partial s}\right|_L = -\left.\frac{\partial f}{\partial s}\right|_{-L}$, $\left.\frac{\partial f}{\partial z}\right|_L = \left.\frac{\partial f}{\partial z}\right|_{-L}$**:**

$$= \nabla^2_{s,\phi} \langle f \rangle + \beta \left(2\frac{\partial}{\partial s} + \frac{1}{s} + \frac{1}{sL^2} \right) \langle f \rangle \tag{A.64}$$

Rigid, $f(L) = f(-L) = \langle f \rangle$, $\left.\frac{\partial f}{\partial s}\right|_L = \left.\frac{\partial f}{\partial s}\right|_{-L} = \frac{\partial}{\partial s}\langle f \rangle$, $\frac{\partial f}{\partial z} = 0$**:**

$$= \nabla^2_{s,\phi} \langle f \rangle \tag{A.65}$$

Axial Average of the Laplacian Operator

The vector Laplace operator only contains radial derivatives within scalar Laplace operators, so it is easily adapted to a vertically averaged form.

A.5 Azimuthal Average of Two Real-Valued Functions

If f can be represented by a Fourier series, complex-valued constants a_m may be chosen such that

$$f = \sum_{m=-\infty}^{+\infty} a_m e^{im\phi}. \tag{A.66}$$

However, if f is purely real, $f = f^*$ (where f^* is the complex conjugate of f),

$$\sum_{-\infty}^{\infty} a_m e^{im\phi} = \sum_{-\infty}^{\infty} a_m^* e^{-im\phi} = \sum_{-\infty}^{\infty} a_{-m}^* e^{im\phi}\,, \tag{A.67}$$

and therefore

$$a_m = a_{-m}^*\,. \tag{A.68}$$

The azimuthally averaged product of two such purely real functions, f and g (with constants a_m and b_n, respectively), is

$$\overline{fg} = \frac{1}{2\pi s}\oint_0^{2\pi}\left[\left(\sum_{-\infty}^{\infty} a_m e^{im\phi}\right)\left(\sum_{-\infty}^{\infty} b_n e^{in\phi}\right)\right] s\,\mathrm{d}\phi \tag{A.69}$$

$$= \sum_{-\infty}^{\infty}\sum_{-\infty}^{\infty}\frac{a_m b_n}{2\pi s}\oint_0^{2\pi} e^{(m+n)\phi}\,\mathrm{d}\phi = \sum_{-\infty}^{\infty}\sum_{-\infty}^{\infty} a_m b_n \delta_{-nm} \tag{A.70}$$

$$= \sum_{-\infty}^{\infty} a_m b_{-m}\,. \tag{A.71}$$

Relabelling, and using Eq.(A.68),

$$\overline{fg} = \sum_{-\infty}^{\infty} a_m b_{-m} = \sum_{-\infty}^{-1} a_m b_{-m} + a_0 b_0 + \sum_{m=1}^{\infty} a_m b_{-m} \tag{A.72}$$

$$= a_0 b_0 + \sum_{m=1}^{\infty}\left(a_{-m} b_m + a_m b_{-m}\right) \tag{A.73}$$

$$= a_0 b_0 + \sum_{m=1}^{\infty}\left(a_m^* b_m + a_m b_m^*\right) \tag{A.74}$$

Letting $a_m = a + bi$ and $b_m = c + di$, for $\{a, b, c, d\} \in \mathbb{R}$,

$$a_m^* b_m + a_m b_m^* = (a - bi)(c + di) + (a + bi)(c - di) \tag{A.75}$$

$$= (ac + bd) + (ad - bc)\, i + (ac + bd) - (ad - bc)\, i \tag{A.76}$$

$$= 2(ac + bd) \tag{A.77}$$

$$= 2\left[\Re(a_m)\,\Re(b_m) + \Im(a_m)\,\Im(b_m)\right]. \tag{A.78}$$

This allows Eq.(A.74) to be written in terms of the real and imaginary parts of the Fourier coefficients:

$$\boxed{\overline{fg} = a_0 b_0 + 2\sum_{m=1}^{\infty}\left[\Re(a_m)\,\Re(b_m) + \Im(a_m)\,\Im(b_m)\right] \text{ if } \{f, g\} \in \mathbb{R}\,.} \tag{A.79}$$

Appendix B

Dimensional Governing Equations

B.1 Governing Equations

The motions of fluids in which density variations only matter for buoyancy forces can be approximated by the Navier-Stokes equation under the Boussinesq approximation:

$$\frac{\partial \mathbf{u}'}{\partial t'} + (\mathbf{u}' \cdot \boldsymbol{\nabla}')\,\mathbf{u}' + 2\boldsymbol{\Omega}' \times \mathbf{u}' = -\frac{1}{\rho_0}\boldsymbol{\nabla}' P' + \nu \nabla'^2 \mathbf{u}' + \frac{1}{\rho_0}\mathbf{F}'_{\mathrm{A}} + \frac{1}{\rho_0}\mathbf{F}'_{\mathrm{L}}\,. \tag{B.1}$$

Here, ρ_0 is the reference density, $\mathbf{u}'$ is the fluid velocity relative to the rotating frame, t' is time, $\boldsymbol{\Omega}'$ is the container's rotation vector, P' is the modified pressure, ν is the kinematic viscosity, buoyancy forces are represented by $\mathbf{F}'_{\mathrm{A}}$, and magnetic (Lorentz) forces by $\mathbf{F}'_{\mathrm{L}}$. $\boldsymbol{\nabla}'$ is the gradient operator (see Appendix A.1), while primes indicate that a quantity is dimensional, but is to be nondimensionalized later.

The Navier-Stokes equation must be solved simultaneously with a continuity, or mass conservation, equation. In general this is written in terms of the density ρ, which can vary in space and time. However, under the Boussinesq approximation, ρ is replaced with the (constant in space and time) ρ_0. Thus, the continuity equation is transformed from its full

form (on the left) to its Boussinesq form (on the right):

$$\frac{\partial \rho}{\partial t'} + \boldsymbol{\nabla}' \cdot (\rho \mathbf{u}') = 0 \quad \rightarrow \quad \boldsymbol{\nabla}' \cdot \mathbf{u}' = 0 \,. \tag{B.2}$$

The buoyancy forces $\mathbf{F}'_{\mathrm{A}}$ can arise from either thermal or chemical variations in the fluid. In the interest of simplicity, the model currently being constructed assumes there is no chemical buoyancy, and also that there are no heat sources, such as radioactive elements, within the fluid itself. The only sources of heat in the model are then thermal fluxes through its boundaries, with the temperature at any point in the fluid governed by the temperature equation. With κ as the thermal diffusivity and T' as temperature,

$$\frac{\partial T'}{\partial t'} = -\left(\mathbf{u}' \cdot \boldsymbol{\nabla}'\right) T' + \kappa \nabla'^2 T' \,. \tag{B.3}$$

The magnetic field $\mathbf{B}'$ is governed by Maxwell's equations, in which $\eta = 1/\sigma\mu_0$ is the magnetic diffusivity, σ is the electrical conductivity, and μ_0 is the permeability of free space. In particular, $\mathbf{B}'$ obeys both the induction equation

$$\frac{\partial \mathbf{B}'}{\partial t'} = \boldsymbol{\nabla}' \times (\mathbf{u}' \times \mathbf{B}') + \eta \nabla'^2 \mathbf{B}' \,, \tag{B.4}$$

as well as Gauss' law for magnetism, written here in its differential form:

$$\boldsymbol{\nabla}' \cdot \mathbf{B}' = 0 \,. \tag{B.5}$$

B.2 Buoyancy Force

As discussed in the previous section, the model being constructed here assumes, for reasons of simplicity, no chemical or radioactive sources of buoyancy. The absence of chemical buoyancy implies that the only buoyant forces are due to temperature variations. The full temperature T' can be decomposed into a steady, conducting temperature profile T'_0 and a perturbation

component Θ' (see Eq.(2.15), in Section 2.3.5), such that for a position $\mathbf{x}$,

$$T'(t, \mathbf{x}) = T'_0(\mathbf{x}) + \Theta'(t, \mathbf{x})\,. \tag{B.6}$$

It is simplest to assume that the density varies with temperature in proportion to its current value. With α as the thermal expansion coefficient, this relationship is

$$\frac{\partial \rho}{\partial T'} = \frac{\partial \rho}{\partial \Theta'} = -\alpha \rho\,, \tag{B.7}$$

Defining $\rho_0 = \rho(T'_0)$ and $\Delta\rho = \rho(T') - \rho_0$, the full density ρ may be expanded about the background temperature T'_0 as

$$\Delta\rho = \left.\frac{\partial \rho}{\partial \Theta'}\right|_{\Theta'=0} \Theta' + \mathcal{O}(\Theta'^2) = -\alpha\rho_0\Theta' + \mathcal{O}(\Theta'^2)\,. \tag{B.8}$$

The buoyancy force is simply the density anomaly $\Delta\rho$ multiplied by the local gravitational acceleration. Ignoring the higher-order terms of Eq.(B.8), defining g_0 as the strength of gravitational acceleration at the CMB, and assuming gravitational strength increases linearly between the inner and outer core, $\mathbf{F}'_{\mathrm{A}}$ can be approximated as

$$\mathbf{F}'_{\mathbf{A}} = \Delta\rho\mathbf{g} = -\alpha\rho_0\Theta'\mathbf{g}\,, \quad \mathbf{g} = -g_0\frac{\mathbf{r}'}{r_2}\,, \tag{B.9}$$

where $\mathbf{r}'$ is the radial position of the point in question.

B.3 Magnetic Force

Because current density $\mathbf{J}'$ is defined as

$$\mathbf{J}' = \frac{1}{\mu_0}\boldsymbol{\nabla}' \times \mathbf{B}\,, \tag{B.10}$$

the Lorentz force experienced by a liquid metal in the presence of a magnetic field is

$$\mathbf{F}'_{\mathrm{L}} = \mathbf{J}' \times \mathbf{B}' = \left(\frac{1}{\mu_0} \boldsymbol{\nabla}' \times \mathbf{B}' \right) \times \mathbf{B}' \,. \tag{B.11}$$

B.4 Summary of Dimensional Equations

The combined set of Eqs.(B.1), (B.2), (B.3), (B.4), (B.5), (B.9), and (B.11) can be summarized as

$$\frac{\partial \mathbf{u}'}{\partial t'} + (\mathbf{u}' \cdot \boldsymbol{\nabla}')\, \mathbf{u}' + 2\boldsymbol{\Omega}' \times \mathbf{u}' = -\frac{1}{\rho_0} \boldsymbol{\nabla}' P' + \nu \nabla'^2 \mathbf{u}' + \alpha g_0 \Theta' \frac{\mathbf{r}'}{r_2} + \frac{1}{\rho_0 \mu_0} (\boldsymbol{\nabla}' \times \mathbf{B}') \times \mathbf{B}' \,, \tag{B.12}$$

$$\frac{\partial T'}{\partial t'} = -(\mathbf{u}' \cdot \boldsymbol{\nabla}')\, T' + \kappa \nabla'^2 T' \,, \tag{B.13}$$

$$\frac{\partial \mathbf{B}'}{\partial t'} = \boldsymbol{\nabla}' \times (\mathbf{u}' \times \mathbf{B}') + \eta \nabla'^2 \mathbf{B}' \,, \tag{B.14}$$

$$\boldsymbol{\nabla}' \cdot \mathbf{u}' = 0 \,, \quad \boldsymbol{\nabla}' \cdot \mathbf{B}' = 0 \,. \tag{B.15}$$

Appendix C

Nondimensionalization

Eqs.(B.12) through (B.15) from Appendix B are nondimensionalized using the scalings shown in Table 2.2.

C.1 Navier-Stokes Equation

Plugging in the appropriate scales, the Navier-Stokes equation of Eq.(B.12) becomes

$$\begin{aligned}\frac{\mathcal{U}}{\mathcal{T}}\frac{\partial \mathbf{u}}{\partial t} + \frac{\mathcal{U}^2}{\mathcal{L}}\left(\mathbf{u}\cdot\boldsymbol{\nabla}\right)\mathbf{u} + 2\Omega\mathcal{U}\mathbf{e}_z \times \mathbf{u} \\ = -\frac{1}{\rho_0}\frac{\mathcal{P}}{\mathcal{L}}\boldsymbol{\nabla}P + \nu\frac{\mathcal{U}}{\mathcal{L}^2}\nabla^2\mathbf{u} + \alpha g_0 \Delta T \mathcal{L}\Theta\frac{\mathbf{r}}{r_2} + \frac{1}{\rho_0\mu_0}\frac{\mathcal{B}^2}{\mathcal{L}}\left(\boldsymbol{\nabla}\times\mathbf{B}\right)\times\mathbf{B}\,. \end{aligned} \tag{C.1}$$

Replacing $\mathcal{U}$ with $\frac{\mathcal{L}}{\mathcal{T}}$,

$$\begin{aligned}\frac{\mathcal{L}}{\mathcal{T}^2}\frac{\partial \mathbf{u}}{\partial t} + \frac{\mathcal{L}}{\mathcal{T}^2}\left(\mathbf{u}\cdot\boldsymbol{\nabla}\right)\mathbf{u} + 2\frac{\mathcal{L}}{\mathcal{T}^2}\left(\mathbf{e}_z \times \mathbf{u}\right) \\ = -\frac{1}{\rho_0}\frac{\mathcal{P}}{\mathcal{L}}\boldsymbol{\nabla}P + \nu\frac{1}{\mathcal{L}\mathcal{T}}\nabla^2\mathbf{u} + \Delta T \mathcal{L}\alpha g_0\Theta\frac{\mathbf{r}}{r_2} + \frac{1}{\rho_0\mu_0}\frac{\mathcal{B}^2}{\mathcal{L}}\left(\boldsymbol{\nabla}\times\mathbf{B}\right)\times\mathbf{B}\,. \end{aligned} \tag{C.2}$$

Multiplying by $\frac{\mathcal{T}^2}{\mathcal{L}}$,

$$\begin{aligned}&\frac{\partial \mathbf{u}}{\partial t} + (\mathbf{u}\cdot\boldsymbol{\nabla})\,\mathbf{u} + 2\mathbf{e}_z \times \mathbf{u} \\ &\quad = -\frac{1}{\rho_0}\frac{\mathcal{P}\mathcal{T}^2}{\mathcal{L}^2}\boldsymbol{\nabla} P + \nu\frac{\mathcal{T}}{\mathcal{L}^2}\nabla^2\mathbf{u} + \mathcal{T}^2\Delta T\alpha g_0\Theta\frac{\mathbf{r}}{r_2} + \frac{1}{\rho_0\mu_0}\frac{\mathcal{B}^2\mathcal{T}^2}{\mathcal{L}^2}(\boldsymbol{\nabla}\times\mathbf{B})\times\mathbf{B}\,.\end{aligned} \tag{C.3}$$

Replacing $\mathcal{L}$, $\mathcal{T}$, $\mathcal{P}$, and $\mathcal{B}$ with the quantities they represent,

$$\begin{aligned}&\frac{\partial \mathbf{u}}{\partial t} + (\mathbf{u}\cdot\boldsymbol{\nabla})\,\mathbf{u} + 2\mathbf{e}_z \times \mathbf{u} \\ &\quad = -\boldsymbol{\nabla} P + \underbrace{\frac{\nu}{\Omega r_2^2}}_{E}\nabla^2\mathbf{u} + \underbrace{\frac{\alpha g_0\Delta T}{r_2\Omega^2}}_{Ra^*=\frac{E^2 Ra}{Pr}}\Theta\mathbf{r} + (\boldsymbol{\nabla}\times\mathbf{B})\times\mathbf{B}\,.\end{aligned} \tag{C.4}$$

Then, in terms of the Ekman number E and modified Rayleigh number Ra^*(summarized in Table 2.3), the nondimensional Navier-Stokes equation is

$$\boxed{\frac{\partial \mathbf{u}}{\partial t} + (\mathbf{u}\cdot\boldsymbol{\nabla})\,\mathbf{u} + 2\mathbf{e}_z \times \mathbf{u} = -\boldsymbol{\nabla} P + E\nabla^2\mathbf{u} + Ra^*\Theta\mathbf{r} + (\boldsymbol{\nabla}\times\mathbf{B})\times\mathbf{B}}\,. \tag{C.5}$$

C.2 Temperature Equation

Plugging the appropriate scalings into the the temperature equation of Eq.(B.13),

$$\frac{\Delta T}{\mathcal{T}}\frac{\partial T}{\partial t} = -\frac{\mathcal{U}\Delta T}{\mathcal{L}}(\mathbf{u}\cdot\boldsymbol{\nabla})\,T + \kappa\frac{\Delta T}{\mathcal{L}^2}\nabla^2 T\,. \tag{C.6}$$

Replacing $\mathcal{U}$ with $\frac{\mathcal{L}}{\mathcal{T}}$, and multiplying by $\frac{\mathcal{T}}{\Delta T}$, gives

$$\frac{\partial T}{\partial t} = -(\mathbf{u}\cdot\boldsymbol{\nabla})\,T + \kappa\frac{\mathcal{T}}{\mathcal{L}^2}\nabla^2 T\,. \tag{C.7}$$

Replacing $\mathcal{T}$ and $\mathcal{L}$ with the quantities they represent,

$$\frac{\partial T}{\partial t} = -\left(\mathbf{u}\cdot\boldsymbol{\nabla}\right)T + \underbrace{\frac{\kappa}{\Omega r_2^2}}_{E/P_r}\nabla^2 T\,. \tag{C.8}$$

So, in terms of the Ekman number E and Prandtl number P_r (summarized in Table 2.3), the nondimensional temperature equation is

$$\boxed{\frac{\partial T}{\partial t} = -\left(\mathbf{u}\cdot\boldsymbol{\nabla}\right)T + \frac{E}{P_r}\nabla^2 T}\,. \tag{C.9}$$

C.3 Induction Equation

Plugging the appropriate scalings into the the induction equation of Eq.(B.14),

$$\frac{\mathcal{B}}{\mathcal{T}}\frac{\partial \mathbf{B}}{\partial t} = \frac{\mathcal{U}\mathcal{B}}{\mathcal{L}}\boldsymbol{\nabla}\times\left(\mathbf{u}\times\mathbf{B}\right) + \eta\frac{\mathcal{B}}{\mathcal{L}^2}\nabla^2\mathbf{B}\,. \tag{C.10}$$

Replacing $\mathcal{U}$ with $\frac{\mathcal{L}}{\mathcal{T}}$, and multiplying by $\frac{\mathcal{T}}{\mathcal{B}}$, gives

$$\frac{\partial \mathbf{B}}{\partial t} = \boldsymbol{\nabla}\times\left(\mathbf{u}\times\mathbf{B}\right) + \eta\frac{\mathcal{T}}{\mathcal{L}^2}\nabla^2\mathbf{B}\,. \tag{C.11}$$

Replacing $\mathcal{T}$ and $\mathcal{L}$ with the quantities they represent,

$$\frac{\partial \mathbf{B}}{\partial t} = \boldsymbol{\nabla}\times\left(\mathbf{u}\times\mathbf{B}\right) + \underbrace{\frac{\eta}{\Omega r_2^2}}_{E/P_m}\nabla^2\mathbf{B}\,. \tag{C.12}$$

So, in terms of the Ekman number E and magnetic Prandtl number P_m (summarized in Table 2.3), the nondimensional induction equation is

$$\boxed{\frac{\partial \mathbf{B}}{\partial t} = \boldsymbol{\nabla}\times\left(\mathbf{u}\times\mathbf{B}\right) + \frac{E}{P_m}\nabla^2\mathbf{B}}\,. \tag{C.13}$$

C.4 Auxiliary Equations

Nondimensionalizing Eqs.(B.15) is a trivial exercise, since they contain only one term each. Using the appropriate scales from Table 2.2,

$$\frac{\mathcal{U}}{\mathcal{L}}\boldsymbol{\nabla}\cdot\mathbf{u}=0\,,\quad \frac{\mathcal{B}}{\mathcal{L}}\boldsymbol{\nabla}\cdot\mathbf{B}=0\,. \tag{C.14}$$

Because both equations are equal to zero, the scale terms may be dropped, leaving only

$$\boxed{\boldsymbol{\nabla}\cdot\mathbf{u}=0\,,\quad \boldsymbol{\nabla}\cdot\mathbf{B}=0}\,. \tag{C.15}$$

C.5 Summary of Nondimensional Equations

The nondimensionalized Eqs.(C.5), (C.9), (C.13), and (C.15) can be summarized as

$$\frac{\partial\mathbf{u}}{\partial t}+(\mathbf{u}\cdot\boldsymbol{\nabla})\,\mathbf{u}+2\mathbf{e}_z\times\mathbf{u}=-\boldsymbol{\nabla}P+E\nabla^2\mathbf{u}+Ra^*\Theta\mathbf{r}+(\boldsymbol{\nabla}\times\mathbf{B})\times\mathbf{B}\,, \tag{C.16}$$

$$\frac{\partial T}{\partial t}=-(\mathbf{u}\cdot\boldsymbol{\nabla})\,T+\frac{E}{P_r}\nabla^2T\,, \tag{C.17}$$

$$\frac{\partial\mathbf{B}}{\partial t}=\boldsymbol{\nabla}\times(\mathbf{u}\times\mathbf{B})+\frac{E}{P_m}\nabla^2\mathbf{B}\,, \tag{C.18}$$

$$\boldsymbol{\nabla}\cdot\mathbf{u}=0,\quad \boldsymbol{\nabla}\cdot\mathbf{B}=0\,. \tag{C.19}$$

Appendix D

Constructing a QG Model

This appendix transforms the nondimensionalized governing Eqs.(C.16)-(C.19) of Appendix C into their Quasi-Geostrophic, or QG, forms. The geometry used is shown in Figure 2.1, while the assumptions made in performing the transformations are discussed in Section 2.3.3. The mathematical results of Appendix A will be used extensively throughout.

D.1 Axial Vorticity Equation

Letting the current density $\mathbf{J} = \boldsymbol{\nabla} \times \mathbf{B}$, where $\mathbf{B}$ is the magnetic field, the curl of the nondimensional Navier-Stokes equation (Eq.(C.16)) is

$$\boldsymbol{\nabla} \times \left(\frac{\partial \mathbf{u}}{\partial t} \right) + \boldsymbol{\nabla} \times \left((\mathbf{u} \cdot \boldsymbol{\nabla})\, \mathbf{u} \right) + 2\, \boldsymbol{\nabla} \times (\mathbf{e}_z \times \mathbf{u})$$
$$= -\boldsymbol{\nabla} \times (\boldsymbol{\nabla} P) + E\, \boldsymbol{\nabla} \times \left(\nabla^2 \mathbf{u} \right) + Ra^*\, \boldsymbol{\nabla} \times (\Theta \mathbf{r}) + \boldsymbol{\nabla} \times (\mathbf{J} \times \mathbf{B}) \,, \qquad \text{(D.1)}$$

where $\mathbf{u}$ is velocity relative to the rotating frame, P is the modified pressure, E is the Ekman number, Ra^* is the modified Rayleigh number, Θ is the local temperature perturbation, t is time, and $\boldsymbol{\nabla}$ is the gradient operator.

Because the curl of a gradient is identically zero, the pressure term vanishes immediately. In addition, the time derivative can be written in terms of vorticity. Dotting the resulting vorticity equation with $\mathbf{e}_z$ discards the ω_s and ω_ϕ vorticity components, which the QG approximation assumes to be negligible compared to ω_z:

$$\begin{aligned}\frac{\partial \omega_z}{\partial t} &+ \underbrace{\mathbf{e}_z \cdot (\boldsymbol{\nabla} \times ((\mathbf{u} \cdot \boldsymbol{\nabla})\,\mathbf{u}))}_{①} + \underbrace{2\,\mathbf{e}_z \cdot (\boldsymbol{\nabla} \times (\mathbf{e}_z \times \mathbf{u}))}_{②} \\ &= + \underbrace{E\,\mathbf{e}_z \cdot \left(\boldsymbol{\nabla} \times \left(\nabla^2 \mathbf{u}\right)\right)}_{③} + \underbrace{Ra^*\,\mathbf{e}_z \cdot (\boldsymbol{\nabla} \times (\Theta \mathbf{r}))}_{④} + \underbrace{\mathbf{e}_z \cdot (\boldsymbol{\nabla} \times (\mathbf{J} \times \mathbf{B}))}_{⑤}\,. \end{aligned} \tag{D.2}$$

D.1.1 Simplification

The inertial term (①) of Eq.(D.2) can be expanded with a vector identity:

$$① = \mathbf{e}_z \cdot \left(\boldsymbol{\nabla} \times \left(\frac{1}{2}\boldsymbol{\nabla}\,(\mathbf{u} \cdot \mathbf{u}) - \mathbf{u} \times (\boldsymbol{\nabla} \times \mathbf{u})\right)\right) \tag{D.3}$$

The first term inside the brackets disappears, again because the curl of a gradient is zero. The second term becomes $\mathbf{u} \times \boldsymbol{\omega}$. A vector identity is used to expand the curl of it:

$$① = -\mathbf{e}_z \cdot (\mathbf{u}\,(\boldsymbol{\nabla} \cdot \boldsymbol{\omega}) - \boldsymbol{\omega}\,(\boldsymbol{\nabla} \cdot \mathbf{u}) + (\boldsymbol{\omega} \cdot \boldsymbol{\nabla})\,\mathbf{u} - (\mathbf{u} \cdot \boldsymbol{\nabla})\,\boldsymbol{\omega}) \tag{D.4}$$

Because both $\boldsymbol{\omega}$ and $\mathbf{u}$ are solenoidal, the first two terms are zero. The axial component of the remaining terms is

$$① = (\mathbf{u} \cdot \boldsymbol{\nabla})\,\omega_z - (\boldsymbol{\omega} \cdot \boldsymbol{\nabla})\,u_z\,. \tag{D.5}$$

However, ω_z is assumed rigid, so its z-derivative is zero. Meanwhile, ω_s and ω_ϕ are assumed

to be negligible next to ω_z, so terms involving them are discarded. This leaves

$$① = u_s \frac{\partial}{\partial s}\omega_z + \frac{u_\phi}{s}\frac{\partial}{\partial \phi}\omega_z - \omega_z \frac{\partial}{\partial z} u_z \,. \tag{D.6}$$

The Coriolis term (②) of Eq.(D.2) is also expanded by a vector identity:

$$② = 2\,\mathbf{e}_z \cdot \left(\mathbf{e}_z \left(\boldsymbol{\nabla}\cdot\mathbf{u}\right) - \mathbf{u}\left(\boldsymbol{\nabla}\cdot\mathbf{e}_z\right) + \left(\mathbf{u}\cdot\boldsymbol{\nabla}\right)\mathbf{e}_z - \left(\mathbf{e}_z\cdot\boldsymbol{\nabla}\right)\mathbf{u}\right) \,. \tag{D.7}$$

Because $\mathbf{u}$ is solenoidal, and $\mathbf{e}_z$ is constant, the first three terms within the brackets vanish. This leaves

$$② = -2\,\frac{\partial u_z}{\partial z} \,. \tag{D.8}$$

The diffusion term (③) of Eq.(D.2) is, as usual, expanded by a vector identity:

$$③ = \mathbf{e}_z \cdot E\,\boldsymbol{\nabla}\times\left(\boldsymbol{\nabla}\left(\boldsymbol{\nabla}\cdot\mathbf{u}\right) - \boldsymbol{\nabla}\times\left(\boldsymbol{\nabla}\times\mathbf{u}\right)\right) \,. \tag{D.9}$$

The first term within the brackets vanishes, because $\mathbf{u}$ is solenoidal. The second term may be rewritten in terms of $\boldsymbol{\omega}$. The result may be expanded with yet another vector identity:

$$③ = -\mathbf{e}_z \cdot E\,\left(\boldsymbol{\nabla}\left(\boldsymbol{\nabla}\cdot\boldsymbol{\omega}\right) - \nabla^2\boldsymbol{\omega}\right) \,. \tag{D.10}$$

The vorticity field is also solenoidal, so

$$③ = E\,\nabla^2\omega_z \,. \tag{D.11}$$

The buoyancy term (④) of Eq.(D.2) is simplified by translating the spherically radial vector ($\mathbf{r}$) to its in its cylindrical equivalent ($s\mathbf{e}_s + z\mathbf{e}_z$):

$$④ = Ra^*\,\mathbf{e}_z\cdot\boldsymbol{\nabla}\times\left[\Theta\left(s\mathbf{e}_s + z\mathbf{e}_z\right)\right] = -\frac{Ra^*}{s}\frac{\partial}{\partial\phi}\left(s\Theta\right) = -Ra^*\frac{\partial\Theta}{\partial\phi} \,. \tag{D.12}$$

The Lorentz term (⑤) of Eq.(D.2) is expanded using the same vector identity as was used for term ②:

$$⑤ = \mathbf{e}_z \cdot \left(\mathbf{J}\left(\boldsymbol{\nabla}\cdot\mathbf{B}\right) - \mathbf{B}\left(\boldsymbol{\nabla}\cdot\mathbf{J}\right) + \left(\mathbf{B}\cdot\boldsymbol{\nabla}\right)\mathbf{J} - \left(\mathbf{J}\cdot\boldsymbol{\nabla}\right)\mathbf{B}\right) . \tag{D.13}$$

Both $\mathbf{B}$ and $\mathbf{J}$ are solenoidal, causing the first two terms within the brackets to vanish. The second two become

$$⑤ = \left(\mathbf{B}\cdot\boldsymbol{\nabla}\right) J_z - \left(\mathbf{J}\cdot\boldsymbol{\nabla}\right) B_z \, . \tag{D.14}$$

However, similar to the vorticity in Eq.(D.5), the s and ϕ components of the current density are assumed to be small relative to J_z, and are therefore ignored. Because the background field is assumed to be curl-free ($\mathbf{J}_0 = 0$), so $J_z \to j_z$. Like ω_z, j_z is assumed to be rigid, causing its z-derivative to vanish. So,

$$⑤ = B_s \frac{\partial}{\partial s} j_z + \frac{B_\phi}{s}\frac{\partial}{\partial \phi} j_z - j_z \frac{\partial}{\partial z} B_z \, . \tag{D.15}$$

With the simplifications calculated for terms ① - ⑤, Eq.(D.2) becomes

$$\begin{aligned} &\frac{\partial \omega_z}{\partial t} + \left(u_s \frac{\partial}{\partial s}\omega_z + \frac{u_\phi}{s}\frac{\partial}{\partial \phi}\omega_z - \omega_z \frac{\partial}{\partial z} u_z \right) - 2\,\frac{\partial u_z}{\partial z} \\ &\qquad = E\,\nabla^2 \omega_z - Ra^* \frac{\partial \Theta}{\partial \phi} + \left(B_s \frac{\partial}{\partial s} j_z + \frac{B_\phi}{s}\frac{\partial}{\partial \phi} j_z - j_z \frac{\partial}{\partial z} B_z \right) \end{aligned} \tag{D.16}$$

D.1.2 Axial Averaging

Axially averaging Eq.(D.16),

$$\left\langle \frac{\partial \omega_z}{\partial t} \right\rangle + \left\langle u_s \frac{\partial}{\partial s}\omega_z + \frac{u_\phi}{s}\frac{\partial}{\partial \phi}\omega_z - \omega_z \frac{\partial}{\partial z} u_z \right\rangle - \left\langle 2 \frac{\partial}{\partial z} u_z \right\rangle$$
$$= E \left\langle \nabla^2 \omega_z \right\rangle - Ra^* \left\langle \frac{\partial \Theta}{\partial \phi} \right\rangle + \left\langle B_s \frac{\partial}{\partial s} j_z + \frac{B_\phi}{s}\frac{\partial}{\partial \phi} j_z - j_z \frac{\partial}{\partial z} B_z \right\rangle . \tag{D.17}$$

As discussed in Chapter 2, $\mathbf{u}_H$, $\mathbf{B}_H$, ω_z, and j_z are all assumed to be rigid, with values at the upper and lower boundaries equal to their axial averages[1]. Thus, the axial averages of terms with time, radial, and azimuthal derivatives are equal to the functions being averaged over. The axial average of the diffusion term can be calculated with Eq.(A.65). This leaves only the axial averages of the axial derivatives. With the understanding that a term without angled brackets has been axially averaged, Eq.(D.17) becomes

$$\frac{\partial \omega_z}{\partial t} + \left(u_s \frac{\partial}{\partial s} + \frac{u_\phi}{s}\frac{\partial}{\partial \phi} \right) \omega_z - (2 + \omega_z) \left\langle \frac{\partial}{\partial z} u_z \right\rangle$$
$$= \left(B_s \frac{\partial}{\partial s} + \frac{B_\phi}{s}\frac{\partial}{\partial \phi} \right) j_z - j_z \left\langle \frac{\partial}{\partial z} B_z \right\rangle + E \nabla_H^2 \omega_z - Ra^* \frac{\partial}{\partial \phi} \Theta . \tag{D.18}$$

The remaining axial averages may be evaluated only if some form is assumed for the axial profiles of u_z and B_z. The no-penetration boundary condition hold that, for a vector normal to the upper (+) or lower (−) boundary $\hat{\mathbf{n}} = s\mathbf{e}_s \pm L\mathbf{e}_z$,

$$\mathbf{u} \cdot \hat{\mathbf{n}} = 0 \quad \Rightarrow \quad u_z = \mp \frac{s}{L} u_s . \tag{D.19}$$

The axial flow must be zero at $z = 0$, and increase/decrease to the value specified in Eq.(D.19)

[1]Such an assumption is not strictly consistent with no-slip boundary conditions, though the two can be reconciled if the limits of the axial averaging integral are interpreted as lying just outside the upper and lower boundary layers. Unfortunately, this interpretation implies that $\mathbf{u} \cdot \hat{\mathbf{n}} \neq 0$, meaning that the axial profiles of u_z would need to be altered by the addition of an Ekman pumping term (see, for example, Greenspan (1968)). However, such a term is proportional to $E^{\frac{1}{2}}$, and is therefore generally small compared to the contribution from the no-penetration condition, proportional to β. Therefore, Ekman pumping is not likely to significantly alter the mechanisms responsible for magnetically-forced mean zonal flows in this highly idealized model, and is therefore ignored for simplicity.

at $z = \pm L$. The simplest relation between u_z and z which meets these criteria is a linear one:

$$u_z = -\frac{s}{L}\frac{z}{L}u_s = \beta u_s z\,. \tag{D.20}$$

Appendix F shows that, in order for the model to conserve angular momentum, a similar axial profile must be assumed for the magnetic field. This is compatible with the $a = 0$ boundary condition assumed in Chapter 2. Thus,

$$B_z = -\frac{s}{L}\frac{z}{L}B_s = \beta B_s z\,. \tag{D.21}$$

With the profiles specified by Eqs.(D.20) and (D.21), Eq.(D.19) becomes

$$\boxed{\frac{\partial \omega_z}{\partial t} + \left(u_s\frac{\partial}{\partial s} + \frac{u_\phi}{s}\frac{\partial}{\partial \phi}\right)\omega_z - (2+\omega_z)\,\beta u_s = \left(B_s\left(\frac{\partial}{\partial s} - \beta\right) + \frac{B_\phi}{s}\frac{\partial}{\partial \phi}\right) j_z + E\,\nabla_H^2 \omega_z - Ra^*\frac{\partial \Theta}{\partial \phi}}\,. \tag{D.22}$$

D.2 Zonal Flow Equation

In principle, Eq.(D.22) contains the zonal flow. However, it is convenient to have a separate equation which explicitly describes the zonal part of the flow, if only to simplify analysis. This equation is derived by azimuthally averaging the azimuthal component of Eq.(C.16):

$$\overline{\mathbf{e}_\phi \cdot \left(\frac{\partial \mathbf{u}}{\partial t}\right)} + \overline{\mathbf{e}_\phi \cdot ((\mathbf{u}\cdot\boldsymbol{\nabla})\,\mathbf{u})} + 2\,\overline{\mathbf{e}_\phi \cdot (\mathbf{e}_z \times \mathbf{u})} = -\overline{\mathbf{e}_\phi \cdot (\boldsymbol{\nabla} P)} + E\,\left(\overline{\mathbf{e}_\phi \cdot (\nabla^2 \mathbf{u})}\right) + \overline{\mathbf{e}_\phi \cdot ((\boldsymbol{\nabla}\times\mathbf{B})\times\mathbf{B})}\,. \tag{D.23}$$

The first term immediately becomes the time derivative of $\overline{u_\phi}$. The pressure term vanishes,

since pressure must be periodic in azimuth:

$$\overline{\mathbf{e}_\phi \cdot (\boldsymbol{\nabla} P)} = \overline{\frac{1}{s}\frac{\partial P}{\partial \phi}} = 0\,. \tag{D.24}$$

With these two adjustments, Eq.(D.23) becomes

$$\frac{\partial \overline{u_\phi}}{\partial t} + \underbrace{\overline{\mathbf{e}_\phi \cdot ((\mathbf{u}\cdot\boldsymbol{\nabla})\,\mathbf{u})} + 2\,\overline{\mathbf{e}_\phi \cdot (\mathbf{e}_z \times \mathbf{u})}}_{①} = E\,\underbrace{\left(\overline{\mathbf{e}_\phi \cdot (\nabla^2 \mathbf{u})}\right)}_{②} + \underbrace{\overline{\mathbf{e}_\phi \cdot ((\boldsymbol{\nabla}\times\mathbf{B})\times\mathbf{B})}}_{③}\,. \tag{D.25}$$

D.2.1 Simplification

Term ① may be expanded as

$$① = \overline{\left(u_s \frac{\partial}{\partial s} u_\phi + \frac{u_\phi}{s}\frac{\partial}{\partial \phi} u_\phi + u_z \frac{\partial}{\partial z} u_\phi + \frac{u_s u_\phi}{s}\right)} + 2\,\overline{u_s}\,. \tag{D.26}$$

Because of mass conservation, u_s lacks an axisymmetric component. u_ϕ is rigid, so its z-derivative is zero. The azimuthal derivative may be rewritten $\frac{u_\phi}{s}\frac{\partial}{\partial\phi}u_\phi = \frac{1}{2s}\frac{\partial}{\partial\phi}u_\phi^2$, which is zero since u_ϕ is periodic in azimuth. So,

$$① = \overline{u_s \frac{\partial}{\partial s} u_\phi} + \frac{\overline{u_s u_\phi}}{s} = \overline{\frac{u_s}{s}\frac{\partial}{\partial s}\left(s u_\phi\right)}\,. \tag{D.27}$$

The viscosity term (②) may be expanded as

$$② = \overline{\left(\nabla^2 u_\phi - \frac{u_\phi}{s^2} + \frac{2}{s^2}\frac{\partial u_s}{\partial \phi}\right)} = \overline{\frac{\partial^2 u_\phi}{\partial s^2}} + \overline{\frac{1}{s}\frac{\partial u_\phi}{\partial s}} + \overline{\frac{1}{s^2}\frac{\partial^2 u_\phi}{\partial \phi^2}} + \overline{\frac{\partial^2 u_\phi}{\partial z^2}} - \frac{\overline{u_\phi}}{s^2} + \frac{2}{s^2}\overline{\frac{\partial u_s}{\partial \phi}}\,. \tag{D.28}$$

Because both u_s and u_ϕ are periodic in azimuth, both azimuthal derivatives vanish. Since derivatives in s and z do not affect azimuthal averaging operations, the latter can be brought

inside the derivatives and applied directly to u_ϕ itself:

$$② = \left(\frac{\partial^2}{\partial s^2} + \frac{1}{s}\frac{\partial}{\partial s} - \frac{1}{s^2} + \frac{\partial^2}{\partial z^2} \right) \overline{u_\phi} \,. \tag{D.29}$$

The Lorentz term (③) may be rewritten using a vector identity as

$$③ = \overline{\mathbf{e}_\phi \cdot \left((\mathbf{B} \cdot \boldsymbol{\nabla}) \mathbf{B} - \frac{1}{2} \boldsymbol{\nabla} (\mathbf{B} \cdot \mathbf{B}) \right)} \,. \tag{D.30}$$

Expanding this,

$$③ = \overline{B_s \frac{\partial}{\partial s} B_\phi} + \overline{\frac{B_s}{s} \frac{\partial}{\partial \phi} B_\phi} + \overline{B_z \frac{\partial}{\partial z} B_\phi} + \overline{\frac{B_s B_\phi}{s}} - \frac{1}{2s} \overline{\frac{\partial}{\partial \phi} (\mathbf{B} \cdot \mathbf{B})} \,. \tag{D.31}$$

$\mathbf{B}$ is periodic in azimuth, so both terms with ϕ-derivatives vanish. Of the remaining three terms, the two not involving $\frac{\partial}{\partial z}$ are combined to form

$$③ = \overline{\frac{B_s}{s} \frac{\partial}{\partial s} (s B_\phi)} + \overline{B_z \frac{\partial}{\partial z} B_\phi} \,. \tag{D.32}$$

The full magnetic field is decomposed into a steady, imposed background field $\mathbf{B}_0$, and a time-dependent perturbation field $\mathbf{b}$, such that $\mathbf{B} = \mathbf{B}_0 + \mathbf{b}$. The $B_{0\phi}$ component of the background field is assumed to be zero, while the background field as a whole is assumed to be axisymmetric. So,

$$③ = \underbrace{\left(\frac{B_{0s}}{s} \frac{\partial}{\partial s} \left(s \overline{b_\phi} \right) + B_{0z} \frac{\partial}{\partial z} \overline{b_\phi} \right)}_{Ⓐ} + \underbrace{\left(\overline{\frac{b_s}{s} \frac{\partial}{\partial s} (s b_\phi)} + \overline{b_z \frac{\partial}{\partial z} b_\phi} \right)}_{Ⓑ} \,. \tag{D.33}$$

The linear terms (Ⓐ) can be rewritten as

$$Ⓐ = \left(\frac{1}{s} \frac{\partial}{\partial s} \left(s B_{0s} \overline{b_\phi} \right) - \overline{b_\phi} \frac{\partial}{\partial s} B_{0s} \right) + \left(\frac{\partial}{\partial z} \left(B_{0z} \overline{b_\phi} \right) - \overline{b_\phi} \frac{\partial}{\partial z} B_{0z} \right) \,. \tag{D.34}$$

Rearranging,

$$\text{Ⓐ} = \frac{1}{s}\frac{\partial}{\partial s}\left(sB_{0s}\overline{b_\phi}\right) - \overline{b_\phi}\left(\frac{\partial}{\partial s}B_{0s} + \frac{\partial}{\partial z}B_{0z}\right) + \frac{\partial}{\partial z}\left(B_{0z}\overline{b_\phi}\right) . \tag{D.35}$$

Recalling the assumption that $B_{0\phi} = 0$

$$\boldsymbol{\nabla}\cdot\mathbf{B}_0 = \frac{1}{s}\frac{\partial}{\partial s}\left(sB_{0s}\right) + \frac{\partial}{\partial z}B_{0z} = 0 \quad \Rightarrow \quad \frac{\partial}{\partial s}B_{0s} + \frac{\partial}{\partial z}B_{0z} = -\frac{B_{0s}}{s} . \tag{D.36}$$

Substituting this expression into Eq.(D.35),

$$\text{Ⓐ} = \frac{1}{s}\frac{\partial}{\partial s}\left(sB_{0s}\overline{b_\phi}\right) + \frac{B_{0s}\overline{b_\phi}}{s} + \frac{\partial}{\partial z}\left(B_{0z}\overline{b_\phi}\right) . \tag{D.37}$$

Using Eq.(A.14) to combine the first two terms on the right-hand side, this becomes

$$\text{Ⓐ} = \frac{1}{s^2}\frac{\partial}{\partial s}\left(s^2B_{0s}\overline{b_\phi}\right) + \frac{\partial}{\partial z}\left(B_{0z}\overline{b_\phi}\right) . \tag{D.38}$$

A similar procedure to that followed for Ⓐ is now applied to the nonlinear terms (Ⓑ). They can be rewritten (similar to Eq.(D.34) and rearranged (similar to Eq.(D.35) to produce

$$\text{Ⓑ} = \frac{1}{s}\frac{\partial}{\partial s}\left(s\overline{b_sb_\phi}\right) - \overline{b_\phi\left(\frac{\partial}{\partial s}b_s + \frac{\partial}{\partial z}b_z\right)} + \frac{\partial}{\partial z}\left(\overline{b_\phi b_z}\right) . \tag{D.39}$$

Using the continuity equation $\boldsymbol{\nabla}\cdot\mathbf{b} = 0$,

$$\frac{\partial}{\partial s}b_s + \frac{\partial}{\partial z}b_z = -\frac{1}{s}\left(b_s + \frac{\partial}{\partial\phi}b_\phi\right) , \tag{D.40}$$

which causes

$$\text{Ⓑ} = \frac{1}{s}\frac{\partial}{\partial s}\left(s\overline{b_sb_\phi}\right) + \frac{\overline{b_sb_\phi}}{s} - \overline{\frac{b_\phi}{s}\frac{\partial}{\partial\phi}b_\phi} + \frac{\partial}{\partial z}\left(\overline{b_\phi b_z}\right) . \tag{D.41}$$

The first two terms on the right-hand side can be combined with one another, while the azimuthal derivative can be rewritten as $\overline{\frac{b_\phi}{s}\frac{\partial}{\partial\phi}b_\phi} = \frac{1}{2s}\overline{\frac{\partial}{\partial\phi}b_\phi^2}$. Because b_ϕ is periodic in azimuth,

the entire term vanishes:

$$\text{Ⓑ} = \frac{1}{s^2}\frac{\partial}{\partial s}\left(s^2\overline{b_s b_\phi}\right) + \frac{\partial}{\partial z}\left(\overline{b_\phi b_z}\right) . \tag{D.42}$$

Combining the expressions for Ⓐ and Ⓑ, ③ becomes

$$\text{③} = \left(\frac{1}{s^2}\frac{\partial}{\partial s}\left(s^2 B_{0s}\overline{b_\phi}\right) + \frac{\partial}{\partial z}\left(B_{0z}\overline{b_\phi}\right)\right) + \left(\frac{1}{s^2}\frac{\partial}{\partial s}\left(s^2\overline{b_s b_\phi}\right) + \frac{\partial}{\partial z}\left(\overline{b_\phi b_z}\right)\right) . \tag{D.43}$$

Using the expressions for ①, ②, and ③ from Eqs.(D.27), (D.29), and (D.43), Eq.(D.25) becomes

$$\begin{aligned}\frac{\partial\overline{u_\phi}}{\partial t} + \overline{\frac{u_s}{s}\frac{\partial}{\partial s}\left(s u_\phi\right)} =& E\left(\frac{\partial^2}{\partial s^2} + \frac{1}{s}\frac{\partial}{\partial s} - \frac{1}{s^2} + \frac{\partial^2}{\partial z^2}\right)\overline{u_\phi} \\ &+ \left(\frac{1}{s^2}\frac{\partial}{\partial s}\left(s^2 B_{0s}\overline{b_\phi}\right) + \frac{\partial}{\partial z}\left(B_{0z}\overline{b_\phi}\right)\right) + \left(\frac{1}{s^2}\frac{\partial}{\partial s}\left(s^2\overline{b_s b_\phi}\right) + \frac{\partial}{\partial z}\left(\overline{b_\phi b_z}\right)\right) .\end{aligned} \tag{D.44}$$

D.2.2 Axial Averaging

As in the non-axisymmetric case, axial averaging of the flow field is notionally done between boundary layers. Since the bulk of the horizontal flow field does not depend on z, the axial averages of the two terms on the left-hand side of Eq.(D.44) are unchanged by the axial averaging operation. Again using the convention that, in this section, quantities not contained within angled brackets are assumed to have been axially averaged, this means

$$\frac{\partial \overline{u_\phi}}{\partial t} + \overline{\frac{u_s}{s}\frac{\partial}{\partial s}\left(s u_\phi\right)} = \overbrace{E\left(\left\langle \frac{\partial^2}{\partial s^2}\overline{u_\phi}\right\rangle + \left\langle \frac{1}{s}\frac{\partial}{\partial s}\overline{u_\phi}\right\rangle - \left\langle \frac{1}{s^2}\overline{u_\phi}\right\rangle + \left\langle \frac{\partial^2}{\partial z^2}\overline{u_\phi}\right\rangle\right)}^{①} + \underbrace{\left\langle\left(\frac{1}{s^2}\frac{\partial}{\partial s}\left(s^2 B_{0s}\overline{b_\phi}\right) + \frac{\partial}{\partial z}\left(B_{0z}\overline{b_\phi}\right)\right)\right\rangle}_{②} + \underbrace{\left\langle\left(\frac{1}{s^2}\frac{\partial}{\partial s}\left(s^2\overline{b_s b_\phi}\right) + \frac{\partial}{\partial z}\left(\overline{b_\phi b_z}\right)\right)\right\rangle}_{③}. \tag{D.45}$$

A rigid horizontal flow field implies $\langle\overline{u_\phi}\rangle = \overline{u_\phi}|_{z=\pm L}$. Because of this, the $\left\langle \frac{\partial^2}{\partial s^2}\overline{u_\phi}\right\rangle$ part of the viscosity term (①) can be expanded according to Eq.(A.56). In addition, the $\left\langle \frac{\partial}{\partial s}\overline{u_\phi}\right\rangle$ part can be expanded according to Eq.(A.38):

$$\begin{aligned} ① = & \left(\frac{\partial^2}{\partial s^2}\left\langle\overline{u_\phi}\right\rangle + \beta\left(\frac{\partial}{\partial s}\left\langle\overline{u_\phi}\right\rangle - \frac{\partial}{\partial s}\overline{u_\phi}\Big|_{z=L}\right)\right) + \left(\frac{1}{s}\frac{\partial}{\partial s}\left\langle\overline{u_\phi}\right\rangle\right) \\ & + \left(\frac{1}{s^2}\left\langle\overline{u_\phi}\right\rangle\right) + \left(\frac{1}{2L}\left(\frac{\partial}{\partial z}\overline{u_\phi}\Big|_{z=L} - \frac{\partial}{\partial z}\overline{u_\phi}\Big|_{z=-L}\right)\right). \end{aligned} \tag{D.46}$$

Rearranging terms, and recognizing that, because of $\overline{u_\phi}$'s rigidity, $\frac{\partial}{\partial s}\overline{u_\phi}\big|_{z=L} = \frac{1}{2}\left(\frac{\partial}{\partial s}\overline{u_\phi}\big|_{z=L} + \frac{\partial}{\partial s}\overline{u_\phi}\big|_{z=-L}\right)$,

$$\begin{aligned} ① = & \left(\frac{\partial^2}{\partial s^2} + \left(\frac{1}{s}+\beta\right)\frac{\partial}{\partial s} - \frac{1}{s^2}\right)\left\langle\overline{u_\phi}\right\rangle \\ & - \frac{\beta}{2}\left(\frac{\partial}{\partial s}\overline{u_\phi}\Big|_{z=L} - \frac{\partial}{\partial s}\overline{u_\phi}\Big|_{z=-L}\right) + \frac{1}{2L}\left(\frac{\partial}{\partial z}\overline{u_\phi}\Big|_{z=L} - \frac{\partial}{\partial z}\overline{u_\phi}\Big|_{z=-L}\right). \end{aligned} \tag{D.47}$$

The boundary derivative terms depend on the boundary conditions being used. This model uses a free-slip boundary condition on the zonal velocity field, which can be expressed in spherical coordinates as

$$\frac{\partial}{\partial r}\left(\frac{\overline{u_\phi}}{r}\right)\Big|_{r=r_2} = \left(\frac{1}{r}\frac{\partial \overline{u_\phi}}{\partial r} - \frac{\overline{u_\phi}}{r^2}\right)\Big|_{r=r_2} = 0 \quad \Rightarrow \quad \overline{u_\phi}|_{r=r_2} = r\left.\frac{\partial \overline{u_\phi}}{\partial r}\right|_{r=r_2}. \tag{D.48}$$

Transforming this to cylindrical coordinates,

$$\overline{u_\phi}|_{z=\pm L} = \sqrt{s^2+z^2}\left(\frac{\partial s}{\partial r}\frac{\partial}{\partial s}+\frac{\partial z}{\partial r}\frac{\partial}{\partial z}\right)\overline{u_\phi}\Big|_{z=\pm L}. \tag{D.49}$$

Because $L=\sqrt{1-s^2}$, the leading factor is just 1. Meanwhile, $\frac{\partial s}{\partial r}\big|_{z=\pm L}=s$, and $\frac{\partial z}{\partial r}\big|_{z=\pm L}=\pm L$. So,

$$\frac{\partial\overline{u_\phi}}{\partial s}\bigg|_{z=\pm L} = \frac{\overline{u_\phi}}{s}\bigg|_{z=\pm L} \mp \frac{L}{s}\frac{\partial\overline{u_\phi}}{\partial z}\bigg|_{z=\pm L}. \tag{D.50}$$

Using the relation in (D.50) to transform the radial boundary derivatives of Eq.(D.47) into axial boundary derivatives,

$$\begin{aligned}①= &\left(\frac{\partial^2}{\partial s^2}+\left(\frac{1}{s}+\beta\right)\frac{\partial}{\partial s}-\frac{1}{s^2}\right)\langle\overline{u_\phi}\rangle\\ &-\frac{\beta}{2}\left(\frac{\overline{u_\phi}}{s}\bigg|_{z=L}-\frac{L}{s}\frac{\partial}{\partial z}\overline{u_\phi}\bigg|_{z=L}+\frac{\overline{u_\phi}}{s}\bigg|_{z=-L}+\frac{L}{s}\frac{\partial}{\partial z}\overline{u_\phi}\bigg|_{z=-L}\right)+\frac{1}{2L}\left(\frac{\partial}{\partial z}\overline{u_\phi}\bigg|_{z=L}-\frac{\partial}{\partial z}\overline{u_\phi}\bigg|_{z=-L}\right).\end{aligned} \tag{D.51}$$

Again taking advantage of u_ϕ's rigidity, and substituting $\beta=-\frac{s}{L^2}$,

$$\begin{aligned}①= &\left(\frac{\partial^2}{\partial s^2}+\left(\frac{1}{s}+\beta\right)\frac{\partial}{\partial s}-\frac{1}{s^2}-\frac{\beta}{s}\right)\langle\overline{u_\phi}\rangle\\ &-\frac{1}{2L}\left(\frac{\partial}{\partial z}\overline{u_\phi}\bigg|_{z=L}-\frac{\partial}{\partial z}\overline{u_\phi}\bigg|_{z=-L}\right)+\frac{1}{2L}\left(\frac{\partial}{\partial z}\overline{u_\phi}\bigg|_{z=L}-\frac{\partial}{\partial z}\overline{u_\phi}\bigg|_{z=-L}\right).\end{aligned} \tag{D.52}$$

The axial boundary derivatives thus cancel one another out. Taking advantage of Eqs.(A.16) to cause the remaining radial derivatives to act upon $\frac{\langle\overline{u_\phi}\rangle}{s}$, instead of just $\langle\overline{u_\phi}\rangle$:

$$①=\left(s\left(\frac{\partial^2}{\partial s^2}+\frac{2}{s}\frac{\partial}{\partial s}\right)+\left(\frac{1}{s}+\beta\right)(s)\left(\frac{\partial}{\partial s}+\frac{1}{s}\right)-\left(\frac{1}{s}+\beta\right)\right)\left(\frac{\langle u_\phi\rangle}{s}\right). \tag{D.53}$$

Expanding the first set of brackets, cancelling terms, and rearranging gives

$$① = s\left(\frac{\partial}{\partial s} + \frac{3}{s} + \beta\right)\left(\frac{\partial}{\partial s}\left(\frac{\langle\overline{u_\phi}\rangle}{s}\right)\right) . \tag{D.54}$$

Using the identity (A.14), this can be written

$$① = \frac{1}{s^2 L}\frac{\partial}{\partial s}\left(s^3 L\frac{\partial}{\partial s}\left(\frac{\langle\overline{u_\phi}\rangle}{s}\right)\right) . \tag{D.55}$$

The axial average of the radial derivative in the linear magnetic force term (②) is evaluated according to Eq.(A.35), while the axial average of the z-derivative is evaluated by the definition of the operation (Eq.(A.27)). Thus,

$$\begin{aligned} ② = \; & \frac{1}{s^2}\left(\frac{\partial}{\partial s}\left\langle s^2 B_{0s}\overline{b_\phi}\right\rangle + \beta\left(\left\langle s^2 B_{0s}\overline{b_\phi}\right\rangle - \frac{1}{2}\left(s^2 B_{0s}\,\overline{b_\phi}\big|_{z=L} + s^2 B_{0s}\,\overline{b_\phi}\big|_{z=-L}\right)\right)\right) \\ & + \left(\frac{1}{2L}\left(B_{0z}\overline{b_\phi}\right)\Big|_{z=-L}^{z=L}\right) . \end{aligned} \tag{D.56}$$

This can be rearranged into

$$\begin{aligned} ② = \; & \frac{1}{s^2}\left(\frac{\partial}{\partial s}\left(s^2\left\langle B_{0s}\right\rangle\left\langle\overline{b_\phi}\right\rangle\right) + \beta\left(s^2\left\langle B_{0s}\right\rangle\left\langle\overline{b_\phi}\right\rangle\right)\right) \\ & + \frac{1}{2L^2}\left(\left(sB_{0s} + LB_{0z}\right)\overline{b_\phi}\right)\Big|_{z=L} + \frac{1}{2L^2}\left(\left(sB_{0s} - LB_{0z}\right)\overline{b_\phi}\right)\Big|_{z=-L} . \end{aligned} \tag{D.57}$$

Because at the boundaries the spherically radial magnetic field $B_r|_{z=L} = (sB_{0s} + LB_{0z})|_{z=L}$ and $B_r|_{z=-L} = (sB_{0s} - LB_{0z})|_{z=-L}$,

$$② = \frac{1}{s^2}\left(\frac{\partial}{\partial s}\left(s^2\left\langle B_{0s}\right\rangle\left\langle\overline{b_\phi}\right\rangle\right) + \beta\left(s^2\left\langle B_{0s}\right\rangle\left\langle\overline{b_\phi}\right\rangle\right)\right) + \frac{1}{2L^2}\left(\left(B_r\overline{b_\phi}\right)\big|_{z=L} + \left(B_r\overline{b_\phi}\right)\big|_{z=-L}\right) . \tag{D.58}$$

However, it is assumed that $B_{0z}|_{z=\pm L} = \pm\beta B_{0s} L$ at the boundaries, so on them $B_r = 0$. Thus, the boundary terms to vanish. In fact, they *must* vanish if, as is done in this model, the outer core and mantle are assumed to not be electromagnetically coupled. Then, using the identity given in Eq.(A.14), the terms within in the first set of brackets on the right-hand side may be combined to form

$$② = \frac{1}{s^2 L}\frac{\partial}{\partial s}\left(s^2 L B_{0s}\overline{b_\phi}\right) . \tag{D.59}$$

Evaluating axial average of the nonlinear force (③) is done in a similar way as for the linear terms. Again using Eq.(A.35) to evaluate the axial average of the radial derivatives,

$$\begin{aligned} ③ = \; & \frac{1}{s^2}\left(\frac{\partial}{\partial s}\left\langle s^2\overline{b_s b_\phi}\right\rangle + \beta\left(\left\langle s^2\overline{b_s b_\phi}\right\rangle - \frac{1}{2}\left(s^2\,\overline{b_s b_\phi}\Big|_{z=L} + s^2\,\overline{b_s b_\phi}\Big|_{z=-L}\right)\right)\right) \\ & + \left(\frac{1}{2L}\left(\overline{b_\phi b_z}\right)\Big|_{z=-L}^{L}\right) . \end{aligned} \tag{D.60}$$

This can be rearranged into

$$\begin{aligned} ③ = \; & \frac{1}{s^2}\left(\frac{\partial}{\partial s}\left(s^2\left\langle\overline{b_s b_\phi}\right\rangle\right) + \beta\left(s^2\left\langle\overline{b_s b_\phi}\right\rangle\right)\right) \\ & + \frac{1}{2L^2}\left(\overline{\left(sb_s + Lb_z\right)b_\phi}\Big|_{z=L} + \overline{\left(sb_s - Lb_z\right)b_\phi}\Big|_{z=-L}\right) . \end{aligned} \tag{D.61}$$

As before, $sb_s \pm Lb_z = b_r$ at the upper and lower boundaries, so

$$③ = \frac{1}{s^2}\left(\frac{\partial}{\partial s}\left(s^2\left\langle\overline{b_s b_\phi}\right\rangle\right) + \beta\left(s^2\left\langle\overline{b_s b_\phi}\right\rangle\right)\right) + \frac{1}{2L^2}\left(\overline{b_r b_\phi}\Big|_{z=L} + \overline{b_r b_\phi}\Big|_{z=-L}\right) . \tag{D.62}$$

Also as before, since $b_z|_{z=\pm L} = \pm\beta b_s L$, $b_r = 0$ on the upper and lower boundaries. This causes the boundary terms to vanish. Then, using Eq.(A.14) to combine the remaining

terms,

$$③ = \frac{1}{s^2 L}\frac{\partial}{\partial s}\left(s^2 L\overline{b_s b_\phi}\right) . \tag{D.63}$$

This may be expanded as

$$③ = \frac{1}{s^2 L}\frac{\partial}{\partial s}\left(\overline{(sb_\phi)\,(sLb_s)}\right) = \overline{\frac{b_s}{s}\frac{\partial}{\partial s}(sb_\phi)} + \overline{\frac{b_\phi}{sL}\frac{\partial}{\partial s}(sLb_s)} . \tag{D.64}$$

Using the continuity equation, it can be shown that the second term on the right-hand side vanishes if the b_z profile from Eq.(D.21) is assumed. Thus,

$$③ = \overline{\frac{b_s}{s}\frac{\partial}{\partial s}(sb_\phi)} . \tag{D.65}$$

Inserting the expressions given in Eqs.(D.55), (D.59), and (D.65) into Eq.(D.45), dividing through by s, and moving the Reynolds stress term to the right-hand side gives the final expression for time evolution of the zonal angular acceleration $\frac{\overline{u_\phi}}{s}$. In terms of the individual torques,

$$\boxed{\frac{\partial}{\partial t}\left(\frac{\overline{u_\phi}}{s}\right) = \Gamma_{\mathrm{V}} + \Gamma_{\mathrm{R}} + \Gamma_{\mathrm{L}_1} + \Gamma_{\mathrm{L}_2}} , \tag{D.66}$$

where

$$\boxed{\begin{aligned} \Gamma_{\mathrm{V}} &= \frac{E}{s^3 L}\frac{\partial}{\partial s}\left(s^3 L\frac{\partial}{\partial s}\left(\frac{\overline{u_\phi}}{s}\right)\right) , \quad \Gamma_{\mathrm{R}} = -\overline{\frac{u_s}{s^2}\frac{\partial}{\partial s}(su_\phi)} \\ \Gamma_{\mathrm{L}_1} &= \frac{1}{s^3 L}\frac{\partial}{\partial s}\left(s^3 L B_{0s}\left(\frac{\overline{b_\phi}}{s}\right)\right) , \quad \Gamma_{\mathrm{L}_2} = \overline{\frac{b_s}{s^2}\frac{\partial}{\partial s}(sb_\phi)} . \end{aligned}} \tag{D.67}$$

D.3 Temperature Equation

D.3.1 Background Profile

As discussed in Section 2.3.5, the temperature field T is decomposed into a steady, conducting profile T_0 and an axially-averaged perturbation Θ. Since it will be shown that $\langle T_0 \rangle$ depends only on s (see Eq.(D.83)),

$$T(t, s, \phi) = \langle T_0 \rangle (s) + \Theta(t, s, \phi) \,. \tag{D.68}$$

T_0 is calculated from the temperature equation itself, Eq.(C.17). Because T_0 does not depend on time, the temperature equation reduces to Laplace's equation in the absence of a velocity field. In spherical coordinates,

$$\frac{E}{P_r} \nabla^2 T_0 = \frac{1}{r^2} \frac{E}{P_r} \frac{\partial}{\partial r} \left(r^2 \frac{\partial T_0}{\partial r} \right) + \frac{1}{r^2 \sin\theta} \frac{\partial}{\partial \theta} \left(\sin\theta \frac{\partial}{\partial \theta} T_0 \right) + \frac{1}{r^2 \sin^2\theta} \frac{\partial^2 T_0}{\partial \phi^2} = 0 \,. \tag{D.69}$$

This equation can be solved by separation of variables. It turns out that the solution is spherically symmetric: the θ- and ϕ-components must be equal to arbitrary constants for the solution to remain periodic in azimuth and bounded in latitude. The radial component is

$$\frac{1}{r^2} \frac{E}{P_r} \frac{\partial}{\partial r} \left(r^2 \frac{\partial T_0}{\partial r} \right) = 0 \quad \Rightarrow \quad T_0 = C_2 - \frac{C_1}{r} = C_2 - \frac{C_1}{\sqrt{s^2 + z^2}} \,, \tag{D.70}$$

where C_1 and C_2 are constants dependent upon the boundary conditions, with the constants from the θ and ϕ components being contained within C_2. If the inner and outer spheres are held at constant temperatures,

$$T_0(r_1) = T_1 = C_2 - \frac{C_1}{r_1}\,, \tag{D.71}$$

$$T_0(r_2) = T_2 = C_2 - \frac{C_1}{r_2}\,. \tag{D.72}$$

Since $\Delta T = T_1 - T_2$,

$$\Delta T = C_1\left(\frac{1}{r_2} - \frac{1}{r_1}\right) \quad \Rightarrow \quad C_1 = \Delta T \frac{r_1 r_2}{r_1 - r_2} \tag{D.73}$$

and

$$T_2 = C_2 - \frac{C_1}{r_2} \quad \Rightarrow \quad C_2 = T_2 + \frac{C_1}{r_2}\,. \tag{D.74}$$

D.3.2 Axial Averaging

The temperature field only enters the momentum equations through an axially-averaged azimuthal derivative of Θ in Eq.(D.22). This means that adapting the temperature equation to the QG framework is a (relatively) simple matter of calculating *its* axial average. That is, we calculate the axial average of Eq.(C.17):

$$\left\langle \frac{\partial}{\partial t} T \right\rangle = \left\langle -\mathbf{u}\cdot(\boldsymbol{\nabla} T) + \frac{E}{P_r}\nabla^2 T \right\rangle\,. \tag{D.75}$$

T is decomposed into $T = T_0 + \Theta$, as discussed previously. T_0 is time-independent, so it disappears from the time derivative. $\nabla^2 T_0 = 0$, so the T_0 contribution also disappears from the diffusion term:

$$\frac{\partial}{\partial t}\Theta = -\left\langle (\mathbf{u}\cdot\boldsymbol{\nabla})\,(T_0 + \Theta)\right\rangle + \left\langle \frac{E}{P_r}\nabla^2\Theta \right\rangle \tag{D.76}$$

The horizontal (s, ϕ) components of the velocity field are assumed to be rigid, so they can be brought outside the axial averages. Because temperature perturbations are caused by rigid

flows, Θ itself is assumed to be rigid[2], so its z-derivative is zero. Its rigidity also causes the axial average of the diffusion term to become a transform into a simple horizontal Laplace operator (Eq.(A.65)). T_0 does not depend on ϕ, causing its derivative in that direction to disappear:

$$\frac{\partial}{\partial t}\Theta = -u_s\left\langle\frac{\partial}{\partial s}T_0\right\rangle - \left\langle u_z\frac{\partial}{\partial z}T_0\right\rangle - u_s\left\langle\frac{\partial}{\partial s}\Theta\right\rangle - \frac{u_\phi}{s}\left\langle\frac{\partial}{\partial\phi}\Theta\right\rangle + \frac{E}{P_r}\nabla_H^2\Theta\,. \tag{D.77}$$

From Eq.(D.20), $u_z = \beta u_s z$, allowing the second term on the right-hand-side to be rewritten in terms of u_s, with both u_s and β coming outside the axial-averaging operator because of their lack of dependence on z. Θ's rigidity causes both its radial and azimuthal terms to remain unchanged upon axial averaging:

$$\frac{\partial}{\partial t}\Theta = -u_s\left\langle\frac{\partial}{\partial s}T_0\right\rangle - u_s\beta\left\langle z\frac{\partial}{\partial z}T_0\right\rangle - u_s\frac{\partial}{\partial s}\Theta - \frac{u_\phi}{s}\frac{\partial}{\partial\phi}\Theta + \frac{E}{P_r}\nabla_H^2\Theta\,. \tag{D.78}$$

Because T_0 is symmetric across the equator, the first term on the right-hand side may be evaluated with Eq.(A.36). The second may be integrated by parts:

$$\frac{\partial}{\partial t}\Theta = -u_s\left(\frac{\partial}{\partial s}\langle T_0\rangle + \beta\left(\langle T_0\rangle - T_0|_{z=L}\right)\right) - \frac{\beta u_s}{2L}\left((zT_0)|_{z=-L}^{L} - \int_{-L}^{L}T_0\,\mathrm{d}z\right) - \mathbf{u}_H\cdot(\boldsymbol{\nabla}_H\Theta) + \frac{E}{P_r}\nabla_H^2\Theta\,. \tag{D.79}$$

The $z = L$ surface is, in practice, the $r = r_2$ surface upon which the temperature is held at T_2. The z-integral of T_0, meanwhile, can be rewritten as $\langle T_0\rangle$:

$$\frac{\partial}{\partial t}\Theta = -u_s\left(\frac{\partial}{\partial s}\langle T_0\rangle + \beta\left(\langle T_0\rangle - T_1\right)\right) - \beta u_s\left(T_1 - \langle T_0\rangle\right) - \mathbf{u}_H\cdot(\boldsymbol{\nabla}_H\Theta) + \frac{E}{P_r}\nabla_H^2\Theta\,. \tag{D.80}$$

[2]This is not *quite* compatible with the boundary condition that $\Theta = 0$ on the inner and outer boundaries, since the outer boundary in three dimensions is the $r = r_2$ surface. It is reasonable, however, if the axial averaging is done between the bottom of thermal boundary layers at $z = \pm L$, above which Θ rapidly drops to zero.

The β-terms cancel, leaving

$$\boxed{\frac{\partial \Theta}{\partial t} = -u_s \frac{\partial}{\partial s} \langle T_0 \rangle - \mathbf{u}_H \cdot (\boldsymbol{\nabla}_H \Theta) + \frac{E}{P_r} \nabla_H^2 \Theta} \,. \tag{D.81}$$

The $\frac{\partial}{\partial s} T_0$ term of Eq.(D.81) may be calculated *a priori* from Eq.(D.70). First, $\langle T_0 \rangle$ is

$$\langle T_0 \rangle = \frac{1}{2L} \int_{z=-L}^{L} \left(C_2 - \frac{C_1}{\sqrt{s^2 + z^2}} \right) \mathrm{d}z = C_2 - \frac{C_1}{2L} \int_{z=-L}^{L} \frac{1}{\sqrt{s^2 + z^2}} \, \mathrm{d}z \,. \tag{D.82}$$

Taking advantage of T_0's equatorial symmetry,

$$\langle T_0 \rangle = C_2 - \frac{C_1}{L} \ln \left(\sqrt{s^2 + z^2} + z \right) \Big|_{z=0}^{L} \quad \Rightarrow \quad \langle T_0 \rangle = C_2 - \frac{C_1}{L} \sinh^{-1} \left(\frac{L}{s} \right) . \tag{D.83}$$

The s-derivative of $\langle T_0 \rangle$ is then

$$\frac{\partial}{\partial s} \langle T_0 \rangle = -C_1 \frac{s}{L^2} \left(\frac{1}{L} \sinh^{-1} \left(\frac{L}{s} \right) - \frac{1}{s^2} \right) . \tag{D.84}$$

Using the definition of C_1 from Eq.(D.74),

$$\frac{\partial}{\partial s} \langle T_0 \rangle = \Delta T \frac{r_1 r_2}{r_1 - r_2} \beta \left(\frac{1}{L} \sinh^{-1} \left(\frac{L}{s} \right) - \frac{1}{s^2} \right) . \tag{D.85}$$

The value of this expression is always negative, which may be emphasized by factoring out a negative sign on the right-hand side. Since this model uses r_2 to nondimensionalize lengths, the radial derivative of the background temperature field is

$$\boxed{\frac{\partial}{\partial s} \langle T_0 \rangle = -\Delta T \frac{r_1}{1 - r_1} \beta \left(\frac{1}{L} \sinh^{-1} \left(\frac{L}{s} \right) - \frac{1}{s^2} \right)} . \tag{D.86}$$

D.4 Induction Equation

As outlined in Section 2.3.2, the nonaxisymmetric magnetic perturbation field $\mathbf{b}$ is written in terms of a magnetic potential a, so that

$$\mathbf{b} = \overline{b_\phi}\mathbf{e}_\phi + \frac{1}{L}\boldsymbol{\nabla} \times (La\mathbf{e}_z) \; . \tag{D.87}$$

The induction equation may therefore also be written in terms of a. To begin, the radial component of Eq.(C.18) is extracted. Since only the perturbation ($\mathbf{b}$) part of the full magnetic field ($\mathbf{B} = \mathbf{B}_0 + \mathbf{b}$) changes with time,

$$\frac{\partial b_s}{\partial t} = \frac{1}{s}\frac{\partial}{\partial \phi}\left(u_s B_\phi - u_\phi B_s\right) - \frac{\partial}{\partial z}\left(u_z B_s - u_s B_z\right) + \frac{E}{P_m}\left(\nabla^2 b_s - \frac{b_s}{s^2} - \frac{2}{s^2}\frac{\partial b_\phi}{\partial \phi}\right) . \tag{D.88}$$

In terms of a, b_s and b_ϕ are

$$b_s = \frac{1}{s}\frac{\partial a}{\partial \phi}, \quad b_\phi = -\left(\frac{\partial}{\partial s} + \beta\right) a \, . \tag{D.89}$$

Using these definitions in the diffusion term of Eq.(D.88),

$$\nabla^2 b_s - \frac{b_s}{s^2} - \frac{2}{s^2}\frac{\partial b_\phi}{\partial \phi} = \left(\frac{\partial^2}{\partial s^2} + \frac{1}{s}\frac{\partial}{\partial s} + \frac{1}{s^2}\frac{\partial^2}{\partial \phi^2} + \frac{\partial^2}{\partial z^2}\right)\left(\frac{1}{s}\frac{\partial a}{\partial \phi}\right) \tag{D.90}$$

$$- \frac{1}{s^2}\left(\frac{1}{s}\frac{\partial a}{\partial \phi}\right) - \frac{2}{s^2}\frac{\partial}{\partial \phi}\left(-\frac{\partial a}{\partial s} - \beta a\right) . \tag{D.91}$$

With the recognition that ϕ-derivatives commute with all other derivatives and with factors of s, this simplifies to

$$\nabla^2 b_s - \frac{b_s}{s^2} - \frac{2}{s^2}\frac{\partial b_\phi}{\partial \phi} = \frac{1}{s}\frac{\partial}{\partial \phi}\left(\left(\frac{\partial^2}{\partial s^2} + \frac{1}{s}\frac{\partial}{\partial s} + \frac{1}{s^2}\frac{\partial^2}{\partial \phi^2} + \frac{\partial^2}{\partial z^2}\right) a + \frac{2\beta a}{s}\right) \tag{D.92}$$

$$= \frac{1}{s}\frac{\partial}{\partial \phi}\left(\nabla^2 a + \frac{2\beta a}{s}\right) . \tag{D.93}$$

Substituting this into Eq.(D.88) and writing the time derivative in terms of a results in

$$\frac{1}{s}\frac{\partial}{\partial \phi}\left(\frac{\partial a}{\partial t}\right) = \frac{1}{s}\frac{\partial}{\partial \phi}\left(u_s B_\phi - u_\phi B_s\right) - \frac{\partial}{\partial z}\left(u_z B_s - u_s B_z\right) + \frac{1}{s}\frac{\partial}{\partial \phi}\left(\frac{E}{P_m}\left(\nabla^2 a + \frac{2\beta a}{s}\right)\right) . \tag{D.94}$$

Next, the axial average of Eq.(D.94) is calculated. The average of the axial derivative term is

$$\left\langle \frac{\partial}{\partial z}\left(u_z B_s - u_s B_z\right)\right\rangle = \frac{1}{2L}\left(u_z B_s - u_s B_z\right)\Big|_{z=-L}^{L} . \tag{D.95}$$

As shown in Eqs.(D.20) and (D.21), the no-penetration boundary condition and the assumption of $a = 0$ on the boundaries justifies the assumption of an axial velocity field and total axial magnetic field with forms $u_z = \beta u_s z$ and $B_z = \beta B_s z$, respectively. Substituting these profiles into Eq.(D.95),

$$\left\langle \frac{\partial}{\partial z}\left(u_z B_s - u_s B_z\right)\right\rangle = \frac{1}{2L}\left(\left(\beta u_s z\right) B_s - u_s\left(\beta B_s z\right)\right)\Big|_{z=-L}^{L} = 0 . \tag{D.96}$$

The axial average of Eq.(D.94) is therefore

$$\frac{1}{s}\frac{\partial}{\partial \phi}\left\langle \frac{\partial a}{\partial t}\right\rangle = \frac{1}{s}\frac{\partial}{\partial \phi}\left\langle u_s B_\phi - u_\phi B_s\right\rangle + \frac{1}{s}\frac{\partial}{\partial \phi}\left\langle \frac{E}{P_m}\left(\nabla^2 a + \frac{2\beta a}{s}\right)\right\rangle . \tag{D.97}$$

Because the magnetic potential function must be periodic in azimuth, and Eq.(D.97) will only be used to calculate the non-axisymmetric a (see Chapter 2), the ϕ-derivatives may be

dropped from Eq.(D.97). Then, assuming u_s, u_ϕ, B_s, B_ϕ, and a are rigid,

$$\frac{\partial a}{\partial t} = (u_s B_\phi - u_\phi B_s) + \frac{E}{P_m}\left(\langle \nabla^2 a \rangle + \frac{2\beta a}{s}\right), \tag{D.98}$$

where variables without angled braces are assumed to be axial averages. The value of $\langle \nabla^2 a \rangle$, however, depends on the behaviour of a at the upper and lower boundaries. If a is assumed to be symmetric across the equator, and if axial averaging is performed only between the electromagnetic skin layers present at the boundaries (so that $a|_{z=L} = a|_{z=-L} = \langle a \rangle$), Eq.(A.65) shows that $\langle \nabla^2 a \rangle = \nabla_H^2 \langle a \rangle$. Substituting this into Eq.(D.98) results in the QG induction equation:

$$\boxed{\frac{\partial}{\partial t} a = (u_s B_\phi - u_\phi B_s) + \frac{E}{P_m}\left(\nabla_H^2 a + \frac{2\beta a}{s}\right)}. \tag{D.99}$$

D.5 Zonal Induction Equation

The zonal induction equation is derived from the $\mathbf{e}_\phi$ component of the full induction equation (Eq.(C.18)). Again, the full magnetic field is decomposed into a steady background field, $\mathbf{B}_0$, and a time-dependent perturbation, $\mathbf{b}$. It is assumed that $\nabla^2 \mathbf{B}_0 = 0$. Because $\frac{\partial B_\phi}{\partial t} = \frac{\partial b_\phi}{\partial t}$, the $\mathbf{e}_\phi$ component of Eq.(C.18) is

$$\frac{\partial b_\phi}{\partial t} = \underbrace{\frac{\partial}{\partial s}\left(\mathbf{e}_z \cdot (\mathbf{u} \times \mathbf{B})\right) + \frac{\partial}{\partial z}\left(\mathbf{e}_s \cdot (\mathbf{u} \times \mathbf{B})\right)}_{①} + \frac{E}{P_m}\left(\nabla^2 b_\phi - \frac{b_\phi}{s^2} + \frac{2}{s^2}\frac{\partial b_s}{\partial \phi}\right). \tag{D.100}$$

① expands into

$$① = -\frac{\partial}{\partial s}\left(u_s B_\phi - u_\phi B_s\right) + \frac{\partial}{\partial z}\left(u_\phi B_z - u_z B_\phi\right). \tag{D.101}$$

The z-derivative of the second term may be distributed:

$$① = \frac{\partial}{\partial s}\left(u_\phi B_s - u_s B_\phi\right) + u_\phi \frac{\partial}{\partial z} B_z - B_\phi \frac{\partial}{\partial z} u_z + B_z \frac{\partial}{\partial z} u_\phi - u_z \frac{\partial}{\partial z} B_\phi \,. \tag{D.102}$$

The final two terms vanish, since u_ϕ and B_ϕ are assumed to be rigid – that is, z-invariant. The remaining z-derivatives may be replaced with functions based on the axial profiles assumed for u_z (Eq.(2.21)) and B_z ($B_z = \beta B_s z$):

$$① = \frac{\partial}{\partial s}\left(u_\phi B_s - u_s B_\phi\right) + u_\phi \left(\beta B_s\right) - B_\phi \left(\beta u_s\right) \,. \tag{D.103}$$

Thus, with some rearranging,

$$① = -\left(\frac{\partial}{\partial s} + \beta\right)\left(u_s B_\phi - u_\phi B_s\right) \,. \tag{D.104}$$

Substituting this expression into Eq.(D.100),

$$\frac{\partial b_\phi}{\partial t} = -\left(\frac{\partial}{\partial s} + \beta\right)\left(u_s B_\phi - u_\phi B_s\right) + \frac{E}{P_m}\left(\nabla^2 b_\phi - \frac{b_\phi}{s^2} + \frac{2}{s^2}\frac{\partial b_s}{\partial \phi}\right) \,. \tag{D.105}$$

Azimuthally averaging,

$$\frac{\partial \overline{b_\phi}}{\partial t} = -\left(\frac{\partial}{\partial s} + \beta\right)\left(\overline{u_s B_\phi} - \overline{u_\phi B_s}\right) + \frac{E}{P_m}\left(\overline{\nabla^2 b_\phi} - \frac{\overline{b_\phi}}{s^2} + \frac{2}{s^2}\overline{\frac{\partial b_s}{\partial \phi}}\right) \,. \tag{D.106}$$

Both b_s and b_ϕ are periodic in azimuth, so terms involving their azimuthal derivatives vanish:

$$\frac{\partial \overline{b_\phi}}{\partial t} = -\left(\frac{\partial}{\partial s} + \beta\right)\left(\overline{u_s B_\phi} - \overline{u_\phi B_s}\right) + \frac{E}{P_m}\left(\nabla^2_{s,z}\overline{b_\phi} - \frac{\overline{b_\phi}}{s^2}\right) \,, \tag{D.107}$$

where $\nabla^2_{s,z}$ are the s- and z-derivative terms of the gradient operator. As in the previous section, the axial average of Eq.(D.107) is taken to occur between the boundary layers and electromagnetic skin layers at the top and bottom boundaries, so that the magnetic and velocity fields there are the same as their rigid values. Under this assumption, and

understanding that variables not within angled brackets have been axially averaged,

$$\overline{\frac{\partial \overline{b_\phi}}{\partial t}} = \frac{\partial \overline{b_\phi}}{\partial t} = -\left(\frac{\partial}{\partial s} + \beta\right)\left(\overline{u_s B_\phi} - \overline{u_\phi B_s}\right) + \underbrace{\frac{E}{P_m}\left(\nabla_s^2 \overline{b_\phi} - \frac{\overline{b_\phi}}{s^2}\right)}_{②}, \tag{D.108}$$

where ∇_s^2 are the radial derivative terms of the gradient operator. The viscous term (②) may be expanded as

$$② = \left(\nabla_s^2 - \frac{1}{s^2}\right)\overline{b_\phi} = \left(\frac{\partial^2}{\partial s^2} + \frac{1}{s}\frac{\partial}{\partial s} - \frac{1}{s^2}\right)\overline{b_\phi}\,. \tag{D.109}$$

Using Eq.(A.16), this can be written in terms of $\frac{\overline{b_\phi}}{s}$ as

$$② = \left(s\left(\frac{\partial^2}{\partial s^2} + \frac{2}{s}\frac{\partial}{\partial s}\right) + \frac{\partial}{\partial s}\right)\left(\frac{\overline{b_\phi}}{s}\right) = s\left(\frac{\partial}{\partial s} + \frac{3}{s}\right)\frac{\partial}{\partial s}\left(\frac{\overline{b_\phi}}{s}\right)\,. \tag{D.110}$$

Finally, invoking Eq.(A.14),

$$② = \frac{1}{s^2}\frac{\partial}{\partial s}\left(s^3 \frac{\partial}{\partial s}\left(\frac{\overline{b_\phi}}{s}\right)\right)\,. \tag{D.111}$$

Substituting this back into Eq.(D.108) and dividing through by s gives the final zonal induction equation:

$$\boxed{\frac{\partial}{\partial t}\left(\frac{\overline{b_\phi}}{s}\right) = -\frac{1}{s}\left(\frac{\partial}{\partial s} + \beta\right)\left(\overline{u_s B_\phi} - \overline{u_\phi B_s}\right) + \frac{1}{s^3}\frac{E}{P_m}\frac{\partial}{\partial s}\left(s^3\frac{\partial}{\partial s}\left(\frac{\overline{b_\phi}}{s}\right)\right)}\,. \tag{D.112}$$

Appendix E

Axisymmetric Multiplication in Fourier Space

Eq.(A.79) (Appendix A.5) shows how the azimuthally averaged product of two functions represented by Fourier series may be calculated in Fourier space. There are three terms in the model's governing equations which require such a calculation: the Γ_R and Γ_{L_2} torques in the zonal flow equation (2.36), and the nonlinear terms of the induction equation (2.42). They will be handled individually in this appendix.

E.1 Γ_R - Reynolds Torque

Because the streamfunction ψ is decomposed into azimuthal Fourier modes within the model, for a particular Fourier mode m the radial ($u_{s,m}$) and azimuthal ($u_{\phi,m}$) components of the nonaxisymmetric velocity field may be written in terms of the corresponding streamfunction component ψ_m:

$$u_{s,m} = \frac{1}{s}\frac{\partial \psi_m}{\partial \phi} = \frac{im}{s}\psi_m \,, \tag{E.1}$$

$$u_{\phi,m} = -\left(\frac{\partial}{\partial s} + \beta\right)\psi_m \,, \tag{E.2}$$

where i is the imaginary unit. The Reynolds torque Γ_{R} is given in Eq.(2.38) as

$$\Gamma_{\mathrm{R}} = -\frac{1}{s^2}\left(\overline{u_s \frac{\partial}{\partial s}\left(s u_\phi\right)}\right) \,, \tag{E.3}$$

where the overbar indicates an azimuthal average. Using Eq.(A.79), the azimuthal average is

$$\overline{\left(u_s\right)\left(\frac{\partial}{\partial s}\left(s u_\phi\right)\right)} = \left(\overline{u_s}\right)\left(\overline{\frac{\partial}{\partial s}\left(s u_\phi\right)}\right) + 2\sum_{m=1}^{\infty}\left(\Re\left(u_{s,m}\right)\Re\left(\frac{\partial}{\partial s}\left(s u_{\phi,m}\right)\right) + \Im\left(u_{s,m}\right)\Im\left(\frac{\partial}{\partial s}\left(s u_{\phi,m}\right)\right)\right) \,, \tag{E.4}$$

where $\Re$ and $\Im$ are the real and imaginary operators, respectively. Because u_s does not have an axisymmetric part, the first term on the right-hand side vanishes. Writing $u_{s,m}$ in terms of ψ_m, the azimuthal average becomes

$$\overline{\left(u_s\right)\left(\frac{\partial}{\partial s}\left(s u_\phi\right)\right)} = 2\sum_{m=1}^{\infty}\left(\Re\left(\frac{im}{s}\psi_m\right)\Re\left(\frac{\partial}{\partial s}\left(s u_{\phi,m}\right)\right) + \Im\left(\frac{im}{s}\psi_m\right)\Im\left(\frac{\partial}{\partial s}\left(s u_{\phi,m}\right)\right)\right) \tag{E.5}$$

$$= \frac{2}{s}\sum_{m=1}^{\infty} m\left(-\Im\left(\psi_m\right)\Re\left(\frac{\partial}{\partial s}\left(s u_{\phi,m}\right)\right) + \Re\left(\psi_m\right)\Im\left(\frac{\partial}{\partial s}\left(s u_{\phi,m}\right)\right)\right) \,. \tag{E.6}$$

Defining

$$\alpha_m = -\frac{1}{s}\frac{\partial}{\partial s}\left(s u_{\phi,m}\right) = \left(\frac{\partial^2}{\partial s^2} + \left(\beta + \frac{1}{s}\right)\frac{\partial}{\partial s} + \left(\frac{\beta}{s} + \frac{\partial \beta}{\partial s}\right)\right)\psi_m \,, \tag{E.7}$$

Eq.(E.6) becomes

$$\overline{\left(u_s\right)\left(\frac{\partial}{\partial s}\left(s u_\phi\right)\right)} = \frac{2}{s}\sum_{m=1}^{\infty} m\left(-\Im\left(\psi_m\right)\Re\left(-s\alpha_m\right) + \Re\left(\psi_m\right)\Im\left(-s\alpha_m\right)\right) \tag{E.8}$$

$$= 2\sum_{m=1}^{\infty} m\left(\Im\left(\psi_m\right)\Re\left(\alpha_m\right) - \Re\left(\psi_m\right)\Im\left(\alpha_m\right)\right) \,. \tag{E.9}$$

Then, absorbing the Reynolds torque's negative sign into Eq.(E.9),

$$\boxed{\begin{aligned} &\Gamma_{\mathrm{R}} = \frac{2}{s^2}\sum_{m=1}^{\infty} m\left(\Re\left(\psi_m\right)\Im\left(\alpha_m\right) - \Im\left(\psi_m\right)\Re\left(\alpha_m\right)\right) \,, \\ &\text{where} \quad \alpha_m = \left(\frac{\partial^2}{\partial s^2} + \left(\beta + \frac{1}{s}\right)\frac{\partial}{\partial s} + \left(\frac{\beta}{s} + \frac{\partial \beta}{\partial s}\right)\right)\psi_m \,. \end{aligned}} \tag{E.10}$$

E.2 $\Gamma_{\mathbf{L}_2}$ - Maxwell Torque

The Maxwell torque term is very similar in form to the Reynolds torque. Like the stream-function ψ, the magnetic potential function a is decomposed within the model in terms of azimuthal Fourier modes. Thus, for a given Fourier mode m, the radial ($b_{s,m}$) and azimuthal ($b_{\phi,m}$) components of the nonaxisymmetric magnetic perturbation field may be written in terms of the corresponding potential function component a_m as

$$b_{s,m} = \frac{1}{s}\frac{\partial a_m}{\partial \phi} = \frac{im}{s}a_m \,, \tag{E.11}$$

$$b_{\phi,m} = -\left(\frac{\partial}{\partial s} + \beta\right)a_m \,. \tag{E.12}$$

The Maxwell torque Γ_{L_2} is given in Eq.(2.40) as

$$\Gamma_{\mathrm{L}_2} = \frac{1}{s^2}\left(\overline{b_s \frac{\partial}{\partial s}\left(s b_\phi\right)}\right) . \tag{E.13}$$

Using Eq.(A.79), the azimuthal average is

$$\overline{\left(b_s\right)\left(\frac{\partial}{\partial s}\left(s b_\phi\right)\right)} = \left(\overline{b_s}\right)\left(\overline{\frac{\partial}{\partial s}\left(s b_\phi\right)}\right) + 2\sum_{m=1}^{\infty}\left(\Re\left(b_{s,m}\right)\Re\left(\frac{\partial}{\partial s}\left(s b_{\phi,m}\right)\right) + \Im\left(b_{s,m}\right)\Im\left(\frac{\partial}{\partial s}\left(s b_{\phi,m}\right)\right)\right) . \tag{E.14}$$

Like u_s, b_s does not have an axisymmetric component, causing the first term on the right-hand side to vanish. Writing $b_{s,m}$ in terms of a_m, the azimuthal average becomes

$$\overline{\left(b_s\right)\left(\frac{\partial}{\partial s}\left(s b_\phi\right)\right)} = 2\sum_{m=1}^{\infty}\left(\Re\left(\frac{im}{s}a_m\right)\Re\left(\frac{\partial}{\partial s}\left(s b_{\phi,m}\right)\right) + \Im\left(\frac{im}{s}a_m\right)\Im\left(\frac{\partial}{\partial s}\left(s b_{\phi,m}\right)\right)\right) \tag{E.15}$$

$$= \frac{2}{s}\sum_{m=1}^{\infty} m\left(-\Im\left(a_m\right)\Re\left(\frac{\partial}{\partial s}\left(s b_{\phi,m}\right)\right) + \Re\left(a_m\right)\Im\left(\frac{\partial}{\partial s}\left(s b_{\phi,m}\right)\right)\right) . \tag{E.16}$$

Defining

$$\gamma_m = -\frac{1}{s}\frac{\partial}{\partial s}\left(s b_{\phi,m}\right) = \left(\frac{\partial^2}{\partial s^2} + \left(\beta + \frac{1}{s}\right)\frac{\partial}{\partial s} + \left(\frac{\beta}{s} + \frac{\partial \beta}{\partial s}\right)\right) a_m , \tag{E.17}$$

Eq.(E.16) becomes

$$\overline{\left(b_s\right)\left(\frac{\partial}{\partial s}\left(s b_\phi\right)\right)} = \frac{2}{s}\sum_{m=1}^{\infty} m\left(-\Im\left(a_m\right)\Re\left(-s\gamma_m\right) + \Re\left(a_m\right)\Im\left(-s\gamma_m\right)\right) \tag{E.18}$$

$$= 2\sum_{m=1}^{\infty} m\left(\Im\left(a_m\right)\Re\left(\gamma_m\right) - \Re\left(a_m\right)\Im\left(\gamma_m\right)\right) . \tag{E.19}$$

Thus, the Maxwell torque is

$$\boxed{\begin{aligned}&\Gamma_{\mathrm{L}_2} = \frac{2}{s^2}\sum_{m=1}^{\infty} m\left(\Im\left(a_m\right)\Re\left(\gamma_m\right) - \Re\left(a_m\right)\Im\left(\gamma_m\right)\right)\,,\\ &\text{where}\quad \gamma_m = \left(\frac{\partial^2}{\partial s^2} + \left(\beta + \frac{1}{s}\right)\frac{\partial}{\partial s} + \left(\frac{\beta}{s} + \frac{\partial \beta}{\partial s}\right)\right) a_m\,.\end{aligned}} \tag{E.20}$$

E.3 Zonal Induction Equation

The azimuthally-averaged product G of the nonaxisymmetric velocity and magnetic perturbation fields in the zonal induction equation (Eq.(2.42)) is

$$G = \frac{1}{sL}\frac{\partial}{\partial s}\left(\overline{u_\phi\left(Lb_s\right)} - \overline{u_s\left(Lb_\phi\right)}\right)\,. \tag{E.21}$$

Expanding the radial derivatives and rearranging,

$$G = \frac{1}{s}\left(\overline{b_s\frac{\partial}{\partial s}u_\phi} - \overline{\frac{b_\phi}{L}\frac{\partial}{\partial s}\left(Lu_s\right)} - \overline{u_s\frac{\partial}{\partial s}b_\phi} + \overline{\frac{u_\phi}{L}\frac{\partial}{\partial s}\left(Lb_s\right)}\right)\,. \tag{E.22}$$

For a function f, $\frac{1}{s}\frac{\partial}{\partial s}\left(sf\right) = \frac{\partial}{\partial s}f + \frac{f}{s}$. So,

$$\begin{aligned}G = \;& \frac{1}{s}\left(\overline{b_s\frac{\partial}{\partial s}u_\phi} - \overline{\frac{b_\phi}{L}\left(\frac{\partial}{\partial s}\left(Lu_s\right) + \frac{Lu_s}{s}\right)} + \overline{\frac{b_\phi u_s}{s}}\right.\\ &\left. - \overline{u_s\frac{\partial}{\partial s}b_\phi} + \overline{\frac{u_\phi}{L}\left(\frac{\partial}{\partial s}\left(Lb_s\right) + \frac{Lb_s}{s}\right)} - \overline{\frac{u_\phi b_s}{s}}\right)\end{aligned} \tag{E.23}$$

$$\begin{aligned}\Rightarrow G = \;& \frac{1}{s}\left(\overline{b_s\frac{\partial}{\partial s}u_\phi} - \overline{\frac{b_\phi}{sL}\frac{\partial}{\partial s}\left(sLu_s\right)} + \overline{\frac{b_\phi u_s}{s}}\right.\\ &\left. - \overline{u_s\frac{\partial}{\partial s}b_\phi} + \overline{\frac{u_\phi}{sL}\frac{\partial}{\partial s}\left(sLb_s\right)} - \overline{\frac{u_\phi b_s}{s}}\right)\,.\end{aligned} \tag{E.24}$$

From continuity,

$$\boldsymbol{\nabla}\cdot\mathbf{b}=\frac{1}{s}\frac{\partial}{\partial s}\left(sb_s\right)+\frac{1}{s}\frac{\partial}{\partial\phi}b_\phi+\frac{\partial}{\partial z}b_z=0\quad\text{and}\quad\boldsymbol{\nabla}\cdot\mathbf{u}=\frac{1}{s}\frac{\partial}{\partial s}\left(su_s\right)+\frac{1}{s}\frac{\partial}{\partial\phi}u_\phi+\frac{\partial}{\partial z}u_z=0\,. \tag{E.25}$$

Since it is assumed that $b_z=\beta b_s z$ and $u_z=\beta u_s z$, rearranging the above gives

$$\frac{1}{s}\frac{\partial}{\partial\phi}b_\phi=-\frac{1}{s}\frac{\partial}{\partial s}\left(sb_s\right)-\beta b_s\quad\text{and}\quad\frac{1}{s}\frac{\partial}{\partial\phi}u_\phi=-\frac{1}{s}\frac{\partial}{\partial s}\left(su_s\right)-\beta u_s\,. \tag{E.26}$$

Combining the terms on each right-hand side,

$$\frac{1}{s}\frac{\partial}{\partial\phi}b_\phi=-\frac{1}{sL}\frac{\partial}{\partial s}\left(sLb_s\right)\quad\text{and}\quad\frac{1}{s}\frac{\partial}{\partial\phi}u_\phi=-\frac{1}{sL}\frac{\partial}{\partial s}\left(sLu_s\right)\,. \tag{E.27}$$

Using these expressions, Eq.(E.24) becomes

$$G=\frac{1}{s}\left(\overline{b_s\frac{\partial}{\partial s}u_\phi}+\overline{\frac{b_\phi}{s}\frac{\partial}{\partial\phi}u_\phi}+\overline{\frac{b_\phi u_s}{s}}-\overline{u_s\frac{\partial}{\partial s}b_\phi}-\overline{\frac{u_\phi}{s}\frac{\partial}{\partial\phi}b_\phi}-\overline{\frac{u_\phi b_s}{s}}\right)\,. \tag{E.28}$$

So,

$$G=\underbrace{\frac{1}{s}\left(\overline{b_s\frac{\partial}{\partial s}u_\phi}-\overline{\frac{b_s u_\phi}{s}}\right)}_{①}-\underbrace{\frac{1}{s}\left(\overline{u_s\frac{\partial}{\partial s}b_\phi}-\overline{\frac{u_s b_\phi}{s}}\right)}_{②}+\underbrace{\frac{1}{s^2}\left(\overline{b_\phi\frac{\partial}{\partial\phi}u_\phi}-\overline{u_\phi\frac{\partial}{\partial\phi}b_\phi}\right)}_{③}\,. \tag{E.29}$$

First Term

Writing the variables in ① in terms of the stream and magnetic potential functions,

$$
\begin{aligned}
b_s^m &\equiv \frac{1}{s}\frac{\partial a^m}{\partial \phi} = im\frac{a^m}{s}\,, \\
u_\phi^m &\equiv -\left(\frac{\partial}{\partial s}+\beta\right)\psi^m\,, \\
\frac{\partial}{\partial s}u_\phi^m &= -\left(\frac{\partial^2}{\partial s^2}+\beta\frac{\partial}{\partial s}+\frac{\partial \beta}{\partial s}\right)\psi^m\,.
\end{aligned}
$$

Thus, using Eq.(A.79), ① may be expanded as a sum. Because the radial perturbation field has no axisymmetric mode, the first term of the sum disappears:

$$
\begin{aligned}
① &= \frac{2}{s}\sum_{m=1}^{\infty}\left\{\Re\left(b_s^m\right)\Re\left(\frac{\partial}{\partial s}u_\phi^m-\frac{u_\phi^m}{s}\right)+\Im\left(b_s^m\right)\Im\left(\frac{\partial}{\partial s}u_\phi^m-\frac{u_\phi^m}{s}\right)\right\} \\
&= \frac{2}{s}\sum_{m=1}^{\infty}\left\{\Re\left(im\frac{a^m}{s}\right)\Re\left(-\left(\frac{\partial^2}{\partial s^2}+\beta\frac{\partial}{\partial s}+\frac{\partial\beta}{\partial s}\right)\psi^m+\frac{1}{s}\left(\frac{\partial}{\partial s}+\beta\right)\psi^m\right)\right. \\
&\qquad \left.+\Im\left(im\frac{a^m}{s}\right)\Im\left(-\left(\frac{\partial^2}{\partial s^2}+\beta\frac{\partial}{\partial s}+\frac{\partial\beta}{\partial s}\right)\psi^m+\frac{1}{s}\left(\frac{\partial}{\partial s}+\beta\right)\psi^m\right)\right\} \\
&= \frac{2}{s^2}\sum_{m=1}^{\infty}m\left\{\Im\left(a^m\right)\Re\left(\left(\frac{\partial^2}{\partial s^2}+\left(\beta-\frac{1}{s}\right)\frac{\partial}{\partial s}+\left(\frac{\partial\beta}{\partial s}-\frac{\beta}{s}\right)\right)\psi^m\right)\right. \\
&\qquad \left.-\Re\left(a^m\right)\Im\left(\left(\frac{\partial^2}{\partial s^2}+\left(\beta-\frac{1}{s}\right)\frac{\partial}{\partial s}+\left(\frac{\partial\beta}{\partial s}-\frac{\beta}{s}\right)\right)\psi^m\right)\right\}
\end{aligned}
$$

Defining two dummy functions, α_1 and γ_1,

$$
① = \frac{2}{s^2}\sum_{m=1}^{\infty}m\left[\Im\left(\alpha_1^m\right)\Re\left(\gamma_1^m\right)-\Re\left(\alpha_1^m\right)\Im\left(\gamma_1^m\right)\right], \alpha_1^m = a^m, \tag{E.30}
$$

$$
\gamma_1^m = \left(\frac{\partial^2}{\partial s^2}+\left(\beta-\frac{1}{s}\right)\frac{\partial}{\partial s}+\left(\frac{\partial\beta}{\partial s}-\frac{\beta}{s}\right)\right)\psi^m \tag{E.31}
$$

Second Term

This term is similar to ①:

$$\begin{aligned} u_s^m &\equiv \frac{1}{s}\frac{\partial \psi^m}{\partial \phi} = im\frac{\psi^m}{s} \\ b_\phi^m &\equiv -\frac{\partial a^m}{\partial s} \\ \frac{\partial}{\partial s}b_\phi^m &= -\frac{\partial^2}{\partial s^2}a^m \end{aligned}$$

This time, the nonexistence of the axisymmetric radial velocity field is what causes the first term in equation A.79 to disappear when ② is written in terms of it:

$$\begin{aligned} ② &= -\frac{2}{s}\sum_{m=1}^{\infty}\left\{\Re\left(u_s^m\right)\Re\left(\frac{\partial}{\partial s}b_\phi^m - \frac{b_\phi^m}{s}\right) + \Im\left(u_s^m\right)\Im\left(\frac{\partial}{\partial s}b_\phi^m - \frac{b_\phi^m}{s}\right)\right\} \\ &= -\frac{2}{s}\sum_{m=1}^{\infty}\left\{\Re\left(im\frac{\psi^m}{s}\right)\Re\left(-\frac{\partial^2}{\partial s^2}a^m + \frac{1}{s}\frac{\partial}{\partial s}a^m\right) + \Im\left(im\frac{\psi^m}{s}\right)\Im\left(-\frac{\partial^2}{\partial s^2}a^m + \frac{1}{s}\frac{\partial}{\partial s}a^m\right)\right\} \\ &= -\frac{2}{s^2}\sum_{m=1}^{\infty} m\left\{\Im\left(\psi^m\right)\Re\left(\left(\frac{\partial^2}{\partial s^2} - \frac{1}{s}\frac{\partial}{\partial s}\right)a^m\right) - \Re\left(\psi^m\right)\Im\left(\left(\frac{\partial^2}{\partial s^2} - \frac{1}{s}\frac{\partial}{\partial s}\right)a^m\right)\right\} \end{aligned}$$

With two more dummy functions, I have

$$② = \frac{2}{s^2}\sum_{m=1}^{\infty} m\left[\Im\left(\alpha_2^m\right)\Re\left(\gamma_2^m\right) - \Re\left(\alpha_2^m\right)\Im\left(\gamma_2^m\right)\right], \qquad \alpha_2^m \equiv -\psi^m, \tag{E.32}$$

$$\gamma_2^m \equiv \left(\frac{\partial^2}{\partial s^2} - \frac{1}{s}\frac{\partial}{\partial s}\right)a^m \tag{E.33}$$

Third Term

This one is a bit different! For it, I need

$$\begin{aligned} u_\phi^m \equiv -\left(\frac{\partial}{\partial s} + \beta\right)\psi^m, \qquad \frac{\partial}{\partial \phi}u_\phi^m = imu_\phi^m \\ b_\phi^m \equiv -\frac{\partial}{\partial s}a^m, \qquad \frac{\partial b_\phi^m}{\partial \phi} = imb_\phi^m \end{aligned}$$

Both derivatives are zero for the axisymmetric mode, so again the leading term in equation A.79 disappears. Writing ③ in terms of that series gives

$$\begin{aligned}
③ &= \frac{2}{s^2}\sum_{m=1}^{\infty}\left\{\left(\Re\left(b_\phi^m\right)\Re\left(\frac{\partial}{\partial\phi}u_\phi^m\right)+\Im\left(b_\phi^m\right)\Im\left(\frac{\partial}{\partial\phi}u_\phi^m\right)\right)-\left(\Re\left(u_\phi^m\right)\Re\left(\frac{\partial}{\partial\phi}b_\phi^m\right)+\Im\left(u_\phi^m\right)\Im\left(\frac{\partial}{\partial\phi}b_\phi^m\right)\right.\right. \\
&= \frac{2}{s^2}\sum_{m=1}^{\infty}\left\{\Re\left(b_\phi^m\right)\Re\left(imu_\phi^m\right)+\Im\left(b_\phi^m\right)\Im\left(imu_\phi^m\right)-\Re\left(u_\phi^m\right)\Re\left(imb_\phi^m\right)-\Im\left(u_\phi^m\right)\Im\left(imb_\phi^m\right)\right\} \\
&= \frac{2}{s^2}\sum_{m=1}^{\infty}m\left\{-\Re\left(b_\phi^m\right)\Im\left(u_\phi^m\right)+\Im\left(b_\phi^m\right)\Re\left(u_\phi^m\right)+\Im\left(b_\phi^m\right)\Re\left(u_\phi^m\right)-\Re\left(b_\phi^m\right)\Im\left(u_\phi^m\right)\right\} \\
&= \frac{2}{s^2}\sum_{m=1}^{\infty}m\left\{2\Im\left(\frac{\partial}{\partial s}a^m\right)\Re\left(\left(\frac{\partial}{\partial s}+\beta\right)\psi^m\right)-2\Re\left(\frac{\partial}{\partial s}a^m\right)\Re\left(\left(\frac{\partial}{\partial s}+\beta\right)\psi^m\right)\right\}
\end{aligned}$$

So, using two final dummy functions,

$$③ = \frac{2}{s^2}\sum_{m=1}^{\infty}m\left[\Im\left(\alpha_3^m\right)\Re\left(\gamma_3^m\right)-\Re\left(\alpha_3^m\right)\Im\left(\gamma_3^m\right)\right], \qquad \alpha_3^m \equiv 2\frac{\partial}{\partial s}a^m, \tag{E.34}$$

$$\gamma_3^m \equiv \left(\frac{\partial}{\partial s}+\beta\right)\psi^m \tag{E.35}$$

Everything

So, the nonlinear terms of the axisymmetric induction equation may be written as:

$$\boxed{G = \frac{2}{s^2}\sum_{n=1}^{3}\sum_{m=1}^{\infty}m\left[\Im\left(\alpha_n^m\right)\Re\left(\gamma_n^m\right)-\Re\left(\alpha_n^m\right)\Im\left(\gamma_n^m\right)\right]} \tag{E.36}$$

n	α_n^m	γ_n^m
1	a^m	$\left(\frac{\partial^2}{\partial s^2}+\left(\beta-\frac{1}{s}\right)\frac{\partial}{\partial s}+\left(\frac{\partial\beta}{\partial s}-\frac{\beta}{s}\right)\right)\psi^m$
2	$-\psi^m$	$\left(\frac{\partial^2}{\partial s^2}-\frac{1}{s}\frac{\partial}{\partial s}\right)a^m$
3	$2\frac{\partial}{\partial s}a^m$	$\left(\frac{\partial}{\partial s}+\beta\right)\psi^m$

Appendix F

Conservation of Axial Angular Momentum

The total axial angular momentum $\mathcal{L}_z$ of the outer core is contained in the concentric cylinders rotating with axisymmetric angular velocity $\frac{\overline{u_\phi}}{s}$. Assuming a constant density ρ_0 (set to 1 for convenience), the time variation of $\mathcal{L}_z$ is then

$$\frac{1}{4\pi}\frac{\partial}{\partial t}\mathcal{L}_z = \int_{s_1}^{s_2} s^3 L \frac{\partial}{\partial t}\left(\frac{\overline{u_\phi}}{s}\right) \mathrm{d}s\,, \tag{F.1}$$

where s is the cylindrically radial position, L is the distance between the equatorial plane and the upper boundary in the axial direction, and t is time. As shown by Eq.(2.36), $\frac{\partial}{\partial t}\left(\frac{\overline{u_\phi}}{s}\right)$ can be decomposed into four component torques. For a function f, the linear operator $\mathcal{G}(f)$ is defined as $\mathcal{G}(f) = \int_{s_1}^{s_2} s^3 L f \,\mathrm{d}s$. Using this operator, Eq.(F.1) may be rewritten as a sum:

$$\frac{1}{4\pi}\frac{\partial}{\partial t}\mathcal{L}_z = \mathcal{G}\left(\Gamma_{\mathrm{V}}\right) + \mathcal{G}\left(\Gamma_{\mathrm{L}_1}\right) + \mathcal{G}\left(\Gamma_{\mathrm{L}_2}\right) + \mathcal{G}\left(\Gamma_{\mathrm{R}}\right)\,. \tag{F.2}$$

With the input torques

$$\Gamma_{\mathrm{V}} = \frac{E}{s^3 L}\frac{\partial}{\partial s}\left(s^3 L \frac{\partial}{\partial s}\left(\frac{\overline{u_\phi}}{s}\right)\right) , \tag{F.3}$$

$$\Gamma_{\mathrm{L_1}} = \frac{1}{s^3 L}\frac{\partial}{\partial s}\left(s^3 L B_{0s}\frac{\overline{b_\phi}}{s}\right) , \tag{F.4}$$

$$\Gamma_{\mathrm{L_2}} = \frac{1}{s}\left(\overline{\frac{b_s}{s}\frac{\partial}{\partial s}\left(s b_\phi\right)}\right) , \tag{F.5}$$

$$\Gamma_{\mathrm{R}} = -\frac{1}{s}\left(\overline{\frac{u_s}{s}\frac{\partial}{\partial s}\left(s u_\phi\right)}\right) , \tag{F.6}$$

the first two terms on the right-hand side of Eq.(F.2) reduce to $\mathcal{G}(\Gamma_{\mathrm{V}}) = s^3 L\frac{\partial}{\partial s}\left(\frac{\overline{u_\phi}}{s}\right)\Big|_{s_1}^{s_2}$ and $\mathcal{G}(\Gamma_{\mathrm{L_1}}) = s^3 L B_{0s}\frac{\overline{b_\phi}}{s}\Big|_{s_1}^{s_2}$. Since we assume stress-free boundaries upon which $\overline{b_\phi} = 0$, both terms are zero, reducing Eq.(F.2) to

$$\frac{1}{4\pi}\frac{\partial}{\partial t}\mathcal{L}_z = \mathcal{G}\left(\Gamma_{\mathrm{L_2}}\right) + \mathcal{G}\left(\Gamma_{\mathrm{R}}\right) . \tag{F.7}$$

Since both $\mathbf{u}$ and $\mathbf{b}$ are solenoidal and periodic in azimuth, Eqs.(F.5) and (F.6) may be rewritten as

$$\Gamma_{\mathrm{L_2}} = \frac{1}{s}\left(\frac{1}{s^2 L}\frac{\partial}{\partial s}\left(s^2 L\,\overline{b_s b_\phi}\right) - \overline{\left(\beta b_s - \frac{\partial}{\partial z}b_z\right)b_\phi}\right) , \tag{F.8}$$

$$\Gamma_{\mathrm{R}} = -\frac{1}{s}\left(\frac{1}{s^2 L}\frac{\partial}{\partial s}\left(s^2 L\,\overline{u_s u_\phi}\right) - \overline{\left(\beta u_s - \frac{\partial}{\partial z}u_z\right)u_\phi}\right) . \tag{F.9}$$

Application of the $\mathcal{G}$ operator to the first term on the right-hand side of each equation again produces terms which depend only on boundary values: $s^2 L\,\overline{b_s b_\phi}\big|_{s_1}^{s_2}$ and $s^2 L\,\overline{u_s u_\phi}\big|_{s_1}^{s_2}$. Because we use no-penetration ($\psi = 0 \rightarrow u_s = 0$) and $a = 0$ ($\rightarrow b_s = 0$) boundary conditions, both

are zero. This leaves

$$\frac{1}{4\pi}\frac{\partial}{\partial t}\mathcal{L}_z = \mathcal{G}\left(\overline{\left(\beta u_s - \frac{\partial}{\partial z}u_z\right)u_\phi}\right) - \mathcal{G}\left(\overline{\left(\beta b_s - \frac{\partial}{\partial z}b_z\right)b_\phi}\right) . \tag{F.10}$$

An axial profile must be assumed for both the $\mathbf{u}$ and $\mathbf{b}$ fields. The no-penetration boundary condition at the spherical top and bottom boundaries dictates that, where the boundary's normal vector is $\hat{\mathbf{n}}$,

$$\mathbf{u}\cdot\hat{\mathbf{n}} = 0 \quad \Rightarrow \quad u_z(L) = -\frac{s}{L}u_s\,. \tag{F.11}$$

Assuming that the u_z velocity profile varies linearly with z, and is zero in the equatorial plane,

$$\frac{\partial}{\partial z}u_z = \beta u_s\,, \tag{F.12}$$

which is consistent with mass conservation ($\boldsymbol{\nabla}\cdot\mathbf{u} = 0$), and the definition of the flow used in Eqs.(2.16) and (2.17). This causes the first term on the right-hand side of Eq.(F.10) to vanish. Our definition of the magnetic field perturbation $\mathbf{b}$ in Eqs.(2.16) and (2.18) follows the same form as that of $\mathbf{u}$:

$$\frac{\partial}{\partial z}b_z = \beta b_s\,. \tag{F.13}$$

Substituting Eqs.(F.12) and (F.13) into Eq.(F.10) causes the remaining terms on the right-hand side to vanish. Thus, the angular momentum is conserved:

$$\frac{\partial}{\partial t}\mathcal{L}_z = 0\,. \tag{F.14}$$